# STARS

University of Central Florida
## STARS

Electronic Theses and Dissertations, 2004-2019

2013

# X-ray Scattering Investigations Of Metallic Thin Films

Andrew Warren
*University of Central Florida*

Part of the Materials Science and Engineering Commons

Find similar works at: https://stars.library.ucf.edu/etd

University of Central Florida Libraries http://library.ucf.edu

## STARS Citation

Showcase of Text, Archives, Research & Scholarship

# X-RAY SCATTERING INVESTIGATIONS OF METALLIC THIN FILMS

by

**ANDREW P. WARREN**
B. S. Physics, University of Central Florida, 2004

A dissertation submitted in partial fulfillment of the requirements
for the degree of Doctor of Philosophy
in the Department of Materials Science and Engineering
in the College of Engineering and Computer Science
at the University of Central Florida
Orlando, Florida

Spring Term
2013

Major Professor: Kevin R. Coffey

# ABSTRACT

Nanometric thin films are used widely throughout various industries and for various applications. Metallic thin films, specifically, are relied upon extensively in the microelectronics industry, among others. For example, alloy thin films are being investigated for CMOS applications, tungsten films find uses as contacts and diffusion barriers, and copper is used often as interconnect material. Appropriate metrology methods must therefore be used to characterize the physical properties of these films. X-ray scattering experiments are well suited for the investigation of nano-scaled systems, and are the focus of this doctoral dissertation. Emphasis is placed on (1) phase identification of polycrystalline thin films, (2) the evaluation of the grain size and microstrain of metallic thin films by line profile analysis, and (3) the study of morphological evolution in solid/solid interfaces.

To illustrate the continued relevance of x-ray diffraction for phase identification of simple binary alloy systems, Pt-Ru thin films, spanning the compositional range from pure Pt to pure Ru were investigated. In these experiments, a meta-stable extension of the HCP phase is observed in which the steepest change in the electronic work function coincides with a rapid change in the c/a ratio of the HCP phase.

For grain size and microstrain analysis, established line profile methods are discussed in terms of Cu and W thin film analysis. Grain sizes obtained by x-ray diffraction are compared to transmission electron microscopy based analyses. Significant discrepancies between x-ray and electron microscopy are attributed to sub-grain misorientations arising from dislocation core spreading at the film/substrate interface. A novel "residual" full width half max parameter is introduced for examining the

contribution of strain to x-ray peak broadening. The residual width is subsequently used to propose an empirical method of line profile analysis for thin films on substrates.

X-ray reflectivity was used to study the evolution of interface roughness with annealing for a series of Cu thin films that were encapsulated in both $SiO_2$ and $Ta/SiO_2$. While all samples follow similar growth dynamics, notable differences in the roughness evolution with high temperature ex-situ annealing were observed. The annealing resulted in a smoothing of only one interface for the $SiO_2$ encapsulated films, while neither interface of the $Ta/SiO_2$ encapsulated films evolved significantly. The fact that only the upper $Cu/SiO_2$ interface evolves is attributed to mechanical pinning of the lower interface to the rigid substrate. The lack of evolution of the $Cu/Ta/SiO_2$ interface is consistent with the lower diffusivity expected of Cu in a Cu/Ta interface as compared to that in a $Cu/SiO_2$ interface. The smoothing of the upper $Cu/SiO_2$ interface qualitatively follows that expected for capillarity driven surface diffusion but with notable quantitative deviation.

Dedicated to my loving parents, Kalina and Andy.

Dziękuję Wam za rady, zrozumienie, i oparcie. Również dziękuję Wam za Waszą

miłość i wiarę w moje możliwości. Kocham Was bardzo!!!

# ACKNOWLEDGMENTS

# TABLE OF CONTENTS

# LIST OF FIGURES

# LIST OF TABLES

# CHAPTER ONE : INTRODUCTION AND SCATTERING THEORY

**1.1 X-ray Scattering Theory: Diffraction**

1.1.1 Phase Identification

Von Laue's successful first attempt at diffracting x-rays from copper sulfate in 1912 [Laue 1913] is a significant historical event in that it not only simultaneously confirmed the wave nature of electromagnetic radiation and the periodicity of atoms within crystals, it also created an entirely new science: X-ray crystallography. Within a year of Laue's published results, W. L. Bragg developed a mathematical representation of the criteria for diffraction, and proceeded to solve the structure of NaCl [Bragg 1913].

Bragg's law, equation ( 1-1 ), has thus become central to x-ray scattering, and remains one of the most widely cited equations in crystallography. The equation:

$$n\lambda = 2d\sin\theta \qquad\qquad (1\text{-}1)$$

relates the wavelength $\lambda$, to d, the spacing between planes, and the angle $\theta$ between the incident x-ray beam and the diffraction plane.

Bragg's Law alone is enough to quantify small changes in the lattice parameter of materials with a known phase, though it does not provide the extinction rules necessary to allow for phase identification. By considering the phase and amplitude of a diffracted wave and the arrangement of atoms, the structure factor can be developed to which the diffracted intensity is proportional.

The simplest phases are found with metals and disordered alloys where simple cubic cells are common. While identifying the phase of a known metal may be redundant, changes in its lattice parameter often result in significantly modified physical properties.

1

Correlating changes in crystal structure to the physical properties of solids is crucial to the field of solid state physics, and finds application in CMOS technology field, among others.

While Bragg's Law remains relevant, and simple crystal structures continue to pose challenges in their analysis, major developments in the field of crystallography and x-ray scattering have greatly matured the field over the past 100 years. The world's increasing reliance on advanced materials renders the use and hence analysis of these materials more common. Bragg's law alone therefore becomes less useful, and fitting algorithms, requiring significant computational power, become essential. Peak profile analysis will be covered in detail in subsequent sections. However, not all x-ray analysis techniques (e.g., Fourier techniques and whole profile fitting methods) were used in this work and will not be described.

### 1.1.2 Grain Size Analysis

X-ray peak profile analysis is a powerful analytical technique that allows for nano-scale structural investigations of materials. The present work focuses on grain size analysis, applying well-known methods to metallic thin films. Peak profile broadening in general will be discussed before embarking onto grain size analysis specifically

#### 1.1.2.1 Peak Broadening

Peak profiles are measurably modified in shape, intensity, position, and width according to the specimens' microstructure. To effectively discuss quantitative x-ray diffraction and grain size analysis, all sources of peak broadening will be introduced.

The three factors contributing to x-ray peak broadening are instrumentation, lattice distortions (strain), and finite grain size [Cullity *et al.* 2001].

Several sources of instrumental broadening exist: These include, but are not limited to: Beam divergence, finite beam width, finite slit widths, residual misalignments, and sample curvature. Additionally, instrumental broadening is not constant, but rather has a functional dependence on detector angle. While "perfect tools" exhibiting no instrument broadening do not exist, the use of a synchrotron source greatly reduces the contribution of instrumentation to peak broadening, owing to the fact that its inherently intense beam may be restricted to a minimally divergent beam and still provide an adequate intensity for experimental purposes.

Figure 1 illustrates the improved resolution offered by the use of a synchrotron source. Closed circles represent instrumental broadening at the Stanford Synchrotron Radiation Light Source, beam line 7-2, equipped with a high resolution double bounce Si(111) monochromator, using a wavelength of 1.54Å. The reported full width at half maximum values are for the first six, most intense, diffraction peaks obtained from NIST Standard Reference Material 660a (Lanthanum Hexaboride Line Position and Line Shape Standard). The open circle represents instrumental broadening of a more conventional laboratory diffractometer; specifically a X'Pert Pro MRD, with a Lens configuration and monocromated Cu-kα radiation. The specimen used for this analysis was NIST Standard Reference Material 640c (Silicon Line Position and Line Shape Standard). The use of a synchrotron x-ray source allows an improvement in resolution of approximately an order of magnitude.
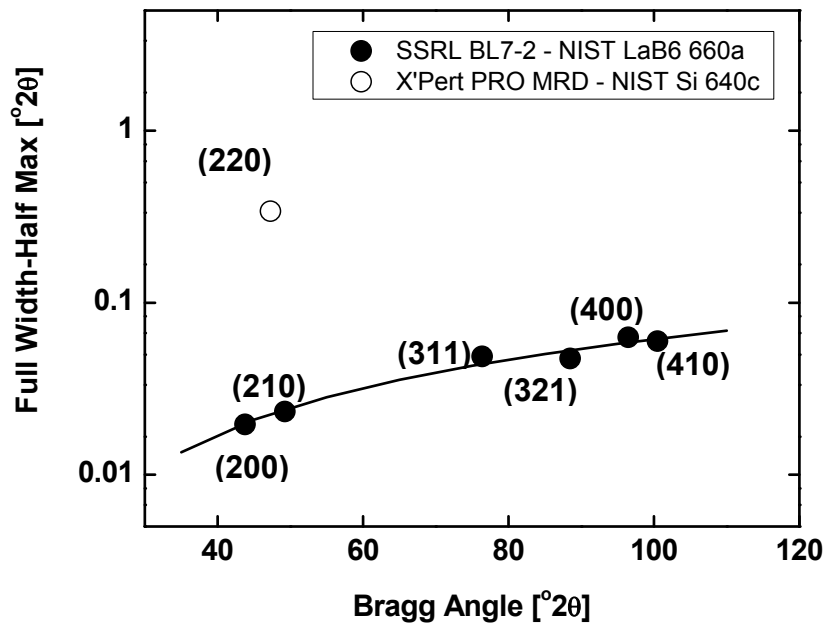
**Figure 1 Instrumental Broadening**

In addition to instrumental effects, sample strain may contribute the broadening of to x-ray peak profiles. Many sources of lattice strain exist, and not all contribute to peak broadening. To illustrate the different effects that strain has on a Bragg reflection, Figure 2 depicts a schematic of a crystalline lattice in a) a zero-strain state b) with a uniform strain and c) with a non-uniform strain. The corresponding diffraction peaks show a) an unaffected reflection whose position corresponding to the expected (zero strain) Bragg angle b) a reflection shifted to lower angles corresponding to an increased lattice spacing c) a broadened reflection, resulting from the distribution of lattice parameters resulting from the non-uniform strain.

4
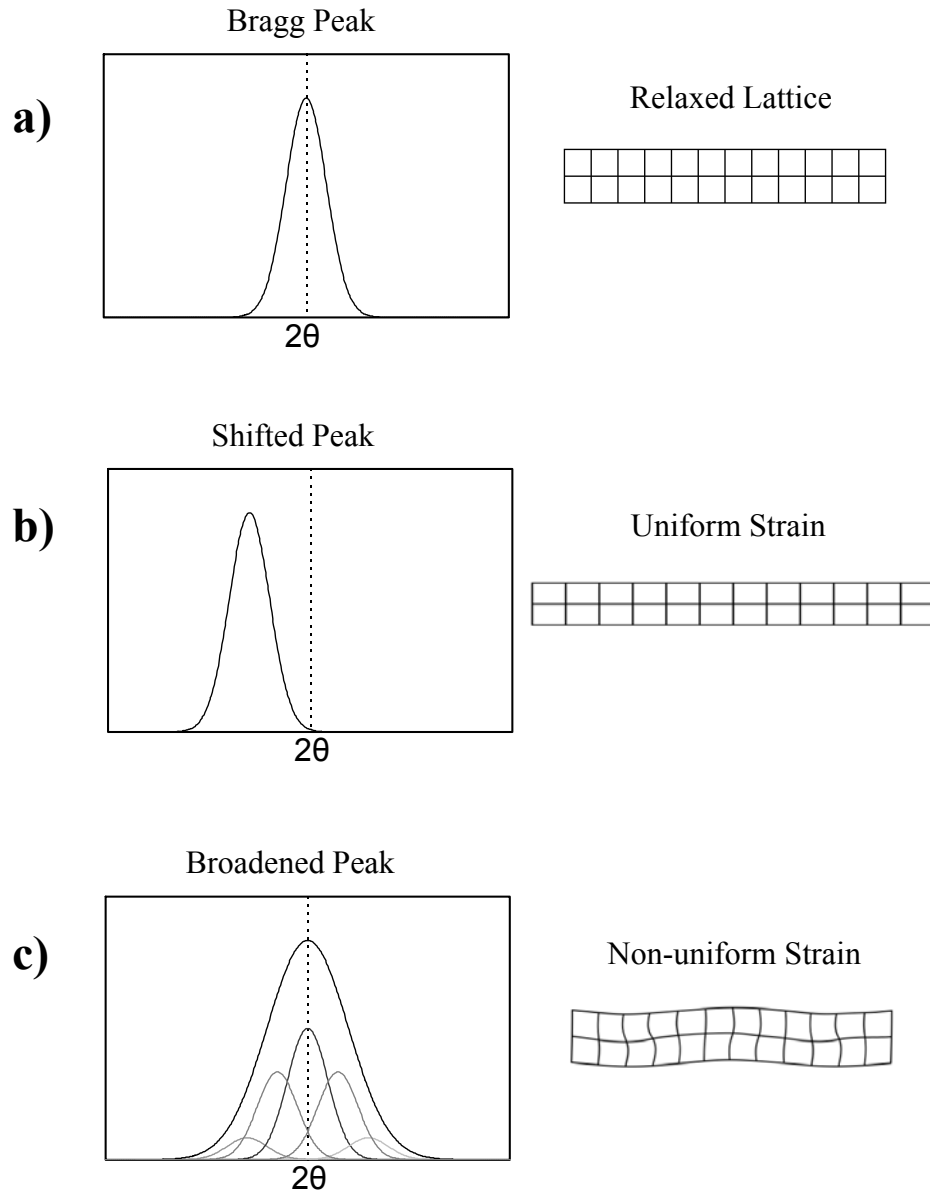
**Figure 2 Effect of strain on x-ray peak profile**

A discussion of strain sources and their respective effects on x-ray line profiles has been found in literature [Ungár 2008], and is summarized in Table 1. Separating lattice defects into point, linear and planar varieties, it has been shown that the decay of a strain field is dictated by the source of the strain, this in turn determines the effect of the strain on the x-ray profile. Point defect strain fields decay as $1/r^2$, therefore, in reciprocal

space the scattering associated with these defects occurs far removed from the fundamental Bragg peak. Linear defect strain fields decay as 1/r, and scattering therefore takes place in the vicinity of the Bragg reflection, thereby contributing to peak broadening. Planar defects produce a constant strain field which cause lattice shifts, and hence peak position displacements; though size-type broadening may also result [Balogh *et al.* 2006].

**Table 1  Lattice defects**

| Strain Source | Comments |
|---|---|
| Point defects | Short range strain fields scatter far from Bragg reflections, contributing to diffuse scattering |
| Precipitates | |
| Inclusions | |
| Chemical heterogeneities | |
| | |
| Dislocations | Lattice defects; Long range strain fields, dislocation-type defects, cause strain broadening |
| Microstresses | |
| Grain boundaries | |
| Sub-boundaries | |
| Coherency strains | |
| Sinter stresses or strains acting between adjacent particles | |
| Chemical heterogeneities | |
| | |
| Stacking faults | Planar defects with homogeneous strain fields. Causes size-type broadening or peak shifts. |
| Twin boundaries | |
| Chemical heterogeneities | |

Although grain size broadening itself will be discussed extensively in subsequent sections, it is important to note here that grain size, strain, and instrument broadening are not simple additive effects, but rather convolute to modify the diffraction peak shape. While Fourier methods are often used to separate the contributions to broadening, no such effort is undertaken herein. Instead, instrument broadening will be subtracted by

assuming convolution profiles. Typically a Gaussian convolution of peak width is assumed:

$$\Delta(2\theta)_{Measured} = \sqrt{\Delta(2\theta)^2 + \Delta(2\theta)^2_{Instrument}}$$

(1-2)

Where $\Delta(2\theta)$ represents the full width-half max. Grain size and strain analysis is therefore performed on the peak, after removing the effects of instrumentation from the measured peak width. Generally however, instrumentation effects may be ignored owing to the use of a synchrotron. The combined effects of strain and grain size, and their respective separations, will be discussed within the context of the Williamson-Hall method.

### 1.1.2.2 Scherrer Equation

A known contribution to x-ray peak broadening is small crystallite size. This effect can be seen by examining the intensity diffracted from a single parallelepiped crystal:

$$I = I_0 F^2 \frac{\sin^2\left(\frac{\pi}{\lambda}\right)(s - s_0) \cdot N_i a_i}{\sin^2\left(\frac{\pi}{\lambda}\right)(s - s_0) \cdot a_i}$$

(1-3)

Where $N_i$ represents the number of atoms along the vector $\mathbf{a_i}$. The vectors $\mathbf{s}$ and $\mathbf{s_0}$ are unitary, and their difference, $(\mathbf{s} - \mathbf{s_0})$ represents the exact Bragg law directions for an hkl reflection:

$$\mathbf{s} - \mathbf{s_0} = \lambda\left(h\mathbf{b_1} + k\mathbf{b_2} + l\mathbf{b_3}\right)$$

(1-4)

Approximating the quotients with Gaussian terms highlights the dependence of peak width on, N:

7

$$\frac{\sin^2 Nx}{\sin^2 x} \rightarrow N^2 e^{\frac{-(Nx)^2}{\pi}} \qquad\qquad (\textbf{ 1-5 })$$

Figure 3 depicts both sides of equation ( 1-5 )  for values of N equal to 5, 50, and 500. Increasing values of N clearly result in narrower peak width, therefore motivating the development of analytical x-ray methods for grain size analysis.  It is interesting to note that the peak widths decrease rapidly with N, thereby limiting grain size analysis to relatively small grains.
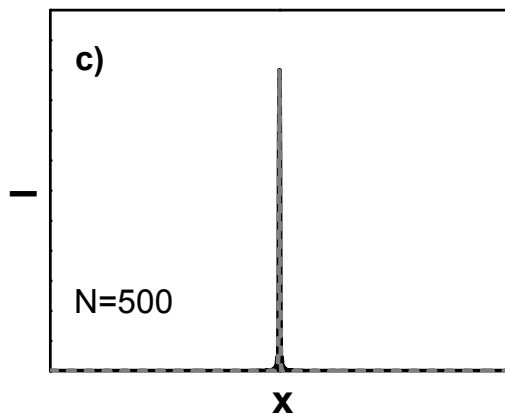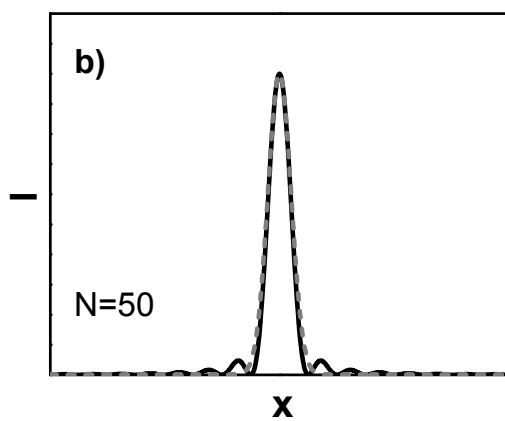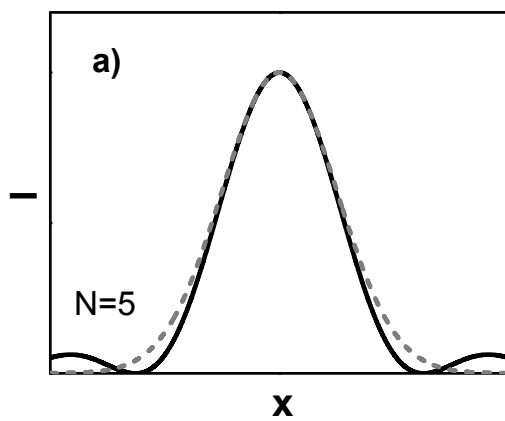
**Figure 3 Size Broadening**

After inserting the Gaussian approximation of ( 1-5 ) into ( 1-1 ) and making appropriate substitutions, the Scherrer equation in its familiar form may be derived. A full account of this derivation is provided in Chapter 13 of Warren's "X-ray Diffraction" [Warren 1990]

Since its first publication, [Scherrer 1918] the Scherrer equation has become a widely used analytical method for determining crystallite size by measuring x-ray line profile broadening. The equation takes the following form:

$$D = \frac{K\lambda}{\Delta(2\theta)\cos\theta}$$

( 1-6 )

where $\Delta(2\theta)$ is the peak breadth or full width at half maximum, $\lambda$ is the wavelength, D is the volume weighted grain size, and K is the shape factor. Though first published almost 100 years ago, investigations showcasing its relevance have been published as recently as 2012 [Khorsand Zak *et al.* 2012], [Gonçalves *et al.* 2012]. Additionally, the technique has also recently been applied to thin films [Savaloni *et al.* 2006], and grazing incidence geometries in the case of small and wide angle scattering experiments [Smilgies 2009].

It is important to note that the Scherrer equation only ascribes peak broadening to grain size, i.e. none of the other broadening mechanisms discussed in the previous section are accounted for by equation ( 1-6 ). Instead, the shape factor was developed as a constant of proportionality that is based on assumed crystallite shapes.

Scherrer originally proposed a value of $2\sqrt{2\ln(2)/\pi} = 0.94$ for K. This value results from the derivation of the Scherrer equation, which assumed cubic crystals and Gaussian peak profiles. While Warren notes that the "exact numerical value has little

significance," [Warren 1990] Langford and Wilson undertook a more rigorous investigation of the shape factor wherein shape factors were determined for various crystal shapes and specific miller indices [Langford *et al.* 1978]. In all cases, the shape factor is approximately equal to unity. An experimental evaluation of the shape factor, as it pertains to thin metallic films, however, has never been undertaken.

### 1.1.2.3 Williamson-Hall plot

As mentioned previously, strain contributes to x-ray peak broadening. Variations in lattice spacing were shown by Stokes and Wilson to broaden the x-ray peak profile according to [Stokes *et al.* 1944]:

$$\varepsilon = \frac{\Delta d}{d} = \frac{\Delta(2\theta)}{4\tan\theta}$$
( 1-7 )

where d is lattice spacing; $\Delta d$ is an upper limit on the deviation from d [Langford *et al.* 1988], $\Delta(2\theta)$ is the full with at half max of the diffracted beam at the Bragg angle $2\theta$. It is important to note that the dependence of strain broadening on the Bragg angle differs from that of size broadening. Specifically; size broadening, unlike strain broadening, is independent of reflection order.

By assuming that size and strain contribute to peak broadening additively, and that the respective peak profiles are Gaussian in nature, Williamson and Hall [Williamson *et al.* 1953] developed a method to separate the effects of size and strain from x-ray line profiles. The analysis method is typically executed graphically, and an example classical Williamson-Hall plot is presented in Figure 4. The corresponding Williamson-Hall equation may be thus be formulated:

$$\Delta(2\theta)\cos(\theta) = \frac{\lambda}{D_{W-H}} + \varepsilon \, 2\sin(\theta s \qquad (1\text{-}8)$$

Where $D_{W-H}$ is the average (Williamson-Hall) grain size, and $\varepsilon$ is the microstrain.
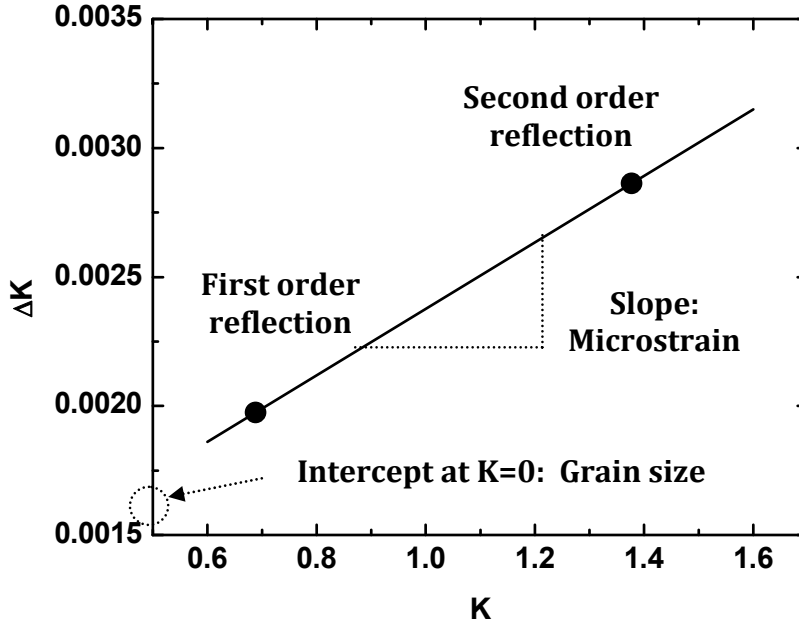


**Figure 4 Classical Williamson-Hall plot**

In the figure $K$ and $\Delta K$ are defined as follows:

$$K = 2\sin(\theta) \qquad (1\text{-}9)$$

$$\Delta K = \Delta(2\theta)\cos(\theta) \qquad (1\text{-}10)$$

The slope of such a plot represents, though poorly defines, micro-strain. The y-intercept is equivalent to the Scherrer equation and is inversely proportional to the grain size:

$$D_{W-H} = \frac{\lambda}{\Delta K_0} \qquad (1\text{-}11)$$

Where $\Delta K_0$ is the y-intercept at K equal to zero.

Anisotropy of strain, however, often prevents the Williamson-Hall plot from revealing the expected monotonous function of peak width with Bragg angle, thereby preventing all reflections from being considered, or making interpretation of results difficult. To address this limitation a modified Williamson-Hall method was developed [Ungár *et al.* 1996]. In this approach, it is assumed that strain broadening is caused exclusively by screw and/or edge dislocations. These dislocations yield different contrasts depending on the relative positions of the Burgers and scattering vectors [Ungár 1996], thereby accounting for the scatter in a plot of the increase of peak width with Bragg angle. An example of a modified Williamson-Hall plot is presented in Figure 5; in which K and ΔK have the same definition as in the classical Williamson-Hall plot.
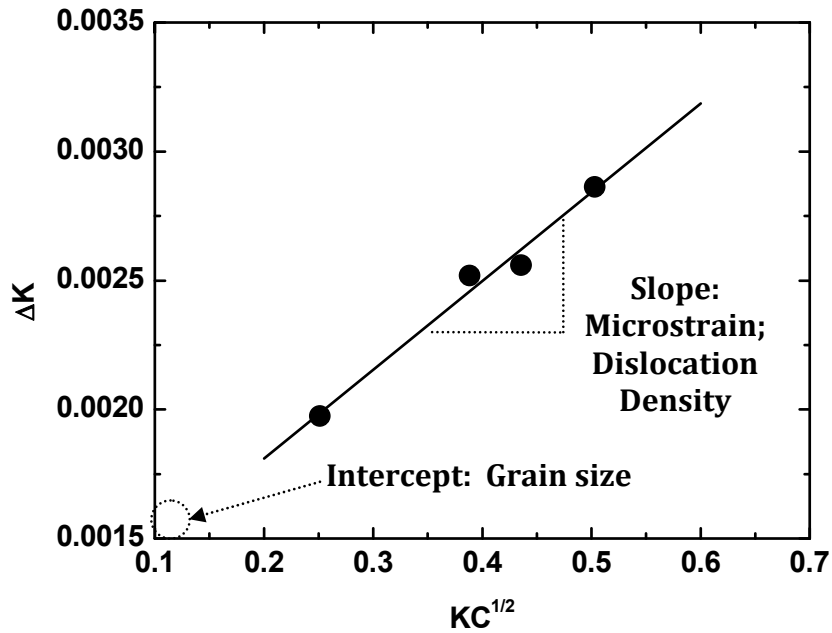


**Figure 5 Modified Williamson-Hall plot**

Likewise the grain size is determined from the quotient of x-ray wavelength and the ordinate-axis intercept. The abscissa is however modified by the square root of the dislocation contrast factor, which for cubic crystals is defined as:

$$C = A - BH^2 = A - B\frac{h^2k^2 + h^2l^2 + k^2l^2}{\left(h^2 + k^2 + l^2\right)^2}$$ ( 1-12 )

A and B are calculated from the crystal's elastic constants, and are therefore material dependent. Additionally the constants A and B contain assumptions regarding the nature of dislocations present, i.e. screw and/or edge. Therefore, if peak broadening is correctly assumed to result from dislocations in addition to grain size, a modified Williamson-Hall plot is designed to reveal a monotonic function of peak width with Bragg angle.

Although the modification of the Williamson-Hall plot identifies a specific source of microstrain, an assumption must be made regarding the relative amount of edge and/or screw dislocations; none of the other strain sources presented in Table 1 are considered.

The concept of dislocation contrast is familiar in transmission electron microscopy: The orientation, relative to a dislocation, of the incident electron beam dictates the visibility, or contrast, of the dislocation. In x-ray diffraction, peak broadening, rather than image contrast, are affected by the relative orientation of Burgers and scattering vectors. The effect is illustrated in Figure 6. The dislocation in Figure 6(a) would not be seen, because it does not modify the lattice spacing in the direction of the scattering vector. Figure 6(b) presents an orientation where the scattering vector is parallel to the Burgers vectors: This orientation provides maximum contrast and allows the dislocation to be observed because it modifies the lattice spacing along the Q direction.
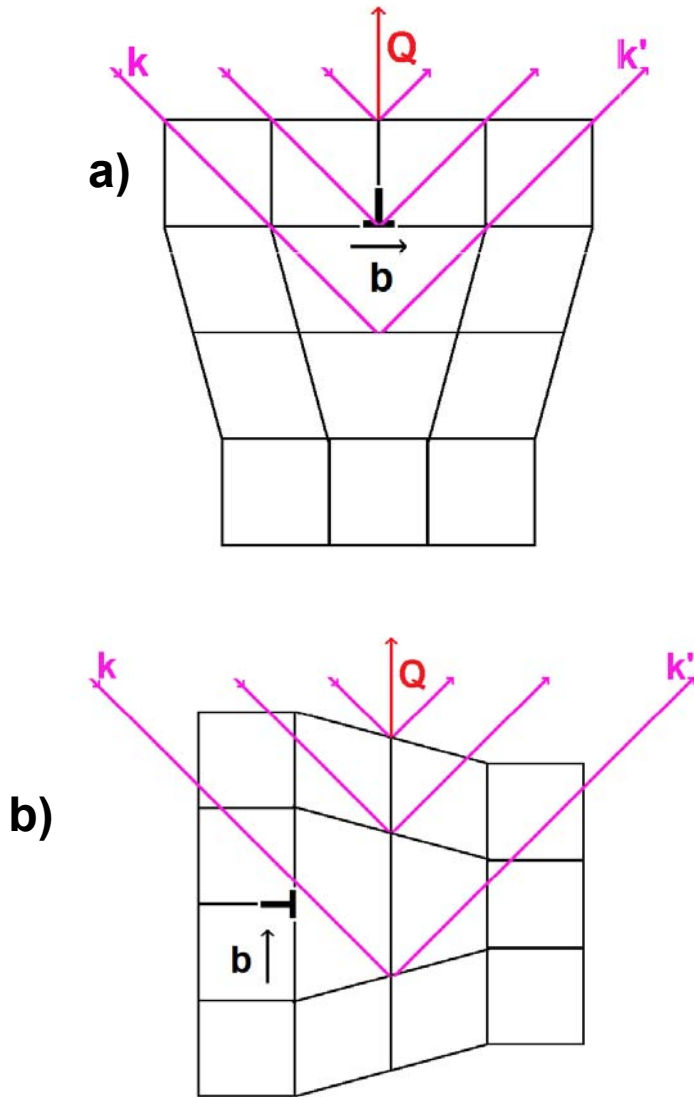
**Figure 6 Schematic representation of dislocation contrast**

In summary, the Modified Williamson-Hall method may be represented by the following equation:

$$\Delta(2\theta)\cos(\theta) = \frac{\lambda}{D_{ModW-H}} + \varepsilon\, C^{1/2}\, 2\sin(\theta)$$

( 1-13 )

The roll of dislocations to broaden x-ray line profiles, as per the modified Williamson-Hall plot, provides a construct by which dislocation density may be calculated.  Though

the Fourier methods used to derive its meaning are not discussed here, the micro strain takes the form of equation ( 1-14 ) [Birkholz *et al.* 2006];

$$\varepsilon = b\sqrt{\frac{A_\rho \pi \rho_d}{2}}$$

( 1-14 )

Where b is the Burgers vector, $\rho_M$ is the dislocation density and $A_\rho$ is a constant that depends the effective outer cut-off radius of dislocations. The outer cut-off radius of dislocations should not be confused with the dislocation core width ($W_\rho$) wich will be discussed in later sections. $A_\rho$ is typically assumed to equal 10 [Wilkens 1970], though experimental investigation of ball-milled iron powder have reported a value of 3.3 [Révész *et al.* 1996].

## 1.2 X-ray Scattering Theory: Reflectivity

The current work utilizes X-ray scattering to study the interfacial evolution of encapsulated Cu thin films. Both specular and diffuse X-ray reflectivity's are highly sensitive to surface and interfacial roughness and existing theories of X-ray scattering make these techniques highly quantitative. Because the description of a rough surface is non-trivial, a detailed discussion regarding surface statistics will precede the introduction of x-ray reflectivity.

### 1.2.1 Surface Statistics

The various parameters used to describe a surface are first introduced, and are followed by a brief discussion of the fractal nature of random rough surfaces and their scaling behavior in time. More detailed discussions may be found in the literature [Pelliccione *et al.* 2008]. The mean height $\bar{h}$ of a surface profile $h(x,t)$ represents an

16

arbitrary reference height, which is defined as $\bar{h}(t) \equiv \langle h(x,t) \rangle$, and is typically set to equal

0. The standard deviation of $\bar{h}$, $\sqrt{\langle [h(x,t)]^2 \rangle}$, is defined as the interface width (or RMS

roughness) and is typically denoted by the Greek letter, σ. While h and σ describe

vertical aspects of a rough profile, the correlation function, C(r), allows for the lateral

roughness character to be expressed.

The correlation function is simply a cross correlation of a surface with itself and

measures the distance over which surface heights are correlated. Though various forms

of the correlation function exist, it is here defined from experimental data to be:

$C(r,t) \equiv \sigma^{-2} \langle h(x,t)h(x+r,t) \rangle$. By inspection, it can be noted that C(r) decreases with

increasing r: Therefore, the decay rate of C(r) is indicative of the length scales over

which the surface heights are correlated. From C(r), the correlation length $\xi$ can be

defined: For isotropic surfaces, $\xi$ is the value of r for which the correlation function

drops to $e^{-1}$ of it initial value.

Several analytical appproximations of the correlation function pertaining to the

description of surfaces exist: The most commonly used correlation function for

describing rough surfaces is the exponential form which is commonly written as [Sinha *et al.* 1988]:

$$C(r) = \sigma^2 \exp\left[ -\left( \frac{r}{\xi} \right)^{2\alpha} \right]$$
( 1-15 )

The assumption of isotropic surface roughness allows the use of a single in-plane

coordinate, r, equal to $(x^2 + y^2)^{1/2}$. The power within the exponential term includes α,

which is the Hurst or fractal exponent that further characterizes the surface; a small value

17

of α describes a jagged surface and as α approaches 1, a smooth surface is represented

Upon obtaining values for $\sigma$, $\alpha$ and $\xi$, Fourier methods allow for a surface profile to be numerically reconstructed [Ogilvy *et al.* 1989].

At times, a simplified sinusoidal model can appropriately be used to describe a surface, thereby avoiding the computationally involved Fourier methods. However, sinusoidal functions necessarily have a characteristic in-plane length scale (the wavelength, $\lambda$). Random rough surfaces, on the other hand, possess no such characteristic dimension, and are typically understood to be self-affine; having a generalized height profile that follows $h(x) \sim \varepsilon^{-\alpha} h(\varepsilon x)$, where $\varepsilon$ is a scaling factor [Mandelbrot 1985].

Self-affinity is a fractal property whereby anisotropic rescaling of the fractal dimensions are needed so as to observe the systems self-similarity. This is contrary to self-similar systems whose x and y dimensions scale equally to return an identical profile. Figure 7 illustrates, by example, the difference between self-affine and self-similar functions. Figure 7 (a) present the plotted function f(x) = x. Upon rescaling both axis by equal amount, the same curve is returned (Figure 7 (b)): Self similar behavior is evident. Figure 7 (c) and (d) present the plotted function f(x) = $x^{1/3}$. The abscissa in Figure 7 (c) must be rescaled by a different amount than the ordinate axis if an identical profile is to be obtained.
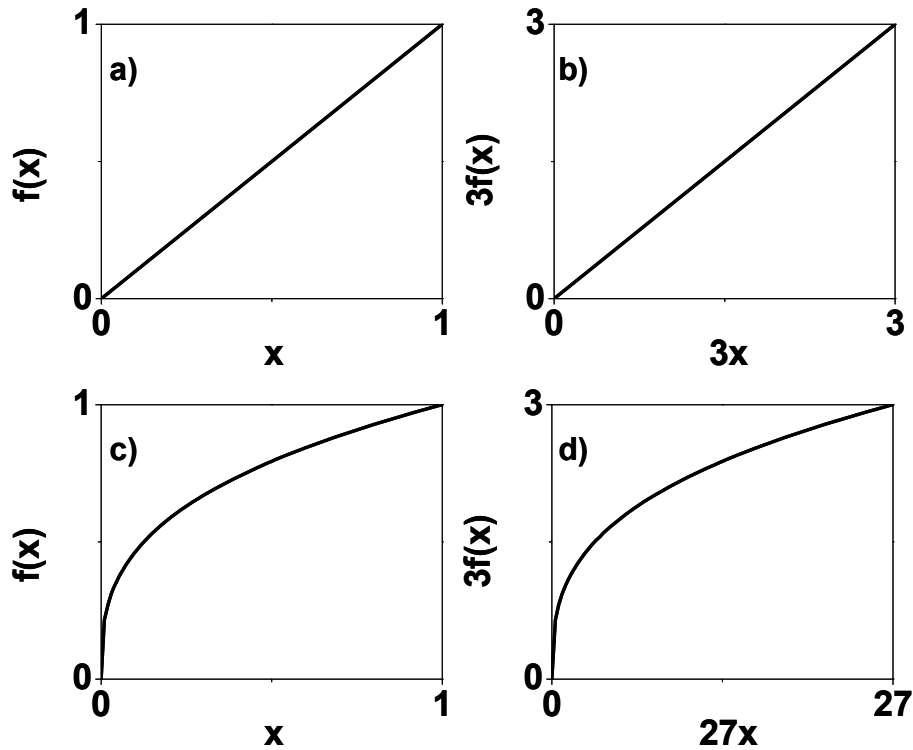
**Figure 7 Self-similar scaling (a and b) and self-affine scaling (c and d)**

It should be noted that self-affine scaling is not necessarily valid over all length scales, but rather only over a relatively narrow spatial window. To elaborate, the shape of a surface is not well defined over length scales that are smaller than that of an atom, thereby rendering the self-affine description invalid. Additionally, at very large length scales, if for example the otherwise self-affine and planar surface is that of a sphere, different geometrical arguments will be needed to describe the systems large scale curvature. Nonetheless, since our interest is in the length scales intermediate to these extremes, the assumption will be made throughout this text that for all length scales being discussed, the self-affine description of a surface is always valid unless otherwise specified.

The time dependent surface morphology of growing self-affine interface can be understood within the context of dynamic scaling. For self affine systems, the concept of dynamic scaling can be summarized by modifying the generalized representation of the height profile to include proper time dependence [Barabási *et al.* 1995], [Meakin 1998], [Family *et al.* 1985] : $h(x,t) \sim \varepsilon^{-\alpha} h(\varepsilon x, \varepsilon^z t)$, where $z$ is the dynamic scaling exponent. Therefore if one increases the growth time by a factor $\varepsilon$, the lateral correlation length must increase by a factor $\varepsilon^{1/z}$ :

$$\xi(t) \sim t^{1/z} \qquad\qquad (1\text{-}16)$$

Similarly, the interface width must increase by a factor of $\varepsilon^{\alpha/z}$:

$$\sigma(t) \sim t^{\alpha/z} = t^{\beta} \qquad\qquad (1\text{-}17)$$

where $\beta$ is the growth exponent. Collectivity, the dynamic growth exponents, $\alpha$, $\beta$, and $z$ are related to one another in a specific manner, and are used to describe a self-affine surface and its growth behavior.

Values for the growth exponents have been derived theoretically for various growth mechanisms. Typically, stochastic equations are used to model growth dynamics and to predict values for the growth exponents. The general form of a stochastic continuum equation for a growing surface is as follows [Pelliccione *et al.* 2008] [Keblinski *et al.* 1996]:

$$\frac{\partial h(x,t)}{\partial t} = \Phi(x,\{h\},t) + \eta(x,t) \qquad\qquad (1\text{-}18)$$

where $\eta(x,t)$ is noise in the system (usually assumed to be Gaussian), and $\Phi(x,\{h\},t)$ represents a height profile that changes according to some growth. A linear form of $\Phi(x,\{h\},t)$ results in the Edwards-Wilkinson (EW) equation[Edwards *et al.* 1982]:

$$\frac{\partial h}{\partial t} = \upsilon \nabla^2 h + \eta \qquad\qquad \text{( 1-19 )}$$

A quadratic term in $\Phi(x,\{h\},t)$ yields the Kardar–Parisi–Zhang (KPZ) equation [Kardar *et al.* 1986]:

$$\frac{\partial h}{\partial t} = \upsilon \nabla^2 h + \frac{\lambda}{2}\left|\nabla h\right|^2 + \eta \qquad\qquad \text{( 1-20 )}$$

Physically, the EW equation has been used to describe random deposition followed by instantaneous relaxation [Vvedensky 2003] and predicts the following growth exponent values:

$$z = 2; \quad \alpha = \frac{2-d}{2}; \quad \beta = \frac{\alpha}{z} = \frac{2-d}{4} \qquad\qquad \text{( 1-21 )}$$

where *d* is the dimensionality of the system. The KPZ equation has been physically attributed to a ballistic deposition process [Aarão Reis 2001] and predicts the following growth exponent values for systems growing in 1+1 dimensions and 2+1 dimensions respectively:

$$z = \frac{3}{2}; \quad \alpha = \frac{1}{2}; \quad \beta = \frac{\alpha}{z} = \frac{1}{3} \qquad\qquad \text{( 1-22a )}$$

$$z = 1.58; \quad \alpha = 0.38; \quad \beta = 0.24 \qquad\qquad \text{( 1-22b )}$$

KPZ scaling further assumes that growth only takes place along the surface normal thereby predicting conformal growth.

1.2.2 Surface and Interface Kinetics

Figure 8 presents an idealized cross-sectional view of a buried interface between materials A and B having sinusoidal interface morphology of wavelength, $\lambda$. If material A is unable to support mechanical stresses (i.e., is a gas, a liquid, or vacuum), then the

21

capillarity driven smoothening of the surface of solid material B (which defines the interface location) should occur relatively unimpeded. Simply stated; smoothing should occur due to the diffusion potential being proportional to the local curvature of a surface. In this case, the atoms of material B are expected to migrate from the crest (position 1B) towards the trough (position 2B) of the undulating surface, ultimately resulting in a lower total surface free energy by reduction of the surface area. If material A is a solid and able to support mechanical stress, then the rates at which the interface between the two materials may evolve are mechanically coupled.
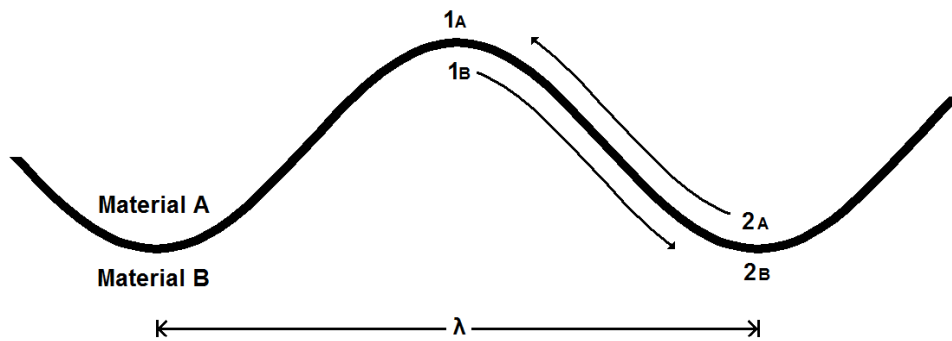


**Figure 8 Idealized solid-solid interface of wavelength λ**

For buried interfaces, the local curvature is of opposing sign for each solid, i.e., the crest of material A is the trough of material B, and capillarity based smoothing due to surface diffusion might be expected to occur simultaneously for both of the solid materials A and B that define the interface. However, if the two solids have very different interfacial diffusivities, then mechanical stresses will be present, i.e., if material B has much faster interfacial transport than A, then material A may be considered rigid and inert and the tendency for atoms of material B to migrate from position 1B to position 2B will result in a pressure (stress) differential between these two positions (positive pressure at 2B, negative pressure at 1B) that will modify the diffusion potential

22

for material B so as to inhibit further transport [Larche *et al.* 1982]. In this case, the smoothing of the interface will be limited by material A. The mechanical coupling across the interface between materials A and B can have two possible effects. The first effect is that the positive pressure induced at position 2B will also result in a positive pressure at position 2A, such that the pressure differential transmitted across the interface is of the sign to further enhance the diffusion potential of material A to move from its crest to its trough (2A to 1A). In this manner the diffusion potential difference driving transport of each material in the shared interface is coupled mechanically, and an effective interfacial diffusivity and effective atomic volume for the coupled capillarity driven interfacial transport of both species can be considered. The second effect is that the material with the slower interfacial transport may be plastically deformed by the shared stresses induced by the faster material. This can be expected to be more likely when one of the materials is in the form of a membrane, having a thickness less than or comparable to the wavelength of the interfacial roughness.

The introduction of an inhomogeneous and anisotropic strain distribution along the interface will result in local variations of lattice parameter and a stress contribution to the chemical potential gradients in the interface that drive atomic transport. This should limit the effects of capillarity since no longer is interface curvature the only driving force for diffusion of each species. The effects of strain (lattice parameter) on surface diffusion have been studied in the past and it has been shown that compressive strains increase the surface diffusion potential [Brune *et al.* 1995], though the opposite can at times be true [Shu *et al.* 2001].

The classical model for capillarity driven smoothing of a solid/vapor interface (or solid/vacuum interface) by surface diffusion of the solid is well developed [Nichols *et al.* 1965] [Balluffi *et al.* 2005] and can be extended to the case of the mechanically coupled transport of two solids at a buried interface. If the surface is assumed to be homogenous, isotropic, and sinusoidal, with a time dependent amplitude:

$$h(x,t) = A(t)\sin\left(\frac{2\pi x}{\lambda}\right) \tag{1-23}$$

it has been shown that for free surfaces the aforementioned time dependent amplitude (i.e., $\sigma\sqrt{2}$ the RMS roughness) takes the following form:

$$A(t) = A_0 e^{-B(2\pi/\lambda)^4 t} \tag{1-24}$$

Where t is time, $\lambda$ is wavelength and B is a kinetic coefficient given by $B = \Omega\gamma\delta D/kT$, where $\Omega$ is the atomic volume of the moving atoms, $\delta$ is the interfacial thickness, $\gamma$ and D are the interfacial energy and an effective surface diffusivity, respectively, and kT is the usual product of Boltzmann's constant and temperature. These results can be extended to the case of interfacial diffusion along buried interfaces by considering $\Omega$ as the effective average atomic volume of the interfacial materials and D is the effective interfacial diffusivity of the coupled transport and it is assumed that voids do not form in the interface.

From equation ( 1-24 ), it can be seen that for a free surface having many different wavelength components, as is normal for roughness, the short wavelength roughness should disappear much faster than long wavelength roughness, and thereby cause an increase in the lateral correlation length. As in a free surface, for a buried interface

simple capillarity is expected to not only decrease the total RMS roughness, but also serve to increase the lateral correlation length of the roughness.

For the case of free surfaces processed such that the height modulations approach a sinusoidal approximation, the amplitude decay has been experimentally verified [Maiya *et al.* 1965] to be proportional to the inverse of wavelength to the fourth power, $\lambda^{-4}$. Nonetheless, deviations from the $\lambda^{-4}$ dependence have been proposed theoretically [Dubson *et al.* 1994] and have been observed experimentally [Castez *et al.* 2006] [Erlebacher *et al.* 2000]. Furthermore, it should be stressed that a $\lambda^{-4}$ dependence is expected only for surface diffusion. Bulk and vapor diffusion modify the decay exponent to $\lambda^{-3}$ and $\lambda^{-2}$ respectively.

In regards to encapsulated Cu films, it is expected that $\sigma$ will decrease with time according to equation ( 1-24 ). Furthermore, although $\xi$ and $\lambda$ are not equivalent, shorter wavelengths are nonetheless expected to decrease more quickly, leading to an effective increase in $\xi$.

1.2.3 X-Ray Reflectivity

X-ray reflectivity is a powerful technique for the study of surfaces and buried interfaces in thin film systems [Tolan 1998], [Holý *et al.* 1999]. There are two primary variations of this technique, specular and diffuse.

In specular X-ray reflectivity, a narrow beam of X-rays is incident upon a specimen and the intensity of the beam reflected at an angle equal to the incident angle is measured. The variation of reflected beam intensity as a function of the common incidence and reflection angle will contain information regarding:

Sample density - by determining the critical angle for total external reflection,

Sample thickness - by measuring the period of the Fresnel oscillations, and

Root-mean-square (RMS) roughness ($\sigma = {}^{A_0}\!/_{\sqrt{2}}$)- by measuring the decay of the reflected intensity.

The second variation is diffuse X-ray reflectivity, in which the intensity of X-rays scattered at angles not equal to the incidence angle is measured. Analysis of the diffusely scattered intensity yields information regarding the in-plane structure of the sample, i.e. the lateral correlation length ($\xi$).

It should be noted that independent values for $\sigma$ corresponding to the upper and lower Cu interfaces may be obtained from the X-ray reflectivity experiments. Independent values of $\xi$ however, are more difficult to measure; accordingly, the generalization will be made that the values of $\xi$ represent a combined effect of the upper and lower film interfaces.

The coherent scattering approximation for evaluation of X-ray reflectivity data was first developed by Parratt [Parratt 1954]. The effects of roughness were later described by Vidal [Vidal *et al.* 1984] and de Boer [De Boer *et al.* 1996]. The calculation of the incoherent component of scattered X-rays caused by roughness requires the use of the distorted-wave Born approximation. For a detailed account of the above, the reader is directed to references [Holý *et al.* 1999], [Schmidbauer 2003], [Tolan 1998]. From these, it is known that the intensity of a specular reflection from a rough surface is attenuated exponentially, and can be described by

$$I = I_0 e^{-Q_z^2 \sigma^2} \qquad\qquad \text{( 1-25 )}$$

Where $I_0$ is the direct beam intensity, $Q_z$ is the normal component of the momentum transfer vector and $\sigma$ is the RMS roughness.  The intensity that is lost from the specular reflection due to roughness is scattered diffusely in a manner described theoretically; using the first order Born approximation, the total scattered intensity per unit area for a single rough surface can be shown to take the following form [Sinha *et al.* 1988] :

$$I(\bar{Q}) = \frac{I_0 e^{-Q_z^2 \sigma^2}}{Q_z^2 \iint e^{Q_z^2 C(x,y)} e^{-i(Q_x x + Q_y y)} dx dy} \qquad\qquad \text{( 1-26 )}$$

In this equation $C(x,y)$ is the correlation function (1-14).

The above reflectivity model is applicable to scattering from a single rough surface (interface).  In the case of multiple non-ideal interfaces, the calculation of the specularly reflected intensity must be further modified by Fresnel coefficients. Additionally, the correlation function must be modified to include the correlation of each interface, and their cross correlations.  Measurement of the cross correlation allows for a vertical correlation fraction (or the amount of conformality in topography that translates from one layer to the next) $\xi_V$ to be determined.  The model is further complicated by realizing that equation ( 1-15 ) only has analytical solution for a Hurst exponent equal to 0, ½, or 1 and therefore numeric integration must be used to solve these equations.  To model the experimentally obtained intensity profiles, commercially available software from Bede is available which employs a genetic algorithm referred to as "Differential Evolution"[Wormington *et al.* 1999].

# CHAPTER TWO :  EXPERIMENTAL DETAILS

The works discussed herein focus on metallic thin films on thermally oxidized single crystal Si substrates.  All samples were processed by sputter deposition, and subsequent x-ray investigations were performed.  The varying nature of these distinct sample sets and the separate investigations undertaken dictates that experimental details be considered individually as they pertain to each sample set.

## 2.1 Pt-Ru

To investigate the meta-stable phases of Pt-Ru as a function of composition and their effects on the alloy work function, several characterization experiments were performed. The information provided here pertaining to these Pt-Ru investigations has been previously published [Warren *et al.* 2008].

### 2.1.1 Sample preparation

Pt-Ru alloys were prepared by sputter deposition in an ultra high vacuum (UHV) system. The alloys were formed by co-sputtering Pt and Ru from elemental targets with a purity of 99.95 %.  A quartz crystal thickness monitor was used to calibrate deposition rates at various DC power settings which allowed for alloy composition to be controlled. The base pressure was $\sim 1 \times 10^{-8}$ Torr, while the deposition pressure was maintained at 4 mTorr with a flow of 20 sccm of Ar. The purity of the Ar process gas was maintained by a hot reactive metal getter. Process gas contamination in the deposition chamber at the typical deposition pressure of 4 mTorr was confirmed to be less than 10 ppm (the instrumental sensitivity limit) by closed ion source quadrapole mass spectrometry.

Films were deposited onto glass substrates for X-ray diffraction analysis to prevent the artifacts that often result from multiple scattering events within a single crystal Si substrate. Films for transmission electron microscopy and work function measurements were deposited on Si wafer substrates and the details of the work function measurements have been reported previously [Todi *et al.* 2006], [Todi *et al.* 2007].

2.1.2 X-ray Scattering

Because the film thickness is far below the penetration depth of x-rays at normal incidence, grazing incidence x-ray diffraction (GIXRD) experiments were performed for the investigation of these Pt-Ru films. A Rigaku D-Max was used with Cu Kα radiation and a thin films attachment. The GIXRD geometry used in these investigations is represented schematically in Figure 9.
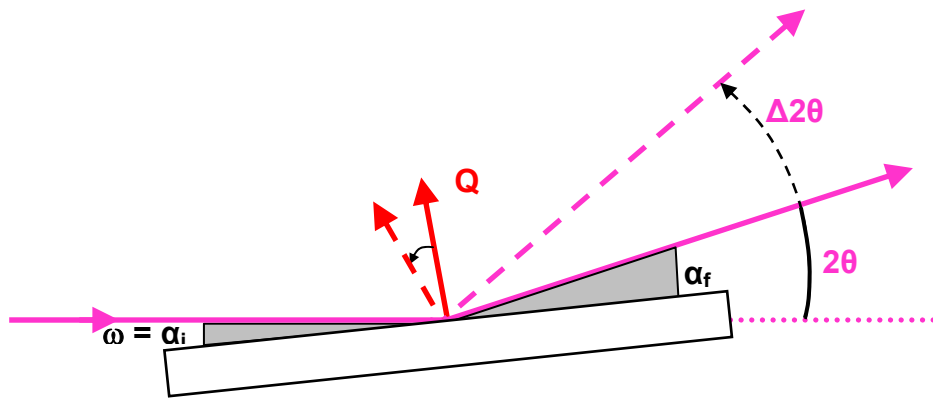


**Figure 9 GIXRD Geometry: $\alpha_i$ remains constant, the detector scans a range $\Delta 2\theta$**

In these experiments , the specimen angle remains fixed at low angles, typically near the critical angle for total external reflection. The sample angle ($\omega$) is equal to the incident angle ($\alpha_i$). The detector scans its axis across a range $\Delta 2\theta$. The diffracted beam therefore makes and angle with the sample $\alpha_f = (2\theta - \alpha_i)$.

This geometry limits the penetration depth of the x-rays, thereby maximizing diffraction intensity from the surface layer. It should be noted that, in these grazing scans, the measured in plane and out of plane components of the scattering vector change as a function of detector angle; owing to the fact that $\alpha_i$ remains constant but $\alpha_f$ does not. The effect may be quantified by considering the following equations which represent the in plane and out of plane components of $\mathbf{Q}$; i.e. $Q_x$ and $Q_z$ respectively:

$$Q_x = \frac{2\pi}{\lambda}(\cos\alpha_f - \cos\alpha_i)$$

**( 2-1)**

$$Q_z = \frac{2\pi}{\lambda}(\sin\alpha_i + \sin\alpha_f)$$

Figure 10 presents the path taken through reciprocal space of a GIXRD experiment in which $\alpha_i$ is taken to be 5° and $\lambda$=1.54Å. Because $Q_x$ and $Q_z$ both vary comparably in GIXRD, highly textured or epitaxial films may not be measurable. This scattering geometry is however very well suited for poly crystalline thin films. Though not discussed here, structural depth profiles may additionally be generated using this technique by performing several GIXRD measurements in which $\alpha_i$ is incremented between subsequent scans.
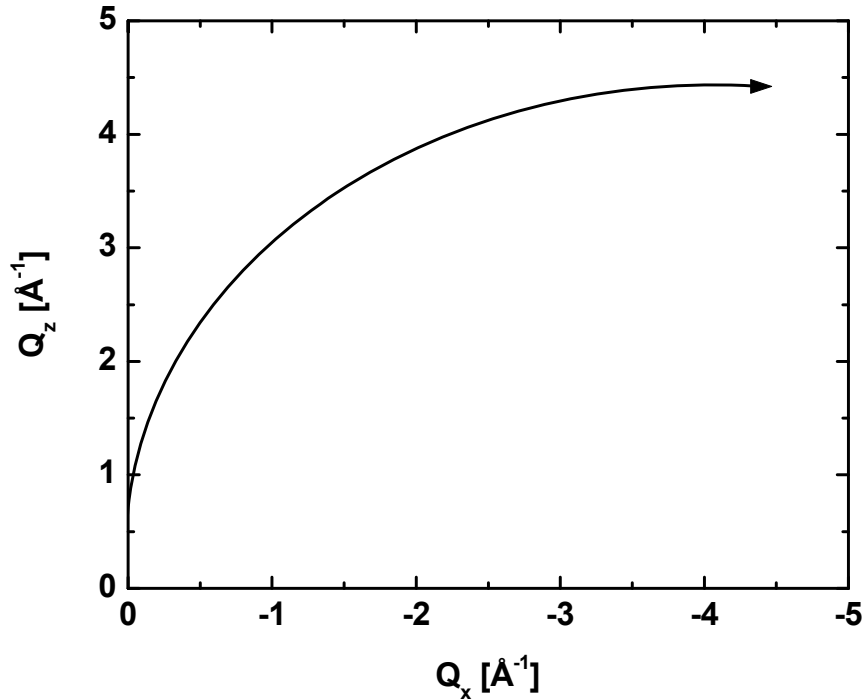
**Figure 10 GIXRD trace through reciprocal space**

GIXRD was used to investigate the crystal structure of Pt-Ru alloys as a function of their respective compositions. Analysis of GIXRD patterns was performed using commercially available software frm MDI: Jade 7.5. The Pt-Ru thin films, on glass substrates, were cut into approximately 1x1cm squares and were rinsed with alcohol to provide a relatively clean surface prior to characterization.

Additionally X-ray reflectivity (XRR) was used to determine film thickness by analysing secular reflectivity patterns with Bede REFS software [Wormington *et al.* 1999]. Only specular scans were collected for the purpose of thickness measurement; A detailed discussion of x-ray reflectivity is presented in subsequent sections, pertaining to the investigation of encapsulated metallic thin films.

2.1.3 Additional Characterization

Rutherford backscattering spectroscopy (RBS), performed with a General IONIX 1.7 MV Tandetron RBS system, was used to determine alloy composition. RBS data was analyzed using the free software package RUMP.

To supplement x-ray analysis, plan-view bright field and dark field images were collected along with corresponding selected area electron diffraction patterns. A Phillips Tecnai F30 transmission electron microscope was used. Samples were prepared using a back etch technique to remove the Si substrate [Yao *et al.* 2008].

**2.2 Encapsulated Cu and W**

A series of encapsulated Cu and W thin films were extensively characterized by X-ray and transmission electron microscopy (TEM) methods. The original motivation for establishing deposition processes for these specimens was to study the electronic properties of the encapsulated nanometric metallic films, and many details regarding sample preparation may be found in previously published works; references to which are provided in the following section.

2.2.1 Sample preparation

Details of the sample preparation process have previously been published [Sun *et al.* 2010], [Choi *et al.* 2012]. Furthermore, the electronic properties of these films were the focus of past dissertations by Sun [Sun 2009] and Choi [Choi 2011]:

The following is an excerpt from the work by Sun:

"The encapsulated Cu thin films were prepared on 3" diameter Si

(100) substrates having a nominally 1500Å thick layer of thermally grown

$SiO_2$. The substrates were mounted onto a Cu substrate platen with a mechanical clamp ring and a thin layer of vacuum grease (Apeizon N) between the wafer backside and the platen to insure adequate thermal contact in vacuum. The Cu substrate platen was introduced into a UHV sputter deposition chamber via a load-lock chamber and RF sputter cleaned in 10 mTorr of $Ar+2\%O_2$ for 15 minutes at low power (0.2 W/cm²). After cleaning, the substrate and platen were cooled prior to deposition to -40°C by contact with a liquid nitrogen cooled Cu plate. The substrate temperature prior to deposition was controlled by variation of the allowed cooling time and was confirmed for each sample by measurement of plate temperature immediately upon venting.

For films having the $SiO_2/Ta/Cu/Ta/SiO_2$ structure, a layer of 20Å of Ta was DC sputter deposited immediately prior to, and again after, the Cu layer deposition. These films were otherwise prepared similarly to the $SiO_2/Cu/SiO_2$ process described above. The Cu films, of thickness ranging from 270Å to 1580Å, were deposited by DC sputter deposition from high purity (99.9999%) Cu targets at a rate of 6 Å/sec onto the electrically grounded substrates.

layer depositions were performed at a total pressure of 4 mTorr of Ar process gas while the metal layers were deposited at 2 mTorr of $Ar+3\%H_2$. A deposition chamber pressure in the $10^{-9}$ Torr range was obtained prior to film deposition and the nominally 99.999% purity Ar

was passed through a hot reactive metal getter purifier (SAES Pure Gas) prior to introduction to the chamber.

Annealing treatments of 150°C and 600°C for 30 minutes were performed on both $SiO_2/Cu/SiO_2$ and $SiO_2/Ta/Cu/Ta/SiO_2$ structure samples in a tube furnace to provide grain size variations at each thickness of the Cu layer. An Ar+5%$H_2$ reducing process gas was used in both annealing treatments to prevent oxidation of the Cu layer."

The Encapsulated W films were deposited using the same procedure as that is described by Sun, with the modification that depositions were performed at room temperature and no RF substrate cleaning was used. [Choi 2011].

2.2.2 X-ray Scattering

*2.2.2.1 X-ray Diffraction*

X-ray scattering investigation of encapsulated Cu and W films were performed using a grazing incidence diffraction (GID) geometry. The large lateral coherence, established by the in plane scattering geometry, renders GID experiments well suited for studying the in plane structure of crystalline matter. Detailed descriptions of in plane scattering experiments and scans through reciprocal space may be found in textbooks [Birkholz *et al.* 2006], [Holý *et al.* 1999].

Figure 11 illustrates GID schematically. $I_0$ and $I_f$ indicate the incident and diffracted beams respectively. The angles between the respective beams and the sample plane are denoted as $\alpha_i$ and $\alpha_f$ (which in these experiments are equal to each other) and

together dictate the in plane and out of plane components of Q, the scatting vector.  $2\theta$ is the scattering angle; the samples angle ($\omega$, not shown) equals half of $2\theta$.
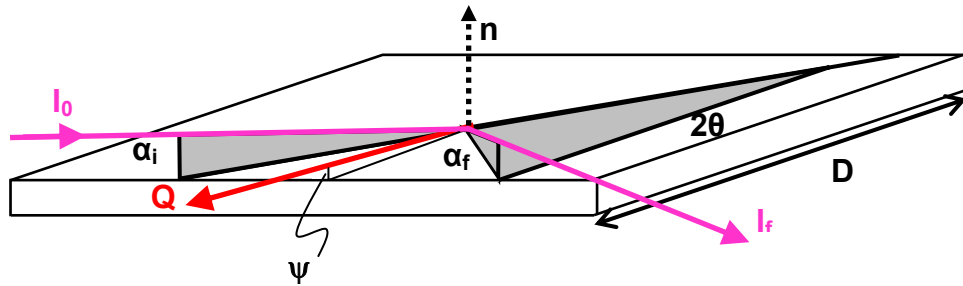


**Figure 11 GID Geometry:  $\alpha_i$ and $\alpha_f$ are small and equal, and approximately equal to $\psi$.  Q remains in the plane.**

Because $I_0$ emits from a  fixed source, the sample tilt angle, $\psi$, establishes $\alpha_i$ and $\alpha_f$.  A GID experiments may therefore be performed by moving $\psi$ to low angles ($\sim2°$), and proceeding with a coupled $\theta$-$2\theta$ scan.  The in plane and out of plane components of Q may therefore be written as follows:

$$Q_x = \frac{2\pi}{\lambda}\left(\cos\alpha_f\sin\theta + \cos\alpha_i\sin\theta\right)$$

$$(\,2\text{-}2\,)$$

$$Q_z = \frac{2\pi}{\lambda}\left(\sin\alpha_i + \sin\alpha_f\right)$$

While values for $\alpha$ may be taken to equal $\psi$,  close inspection reveals that $\alpha_i$ and $\alpha_f$  are however only approximately equal to $\psi$, and are additionally functions of $\omega$. Figure 12 illustrates the co-dependence of $\alpha$ on $\psi$ and $\omega$.  Depictions of $\omega$ at $0°$ and $90°$ are provided at three $\psi$-tilts:  $90°$ (Figure 12(a)), $5°$ (Figure 12(b)) and $0°$  (Figure 12(c)) . In all cases $\alpha_i$ only equals $\psi$ when $\omega$ is at $90°$.  At $\omega=0°$, $\alpha_i$ is $0°$, irrespective of $\psi$.

35
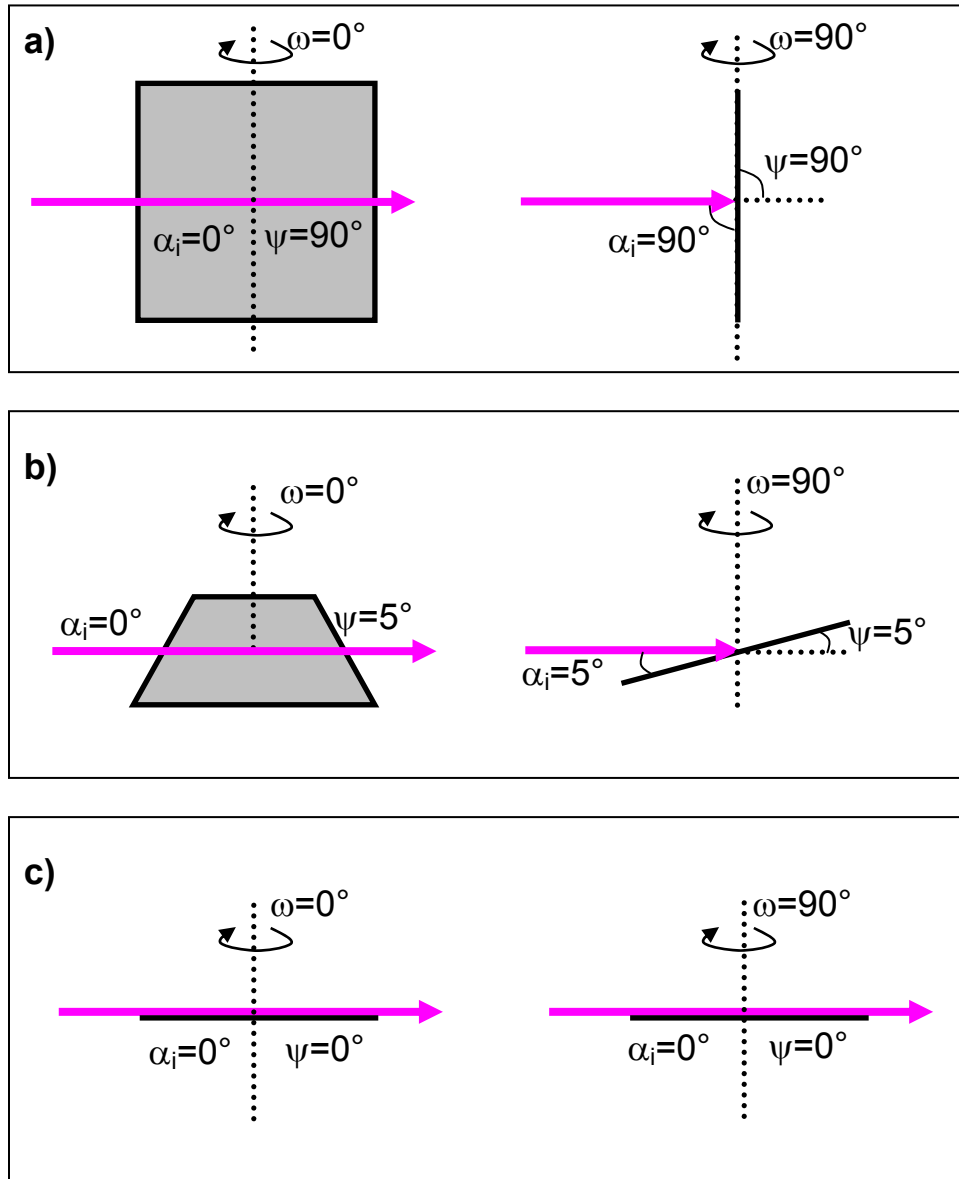
**Figure 12 Dependence of $\alpha_i$ on $\psi$ and $\omega$**

By inspection of Figure 12, the following conjecture for determining $\alpha_i$ may be deduced:

$$\alpha_i = \sin^{-1}(\sin\omega\sin\psi) \qquad (\,2\text{-}3\,)$$

For the encapsulated Cu and W films discussed here, reciprocal space scans were performed such that $Q_z$ remained constant and minimized, while $Q_x$ spanned the range

inclusive of all major Bragg reflections. Figure 13 presents the path taken through reciprocal space of a GID experiment calculated from equation ( 2-2 ) and ( 2-3 ), where λ=1.54Å.
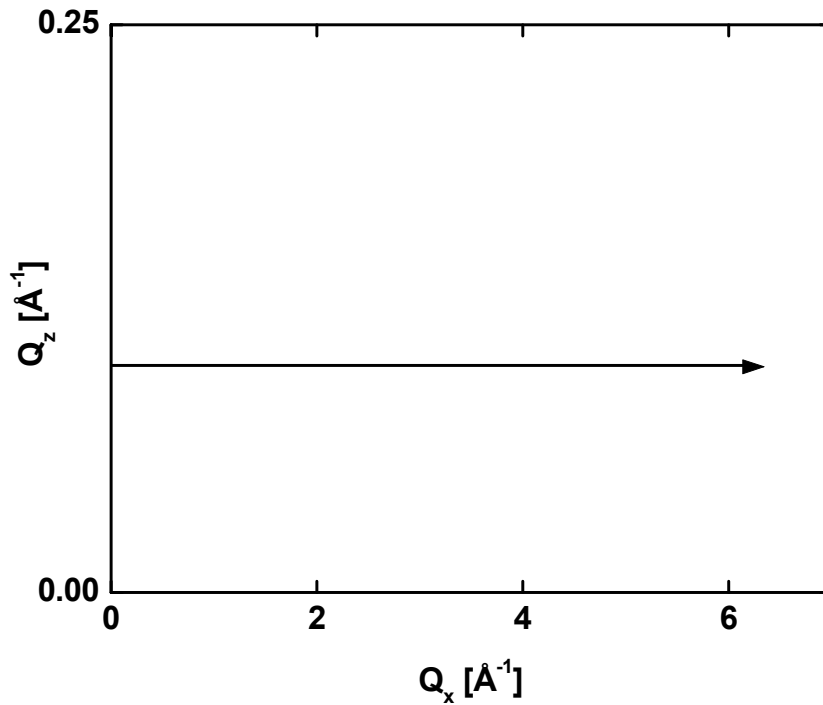


**Figure 13 GID trace through reciprocal space with constant $\alpha_i$**

A synchrotron source is ideal for GID experiments owing to its high spectral purity and high intensity. Accordingly, all diffraction experiments on encapsulated Cu and W thin films were performed at the Stanford Synchrotron Radiation Lightsource (SSRL). Data were collected on beam line 7–2. This beam line is equipped with a Huber 6+2 -circle diffractometer, and a He filled sample stage to decrease the air scattering

background. X-rays with a wavelength of  1.54 Å were monochromated with a double bounce Si(111) crystal.

### 2.2.2.2 X-ray Reflectivity

All X-ray reflectivity (XRR) experiments were also performed at SSRL.  Data were collected on thin-film diffraction beam line 2–1. This beam line is equipped with a Huber 2-circle goniometer, a pair of 1 mm slits as the analyzer, and a He filled sample stage to decrease the air scattering background. X-rays with a wavelength of 1.549 Å were monochromated with a double bounce Si(111) crystal. Three types of scans were performed in order to study the (top and bottom) interfacial roughness and its lateral correlation length.  To determine film thickness and RMS roughness (of top and bottom Cu interfaces), specular and offspecular scans were collected: for specular scans $\omega=2\theta/2=\theta$, whereas for off specular scans $\omega=2\theta/2 \pm0.15°$. The offspecular scans were used to subtract the contribution of diffusely scattered X-rays to the specular reflection, resulting in a purely specular reflectivity pattern. Data were collected for $2\theta$ values ranging between 0.2° to 12°, with a step size of 0.02°, 0.01°, or 0.005°, depending on film thickness.  To determine the lateral correlation length, rocking curves were collected by fixing the detector at approximately 3° of $2\theta$, and rocking the sample through $\pm1.5°$ of $\omega$. A $2\theta$ of 3° was chosen to obtain diffuse scattering that was sufficiently strong. The in plane component of the scattering vector was later determined by realizing that $Q_x=(4\pi/\lambda)\sin\theta\cos\theta$, and was subsequently modeled to determine the lateral correlation length of roughness.   The X-ray data was analyzed using Bede REFS software [Wormington *et al.* 1999].   Specular reflectivity profiles are modeled by inputting thickness, density and roughness values into REFS; necessary instrument parameters,

such as silt settings and X-ray wavelength, are also inputted.  A fitting routine is subsequently executed.  The measured values for thickness, density, and roughness are then used to model each corresponding diffuse reflectivity profile, which then only depends on vertical correlation length, vertical correlation fraction, and the fractal exponent.

2.2.3 Additional Characterization

The microstructure of these films were extensively studied by TEM; details have been published elsewhere [Sun 2009], [Choi 2011]. The following represents a summary:

The TEM samples were prepared using a back-etching technique [Yao *et al.* 2008] and examined by a combination of techniques. High angle annular dark field (HAADF) imaging in scanning TEM mode was used at relatively low magnifications to assess the void fraction present in the film.   In the case of Cu films, Hollow cone dark field (HCDF) TEM imaging was used to provide high diffraction contrast for grain size measurements which were based on a hand tracing method  [Sun 2009]. In the case of W films, an Automated Crystallography in the TEM (ACT) technique was employed. Details of the ACT technique may be found in the Doctoral Dissertation of Dooho Choi [Choi 2011].  The reported grain size is the diameter of the equivalent circle with area equal to the average of the grain areas and the errors on the mean are quoted as $2\sigma$ values at a 95% confidence level for the given grain population.  For samples in Table 14 (c) the reported grain size is an approximation based on resistivity data and film thicknesses measured by specular XRR.  This was made possible by previously published works which provide quantitative verification of the Myadas-Schotzkey model of resistivity [Sun *et al.* 2008], [Sun *et al.* 2009], [Sun *et al.* 2010].  The specimens whose grain size

was calculated based on resistivity are only included in x-ray reflectivity discussions pertaining to scaling dynamics.

**2.3 GlobalFoundries W**

2.3.1 Sample Preparation

Three W thin films specimens were processes by industrial partners at GlobalFoundries. These were deposited onto thermally oxidized Si substrates via chemical vapor deposition. Table 2 lists all processing details made available.

**Table 2 GlobalFoundries W processing details**

| ID | $SiO_2$ [Å] | $W_{Nucleation}$ [Å] | $W_{Coolfill}$ [Å] | $W_{CVD}$ [Å] | $W_{Total}$ [Å] |
|---|---|---|---|---|---|
| GF W 2 | 1000 | 23 | 111 | 0 | 134 |
| GF W 4 | 1000 | 23 | 0 | 106 | 129 |
| GF W 5 | 1000 | 23 | 29 | 75 | 127 |

2.3.2 X-ray Scattering

X-ray scattering investigations of W films from GlobalFoundries were performed using a grazing incidence diffraction (GID) geometry, similar to that described in section 2.2.2.1 X-ray Diffraction. In these experiments, the specimen was held at a constant inclination angle, $\psi=2°$: Real space, $\theta$-$2\theta$, scans were performed so as to include all major Bragg reflections. Because $\psi$ was held constant, $\alpha_i$ and $\alpha_f$ varied during the diffraction experiment; thereby resulting in a small change in $Q_z$. Figure 14 presents the path taken through reciprocal space of the GID experiment described here. Equation ( 2-2 ) and ( 2-3 ) were used to generate the trace, where $\lambda=1.54$Å and $\psi=2°$. The change in $Q_z$ is however small, and ultimately experimentally negligible: No corrections are made to the experimentally obtained diffraction profiles to accommodate the non-constant $Q_z$.
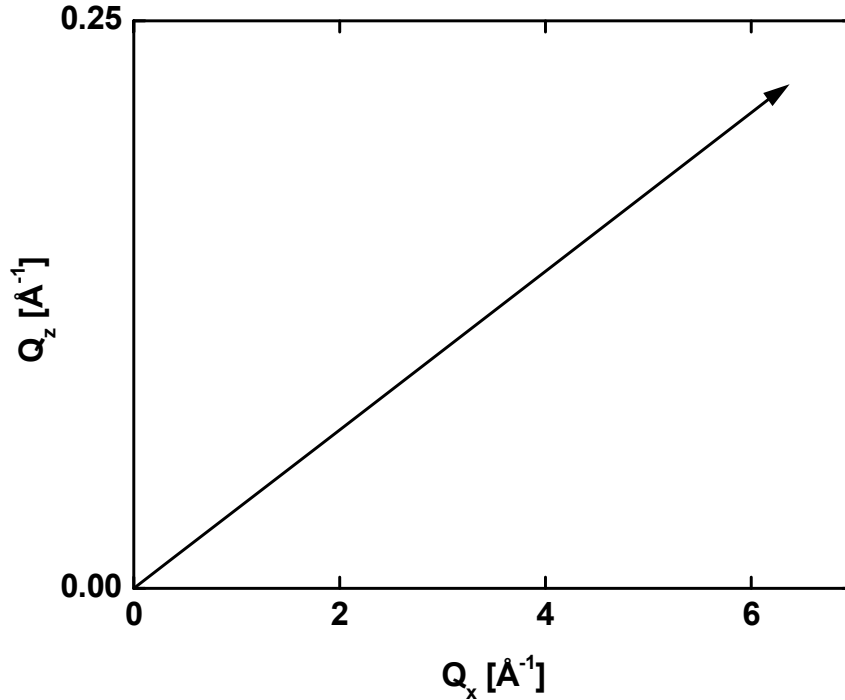
**Figure 14 GID trace through reciprocal space with constant ψ**

A X'pert Pro MRD diffractometer with Cu-Kα radiation was used for these investigations. The diffractometer is housed at Carnegie Mellon University. The diffraction patters were collected by Jason Wolfe and Xuan Liu in accordance with the experiments proposed by Andrew P. Warren. Measured diffraction patterns were analyzed as a function of scattering angle using a combination of software: OriginPro version 8, and Microsoft Excel 2003.

2.3.3 Additional Characterization

Thin film samples of W from Globalfoundries were extensively studied by transmission electron microscopy. These investigations comprise a significant portion of

Xuan Liu's doctoral dissertation; a student at Carnegie Mellon University, Pittsburg, PA (Advisor: Katayun Barmak).

Plan view electron transparent samples for TEM investigations were prepared by a back etch method [Yao *et al.* 2008]. Subsequent TEM analysis was preformed on a FEI Techni F20. Orientation maps were generated using a commercially available software package from NanoMEGAS: ASTAR[TM], and analyzed using the TSLOIM[TM]

# CHAPTER THREE :  METASTABLE PHASE IDENTIFICATION

The continued scaling of device dimensions in complementary metal-oxide-semiconductor (CMOS) technology in the sub 700Å  region requires an alternative high dielectric (high-κ) oxide layer to counter tunneling leakage currents, and a metallic gate electrode to address limitations of polysilicon [Wilk *et al.* 2001]. A key parameter for the choice of the metal gate material is its work function. For p-channel MOS (p-MOS), Pt and Ru are both possible choices due to their higher work function value. Alloys of these metals can also be considered to achieve an optimized or "tunable" work function. A detailed study of the resulting phases for a binary metal alloy system is important, as it can be expected to impact the important properties of the gate electrode material, such as its work function, electrical resistivity and thermal stability.  For FCC materials, the dependence of work function and lattice parameters on alloy composition has been demonstrated theoretically and corroborated experimentally [Abrikosov *et al.* 1993]. In this section, a detailed phase characterization of Pt-Ru binary alloy thin films performed predominantly by grazing incidence x-ray diffraction (GIXRD) is reported.

## 3.1 Objectives

The objective of this research is to gain insight into compositional dependence of crystallographic structure in Pt-Ru alloy thin films, and to understand its effect on the alloy's electronic work function.   This work additionally illustrates the continued relevance of x-ray diffraction for phase identification of simple binary alloy systems

**3.2 Results**

The structural dependence on composition can be seen in the GIXRD patterns and is qualitatively confirmed with electron diffraction. Figure 15 shows grazing incidence GIXRD of thin films spanning the compositional range from pure Pt to pure Ru where the intensities for each scan have been offset for clarity.

The pure Pt and pure Ru samples are clearly single phase FCC and HCP, respectively, and what is of interest is the transition from FCC to HCP that occurs at intermediate compositions. The lower angle reflections shown in Figure 15(a) reveal an FCC(111) peak for pure Pt that gradually shifts to higher angles and can ultimately be indexed as the HCP(002) peak in pure Ru. As this peak is common to both crystal structures, it cannot be used as evidence of the absence of either one of these two phases. However, the FCC(200) peak is unique to the FCC phase and it is observed to decrease in intensity with increasing Ru concentration and is not discernable in Figure 15(a) at compositions above 43 at% Ru. This observation is accompanied by the growth of the HCP(100) and (101) peaks with increasing Ru concentration. Both of these peaks are clearly present in the sample having 63 at. % Ru, and some indication of the HCP(101) peak is also present at 58 at. % Ru. The higher angle XRD peaks for these same samples (Figure 15(b)) clearly show the presence of the HCP phase at 58 at. % Ru, as the (103) peak is unique to the HCP phase. The HCP(103) peak intensity increases as the Ru concentration is increased. Also evident is the shift to higher angles of the FCC(331), and its splitting into HCP(112) and (201). Clearly, the 58 at. % Ru sample is at or near the transition with composition from FCC phase to HCP phase and warrants a more detailed examination.
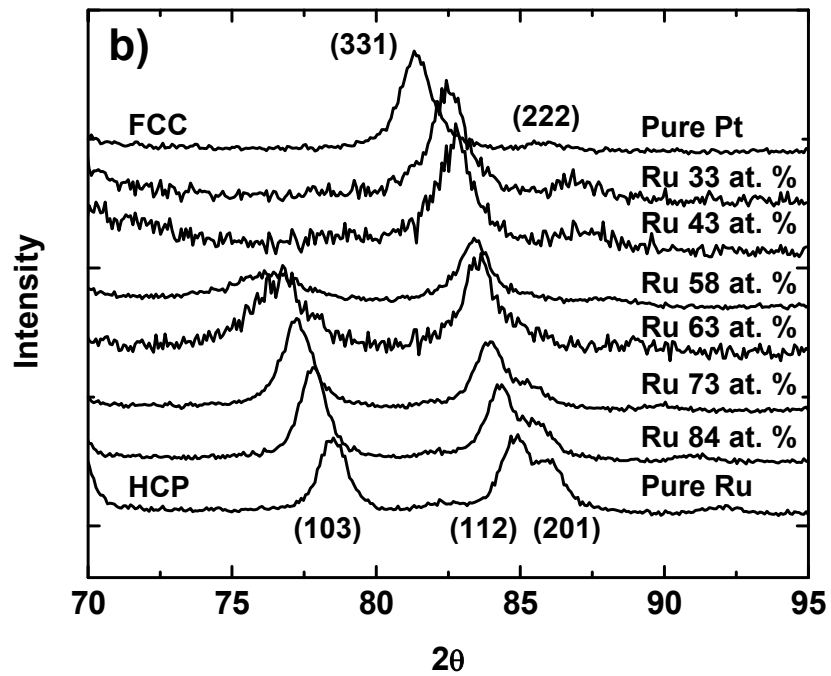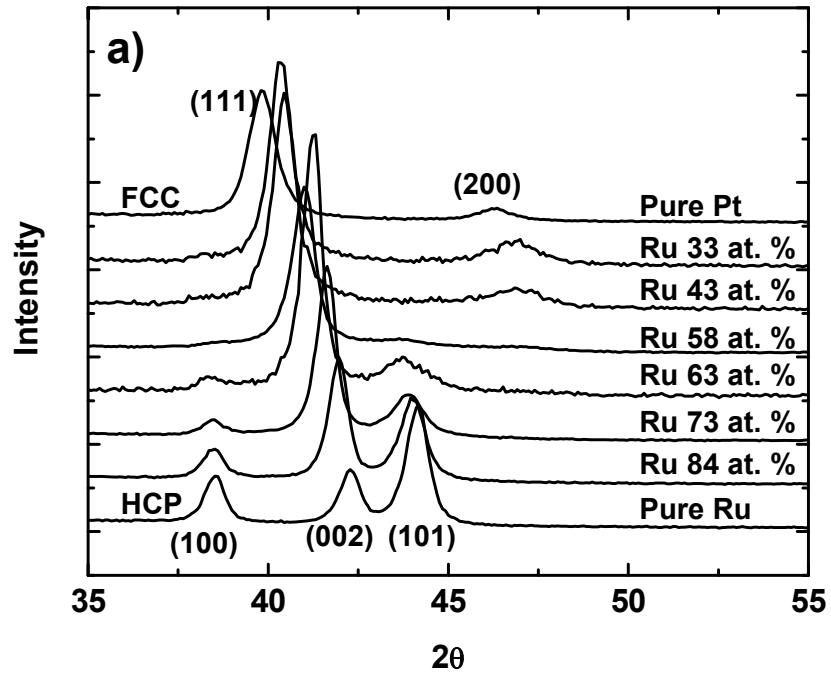
**Figure 15 Pt-Ru GIXRD**

Assessment of the sample with a 43 at. % Ru concentration (figure not shown) reveals asymmetries in the FCC(111) and FCC(200) peaks. We attribute these asymmetries to HCP(100) and HCP(101) respectively; thereby suggesting a dual phase microstructure at this composition that remains predominately FCC. Figure 16 shows the range from 35°2θ to 80°2θ of GIXRD measured for the 58 at. % Ru sample. The presence of both FCC and HCP phases is apparent, in that the FCC(200) peak remains a dominant feature of the diffraction pattern, while several HCP peaks are also present. The FCC(200) remains discernable, albeit less intense, for the sample with a 63 at. % Ru concentration (not shown) indicating some remaining FCC phase. Pt-Ru alloys with Ru concentrations higher than 63 at% have only discernable HCP phase peaks in both electron and X-ray diffraction.
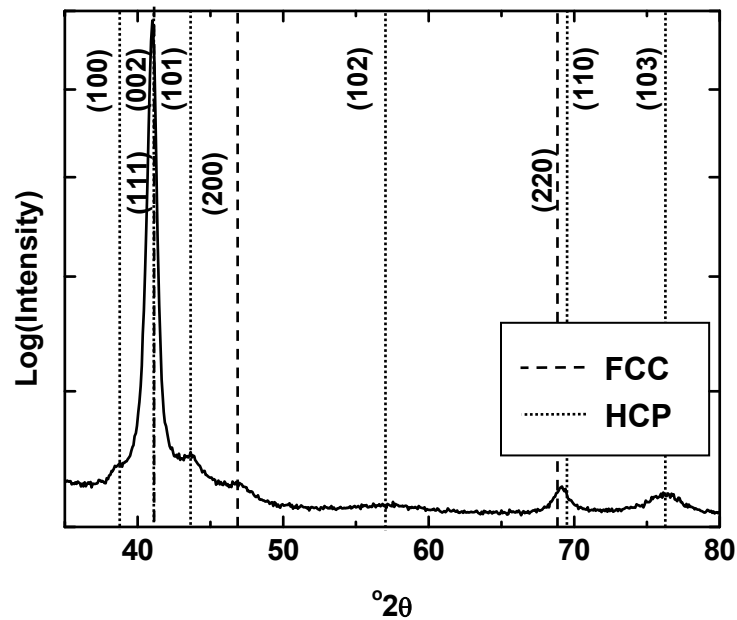


**Figure 16 Ru 58% alloy GIXRD**

46

The d-spacing and lattice parameters for the FCC and HCP phases were obtained from the XRD data. Figure 17 shows the shift of the d-spacing of the FCC(111) plane and subsequent HCP(002) plane as a function of Ru concentration.
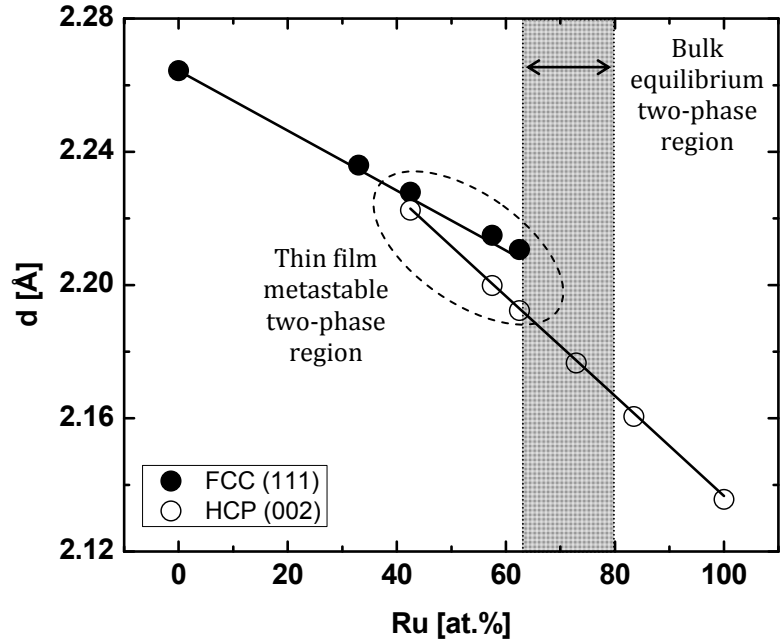


**Figure 17 Variation in lattice spacing with Ru concentration**

Increasing the Ru concentration causes the d-spacing of the FCC(111) plane to decrease linearly at a rate of $9 \times 10^{-4}$ Å/at%Ru, while the HCP(002) d-spacing decreases at a rate of $1.5 \times 10^{-3}$ Å/at%Ru. For samples with a discernable HCP phase, a proportional change in both lattice parameters (c and a) could not fully account for the measured change in all peak positions; therefore indicating a compositional dependence of the c/a ratio, as well. Figure 18 shows the measured c/a ratio as a function of Ru concentration, and the data follows a weakly quadratic trend.
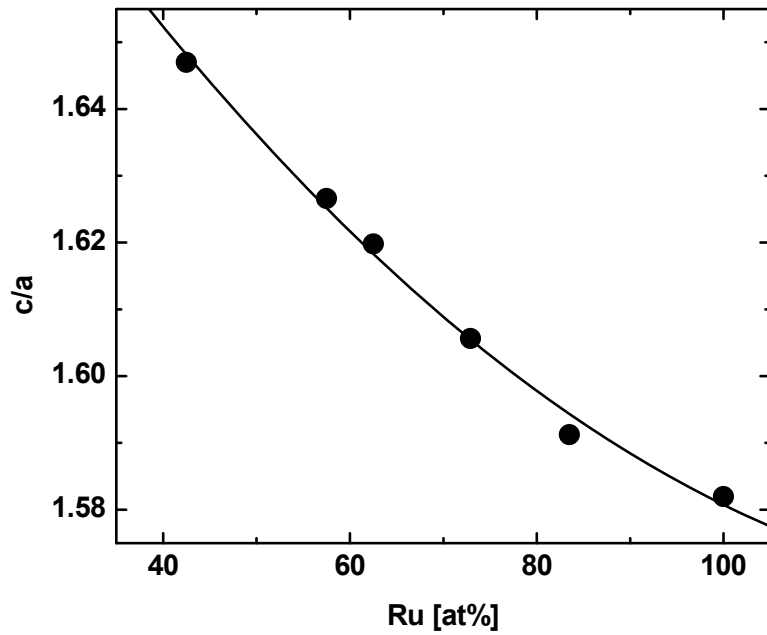
**Figure 18 Effect of composition on c/a ratio in HCP Pt-Ru films**

Figure 19 presents the results of measurements of the work function for these alloys as a function of composition, and a complex, non-linear, behavior is evident. The variation in work function follows the observed metastable extension of the HCP phase identified by GIXRD (Figure 17). Regions of weak compositional dependence are observed in the single-phase and near single-phase regions of the alloy thin films; marked as region A in Figure 19.
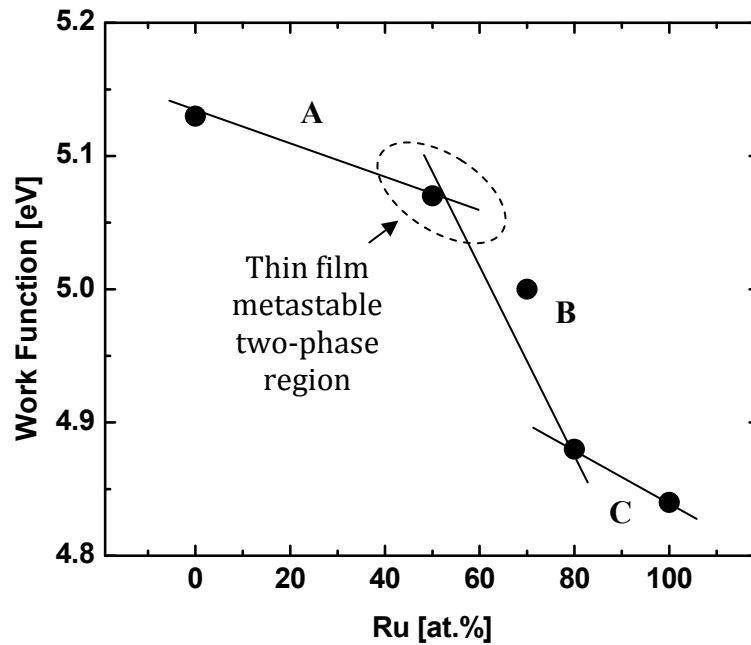
**Figure 19 Nonlinear work-function response to Ru concentration**

Steep compositional dependence is observed across the intermediate compositional range where the c/a ratio is observed to decrease most rapidly as Ru concentration is increased. (Figure 19, region B). The work function asymptotes to that of pure Ru as the concentration of Pt approaches 0 Figure 19, region C). Figure 20 shows the strong correlation between the electronic work function and c/a ratio of the HCP phase samples, where a linear relationship is observed.
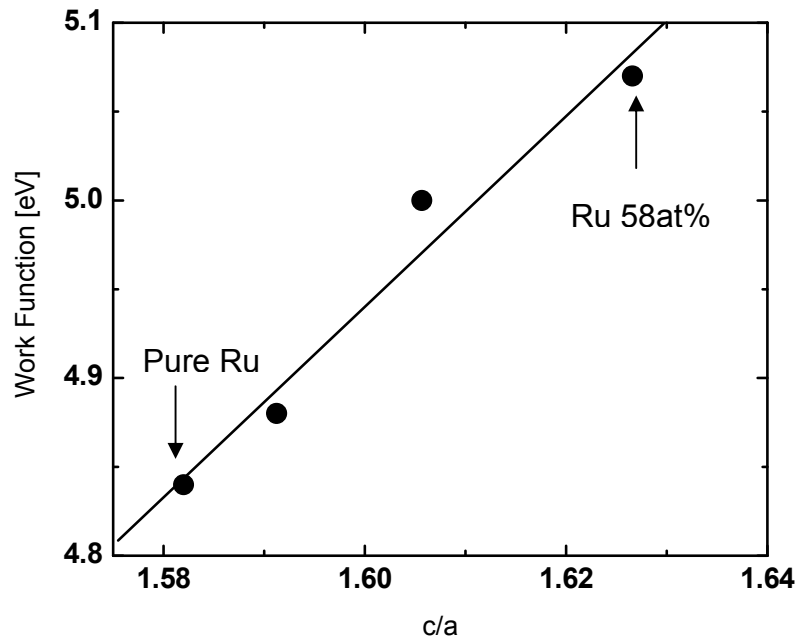
**Figure 20 Dependence of Pt-Ru Work Function on c/a ratio of HCP phase**

According to the equilibrium phase diagram for bulk Pt-Ru alloys [Massalski *et al.* 1990] , a Ru content of less than 62 at. % is expected to consist of only FCC phase, and Ru concentrations of more than 80 at. % are expected to be HCP. Both FCC and HCP phases of Pt and Ru are expected to be present for Ru concentrations between 62 and 80 at.%. However, structural analysis of the Pt-Ru thin film alloy system reveals a notable increase in the compositional range of the hexagonal close packed (HCP) phase, suggesting a metastable extension of the HCP phase stability as compared to bulk Pt-Ru alloys. A similar meta stable extension had been noted in RF sputtered electrodes studied in a GID geometry [Kim *et al.* 2005]. In the case of the thin films discussed herein, a mixed HCP-FCC phase becomes apparent with Ru concentrations as low as 43 at%. Furthermore, the FCC phase is completely absent (single phase HCP) for Ru

concentrations higher than approximately 65 at.%.   In addition to the metastable extension of the HCP phase, a gradual change of phase is apparent in the form of a linearly decreasing d-space of the FCC(111), and subsequent HCP(002) planes,  as the Ru concentration is increased.  A decrease in c/a ratio is also evident in the HCP phase.

## 3.3 Conclusion

Pt-Ru alloy thin films were sputter deposited in an ultra- high vacuum chamber by dc magnetron sputtering and were extensively characterized by GIXRD to quantify the phase dependence of the alloy composition in the Pt-Ru alloy thin films. The equilibrium binary phase diagram [Massalski *et al.* 1990] for bulk Pt–Ru alloys indicate a two-phase microstructure for compositions from 62 to 80 at.% Ru. However, for these thin films a notable increase in the compositional range of the HCP phase was observed, suggesting a metastable extension of the HCP phase stability as compared to bulk Pt-Ru alloys. The steepest change in the electronic work function for the intermediate alloy compositions coincided with a rapid change in the c/a ratio of the HCP phase.

# CHAPTER FOUR : GRAIN SIZE AND DEFECT ANALYSIS

X-ray line profile analysis has been used to investigate the grain size and microstructure of Cu and W thin films. Two distinct sets of W films will be discussed; those referred to as GlobalFoundries W (or GF-W) will be discussed separately at the end of this chapter, and are the only specimens investigated using a conventional diffractometer; all other experiments were performed using a synchrotron source.

Examples of normalized x-ray line profiles (circles) measured at SSRL, and their corresponding fits (solid line) are provided in Figure 21. Figure 21(a) shows an example Grazing Incidence Diffraction (GID) of a Cu film with a thickness of 1439Å and an in plane grain size (as measured by hollow cone dark field TEM methods) of 2480Å. This data corresponds to sample Cu-08 in Table 3, which summarizes the results of the peak fitting. Figure 21(b) shows an in-plane scan of a W film with a thickness of 189Å and an in plane TEM grain size of 1020Å. This data corresponds to sample W-01 in Table 3.
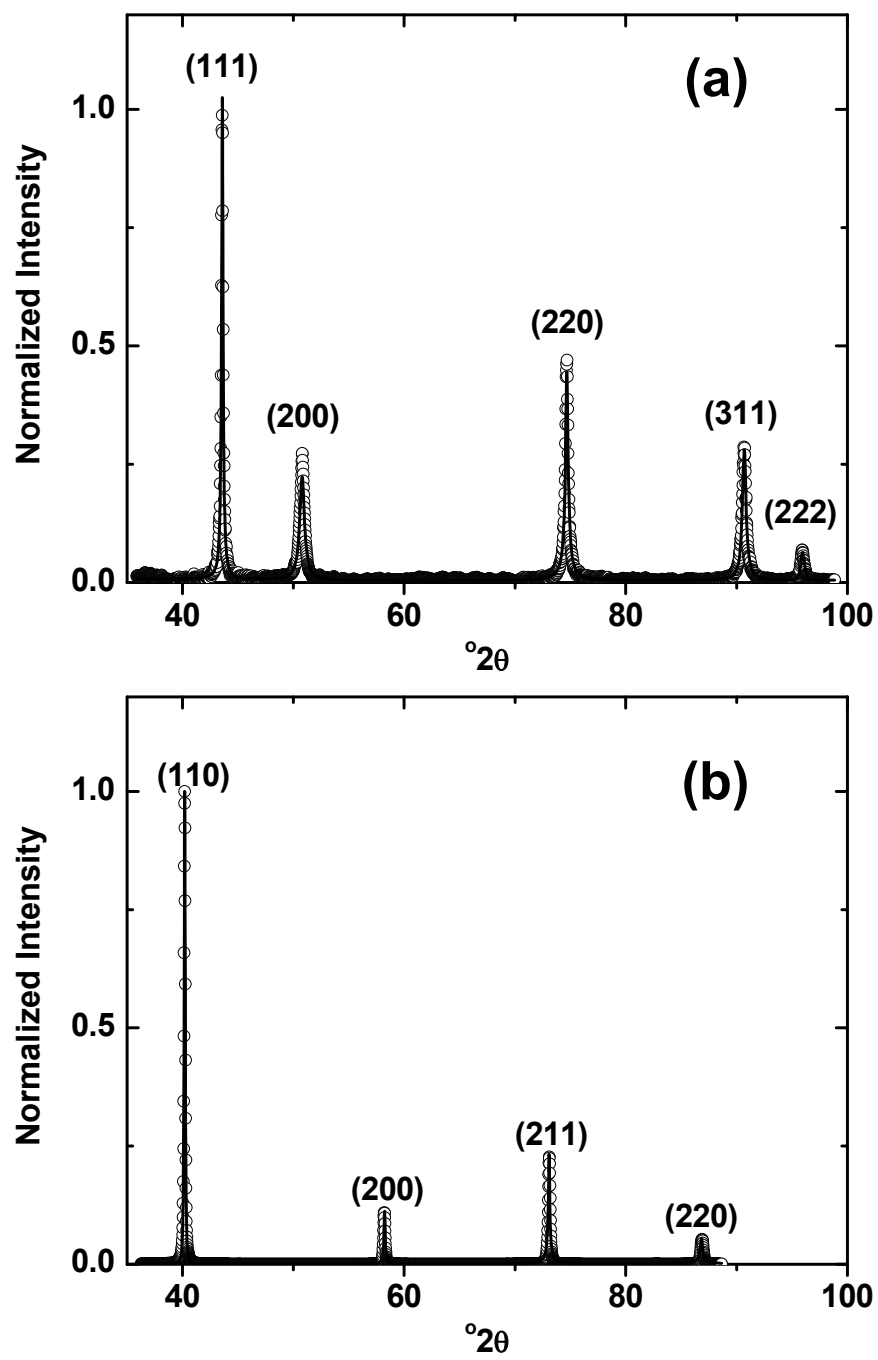
**Figure 21  Experimental and simulated (a) Cu and (b) W GID profiles**

The table includes measured values, in real space coordinates, of peak positions ($2\theta$) and FWHM($\Delta(2\theta)$) and the subscripts indicate the hkl values for each peak. Printed values of FWHM have not been corrected for instrumental broadening. As discussed previously, instrument effects may generally be neglected for these samples. Nevertheless, corrections for instrumental broadening, based on Figure 1, have been made in analysis of peak profiles for grain size, whose results will be presented in subsequent tables and figures.

The x-ray wavelength ($\lambda$), film thickness ($T_{XRR}$) and TEM-based values of grain size ($D_{TEM}$) are also included in Table 3. Thickness values were obtained through x-ray reflectively analysis, which is discussed extensively in chapter 4 which specifically includes samples Cu-01, Cu-02, Cu-05, and Cu-07.

Because the specimens discussed in the this section have comprised significant portions of works published elsewhere, Table 4 presents a list of alternative specimen identifications which may be used for cross correlations. This table should also be used as reference for any subsequent works which may be based on these sample sets.

**Table 3 Cu and W Peak Fitting Results**

| ID | $T_{XRR}$ [Å] | $D_{TEM}$ [Å] | $\lambda$ [Å] | $\Delta(2\Theta)_{111}$ [°2Θ] | $2\Theta_{111}$ [°2Θ] | $\Delta(2\Theta)_{200}$ [°2Θ] | $2\Theta_{200}$ [°2Θ] | $\Delta(2\Theta)_{220}$ [°2Θ] | $2\Theta_{220}$ [°2Θ] | $\Delta(2\Theta)_{331}$ [°2Θ] | $2\Theta_{311}$ [°2Θ] | $\Delta(2\Theta)_{222}$ [°2Θ] | $2\Theta_{222}$ [°2Θ] |
|---|---|---|---|---|---|---|---|---|---|---|---|---|---|
| Cu-01 | 270 | 405 | | 0.200 | 43.604 | 0.530 | 50.842 | 0.346 | 74.739 | 0.444 | 90.757 | 0.422 | 95.996 |
| Cu-02 | 336 | 684 | | 0.182 | 43.466 | 0.423 | 50.556 | 0.361 | 74.494 | 0.512 | 90.333 | 0.438 | 95.614 |
| Cu-03 | 371 | 648 | | 0.180 | 43.586 | 0.433 | 50.829 | 0.307 | 74.677 | 0.412 | 90.691 | 0.349 | 95.930 |
| Cu-04 | 417 | 877 | 1.549358 | 0.134 | 43.526 | 0.353 | 50.673 | 0.251 | 74.539 | 0.326 | 90.493 | 0.290 | 95.756 |
| Cu-05 | 451 | 1011 | | 0.121 | 43.552 | 0.335 | 50.696 | 0.167 | 74.580 | 0.237 | 90.549 | 0.223 | 95.821 |
| Cu-06 | 836 | 2215 | | 0.093 | 43.527 | 0.234 | 50.662 | 0.184 | 74.537 | 0.275 | 90.473 | 0.255 | 95.782 |
| Cu-07 | 1439 | 2480 | | 0.071 | 43.567 | 0.258 | 50.814 | 0.119 | 74.645 | 0.375 | 90.679 | 0.164 | 95.896 |

| ID | $T_{XRR}$ [Å] | $D_{TEM}$ [Å] | $\lambda$ [Å] | $\Delta(2\Theta)_{110}$ [°2Θ] | $2\Theta_{110}$ [°2Θ] | $\Delta(2\Theta)_{200}$ [°2Θ] | $2\Theta_{200}$ [°2Θ] | $\Delta(2\Theta)_{211}$ [°2Θ] | $2\Theta_{211}$ [°2Θ] | $\Delta(2\Theta)_{220}$ [°2Θ] | $2\Theta_{220}$ [°2Θ] |
|---|---|---|---|---|---|---|---|---|---|---|---|
| W-01 | 189 | 1020 | | 0.125 | 40.203 | 0.112 | 58.208 | 0.185 | 73.101 | 0.220 | 86.882 |
| W-02 | 283 | 1060 | | 0.128 | 40.198 | 0.164 | 58.211 | 0.200 | 73.096 | 0.256 | 86.885 |
| W-03 | 425 | 1010 | 1.540178 | 0.140 | 40.247 | 0.194 | 58.278 | 0.232 | 73.191 | 0.287 | 87.002 |
| W-04 | 607 | 1110 | | 0.134 | 40.285 | 0.189 | 58.324 | 0.216 | 73.270 | 0.266 | 87.104 |
| W-05 | 1229 | 1090 | | 0.124 | 40.271 | 0.183 | 58.330 | 0.200 | 73.263 | 0.243 | 87.095 |

**Table 4 Alternative Sample ID's**

| ID | Alternative ID | | |
|---|---|---|---|
| Cu-01 | -- | -- | N43_101006d_150 |
| Cu-02 | -- | -- | N43_101006d_600 |
| Cu-03 | -- | -- | N35_072106a_150 |
| Cu-04 | -- | -- | N35_072106a_400 |
| Cu-05 | -- | -- | N50_071606B_150 |
| Cu-06 | -- | -- | N50_071606B_400 |
| Cu-07 | -- | -- | N35_101006e_150 |
| -- | W3N5 | B5 | 1100 |
| -- | W3N10 | B10 | 1099 |
| W-01 | W3N20 | B20 | 1087 |
| W-02 | W3N30 | B30 | 1092 |
| W-03 | W3N40 | B40 | 1091 |
| W-04 | W3N60 | B60 | 1090 |
| W-05 | W3N120 | B120 | 1089 |
| W-06 | W3N180 | B180 | 1088 |

## 4.1 Objectives

The objective of this research is to examine the utility of conventional x-ray peak profile analysis methods for the determination of grain size and microstrain in metallic thin film specimens. Results are compared to TEM based investigations.

## 4.2 Results of Scherrer Analysis

The Scherrer method is the simplest method of line profile analysis. It is generally understood to provide only an approximation of crystallite size, owing mainly to the fact that it fails to account for strain broadening. Nevertheless, the method is still widely used and provides many insights into the microstructure of a system. Results of Scherrer analysis are presented in Table 5. Scherrer grain sizes were obtained using equation ( 1-6 ) and values from Table 3 after correcting for instrument broadening as per equation ( 1-2 ) and Figure 1 (solid line). For every sample, two Scherrer grain sizes are reported: These values represent grain sizes obtained with and without empirical shape

factor optimization (discussed in following section).  XRR based thickness values and TEM based grain size values are included for reference.

**Table 5 Results of Scherrer Analysis**

| ID | $T_{XRR}$ [Å] | $D_{TEM}$ [Å] | $D_S$ (K=1.00) [Å] | $D_S$ (K=1.55) [Å] |
|---|---|---|---|---|
| Cu-01 | 270 | 405 | 480 | 745 |
| Cu-02 | 336 | 684 | 528 | 819 |
| Cu-03 | 371 | 648 | 534 | 828 |
| Cu-04 | 417 | 877 | 721 | 1118 |
| Cu-05 | 451 | 1011 | 801 | 1242 |
| Cu-06 | 836 | 2215 | 1052 | 1631 |
| Cu-07 | 1439 | 2480 | 1403 | 2175 |
| W-01 | 189 | 1020 | 759 | 1176 |
| W-02 | 283 | 1060 | 741 | 1148 |
| W-03 | 425 | 1010 | 676 | 1048 |
| W-04 | 607 | 1110 | 707 | 1096 |
| W-05 | 1229 | 1090 | 765 | 1186 |
| W-06 | 1801 | 1160 | 778 | 1206 |

4.2.1 Grain Size

Scherrer analysis was performed on the first order reflection with maximum intensity; i.e. the (111) for FCC Cu and the (110) for BCC W. A shape factor (k=1) was assumed. The maximum grain size that was found to be reliably measurable is herein reported to be on the order of 1200Å. Such a resolution limit is common, and its source is typically attributed to instrumentation. It is reported that when the average TEM based grain size approaches 2000Å, Scherrer analysis yields squared errors that are one hundred times higher than that for 1200Å grained specimens. Specifically, Scherrer-based analysis yields squared errors on the order of $10^4$ for grains up to approximately 1200Å; These errors increase to an order of $10^6$ for larger grained specimens.

Recall however, that a synchrotron source was implemented for these experiments, so as to render the contribution of instrument broadening negligible.

Indeed, based on the measured instrument resolution, (0.02°2θ at 43°2θ), a grain size of nearly 0.5μm should be quantifiable. Instrumental broadening therefore cannot be confirmed to be the source of the observed 1200Å grain size limit.

The data and hypothetical perfect correspondence to TEM based values are plotted in Figure 22 where filled and half-filled circles represent Cu and W films respectively. Open circles represent (Cu) outliers whose x-ray based measures of grain size significantly deviate from expected values. A total sum of the errors squared of $3.3 \times 10^6$ is reported for the data plotted in Figure 22.
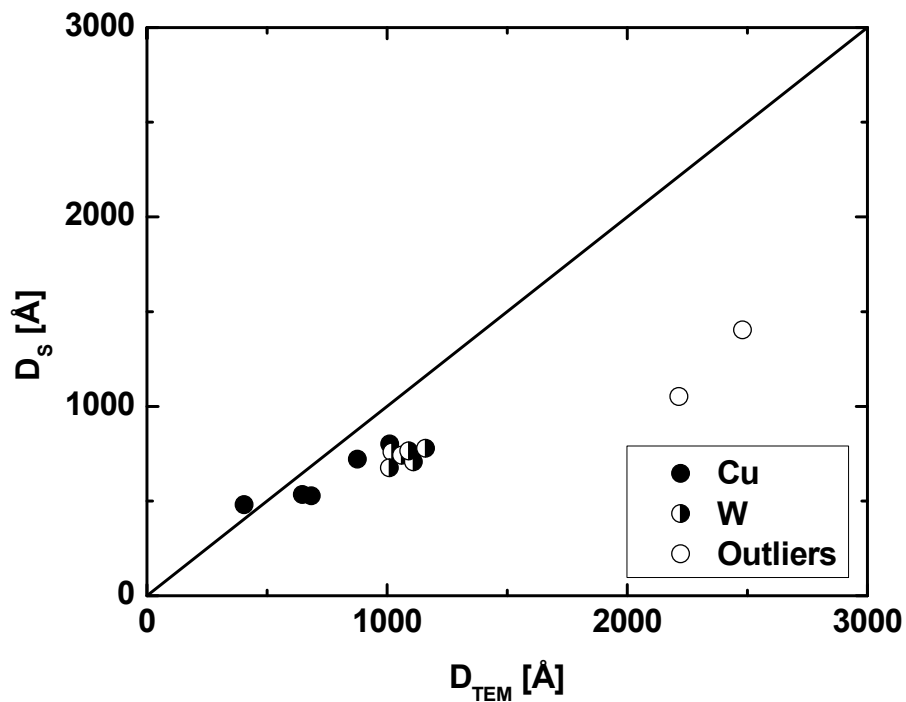


**Figure 22 Scherrer and TEM Grain Size Comparison**

4.2.2 Shape Factor

Having the unprecedented grain size analysis obtained through exhaustive TEM studies, the Scherrer equation has been used to experimentally evaluate the shape factor

59

for Cu and W thin films measured in-plane.  Regression methods were used to minimize the sum squared error between TEM and Scherrer grain size values. Using this approach, a shape factor (k) equal to 1.55 was found to provide the best correlation between TEM and XRD results.

Typical values for the shape factor are 0.88 (when the peak integral breath is used in analysis), 0.94 (when the peak full-width at half-maximum is used in analysis) or 1 (reasonable approximation) [Warren 1990].  More rigorously obtained values were published by Langford and Wilson [Langford *et al.* 1978].  Langford and Wilson present k values that depend on crystallite shape and hkl.  The authors contend that "crystallites are usually irregular in shape, but on average they maybe regarded as having a regular external form."  They continue "If the crystallites making up the specimen have a reasonably well defined shape, and if this shape has a reasonably well defined relation to the crystal axis, the numerical value of the Scherrer constant will depend on the index of reflection."

For (110) (BCC W specimens) and (111) (FCC Cu specimens) reflections specifically, whose full-width at half-maximum is used for analysis, shape factor values ranging between 0.83 and 0.95 are expected according to Langford and Wilson. Similarly, shape factors for platelets have been reported as 0.886 [Smilgies 2009].  The experimentally obtained value however is 1.55.  Limited data prevents an assessment of a dependence on reflection index.  However, a global value of 1.55, applied to Scherrer analysis of both Cu and W thin films, presents a significant improvement in grain size results when compared to TEM based measurement.  Figure 23 shows TEM grain sizes plotted against that obtained through Scherrer analysis.  The solid line represents a

hypothetical perfect correspondence for reference. By inspection, X-ray based grain sizes analyzed using a shape factor of 1.55 lie more closely along the solid line than do grain sizes analyzed with a shape factor of 1.00. To quantify; using k=1.00 provides a sum squared error of $3.3 \times 10^6$. Using k=1.55 however, reduces the sum squared error to $7.6 \times 10^5$.
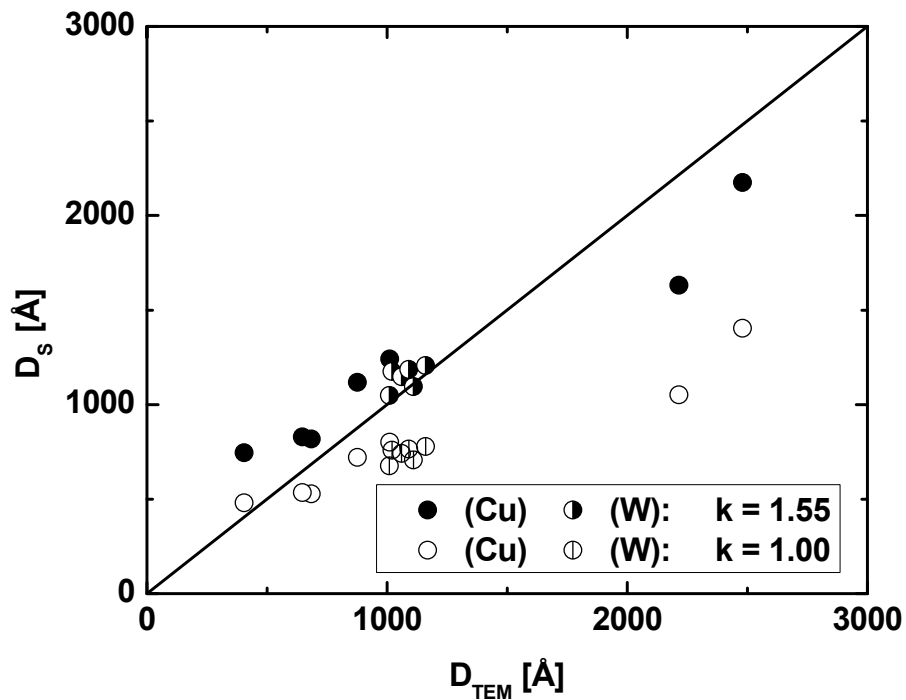


**Figure 23 Optimized Scherrer shape factor showing improved agreement between GID and TEM grain size values.**

The fact that the experimentally determined shape factor exceeds the anticipated value may be attributed to the highly irregular crystallite shape. From plan view TEM micrographs it is apparent that the crystallites do not have a well defined shape, and no obvious correlation exists between crystallite shape and crystallographic orientation To

highlight this point Figure 24(a) shows a hollow cone dark field (HCDF) image of sample Cu-03, and Figure 24(b) shows a bright field (BF) image of W-01. Additionally, Scherer's analysis assumes that the only mechanism responsible for peak broadening is grain size. Therefore stain-related broadening effects are folded into the shape factor; rendering it more aptly referred to as a "scaling factor."



100nm

TEM Courtesy of Bo Yao; UCF

a)
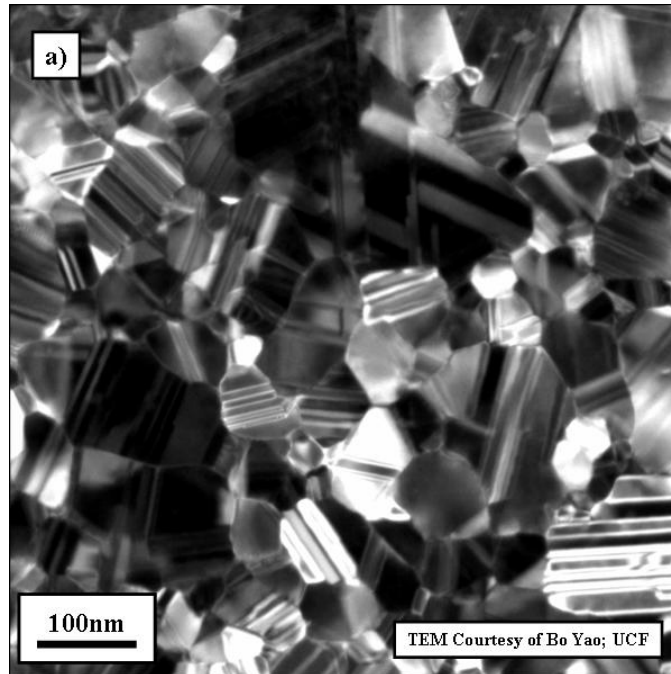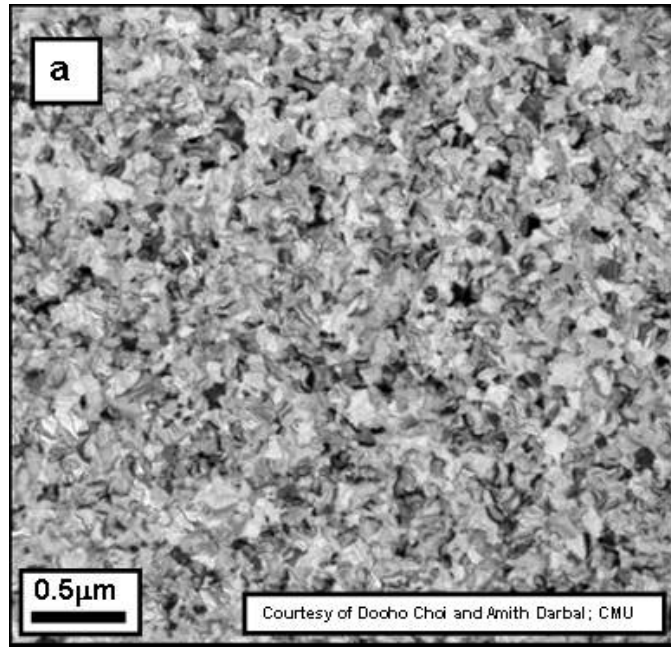
**Figure 24 (a) Cu-03 HCDF, (b) W-01 BF**

## 4.3 Results of Williamson-Hall Analysis

To further investigate x-ray peak profile broadening, the Classical and Modified Williamson-Hall methods were employed. Because significant micro-strains (variance in lattice spacing) are well known to contribute to peak broadening, analytical methods that are strain-sensitive may provide measures of grain size that more closely match that obtained by direct TEM studies. In the event that more reliable grain size values are not obtained by these more sophisticated methods, it is shown that non-negligible, yet under-researched, strains induced by interface phenomena, do indeed contribute to peak broadening. The results of Williamson-Hall (W-H) and modified Williamson-Hall (ModW-H) analysis are summarized in Table 6. Tabulated values include classical Williamson-Hall grain sizes ($D_{W-H}$) modified Williamson-Hall grain sizes ($D_M$), and micro-strain, i.e., the slope of the Williamson-Hall plot ($\varepsilon_{WH}$) and modified Williamson-

63

Hall plot ($\varepsilon_M$). XRR based thickness and TEM based grain size values are again included for reference.

**Table 6 Results of Williamson-Hall analysis**

| ID | $T_{XRR}$ [Å] | $D_{TEM}$ [Å] | $D_{W-H}$ [Å] | $\varepsilon_{WH}$ | $D_M$ [Å] | $\varepsilon_M$ |
|---|---|---|---|---|---|---|
| Cu-01 | 270 | 405 | 987 | 2.2E-03 | 727 | 5.4E-03 |
| Cu-02 | 336 | 684 | 1990 | 2.9E-03 | 1368 | 8.1E-03 |
| Cu-03 | 371 | 648 | 872 | 1.5E-03 | 901 | 5.1E-03 |
| Cu-04 | 417 | 877 | 1598 | 1.6E-03 | 1282 | 4.4E-03 |
| Cu-05 | 451 | 1011 | 1148 | 7.9E-04 | 1100 | 2.1E-03 |
| Cu-06 | 836 | 2215 | -- | 1.9E-03 | 3077 | 4.5E-03 |
| Cu-07 | 1439 | 2480 | 3729 | 9.3E-02 | 2816 | 2.4E-03 |
| W-01 | 189 | 1020 | 1140 | 9.9E-04 | 1390 | 2.8E-03 |
| W-02 | 283 | 1060 | 1566 | 1.6E-03 | 1631 | 4.2E-03 |
| W-03 | 425 | 1010 | 1568 | 1.9E-03 | 1591 | 5.1E-03 |
| W-04 | 607 | 1110 | 1457 | 1.6E-03 | 1425 | 4.4E-03 |
| W-05 | 1229 | 1090 | 1504 | 1.4E-03 | 1417 | 3.9E-03 |
| W-06 | 1801 | 1160 | 1400 | 1.3E-03 | 1357 | 3.4E-03 |

## 4.3.1 Classical Williamson-Hall

In attempting Classical Williamson-Hall analysis, it was found that strain anisotropy prevented the Williamson-Hall plot from revealing the expected monotonic function of peak width with Bragg angle, in both Cu (Figure 25(a)) and W (Figure 25(b)) films. The investigation is therefore limited to analysis of the (111) and (222) reflections (Figure 25(c)) for Cu and (110) and (220) reflections for W (Figure 25(d)).

**Figure 25 Classical Williamson-Hall plots of Cu (a, c) and W (b, d)films. (a, b) Strain anisotropy prevents monotonic function of peak width with Bragg angle. Only peak belonging to a single family of reflections are used (c, d)**

Results of grain size analysis by the Classical Williamson-Hall method are plotted in Figure 26, where filled and half-filled circles again represent Cu and W films respectively. By inspection, the correlation between TEM and XRD grain size values is less apparent than obtained from Scherrer analysis. To quantify the correspondence between TEM and Williamson-Hall based masseurs of grain size, a total sum squared error of $5.1 \times 10^6$ is reported. The open circle in Figure 26 represent one of two outliers identified in the previous section. Additionally, sample Cu-06 was calculate to have a negative Williamson-Hall grain size: Non-physical, negative grain size values have been excluded from Table 6, Figure 26, and error summations.
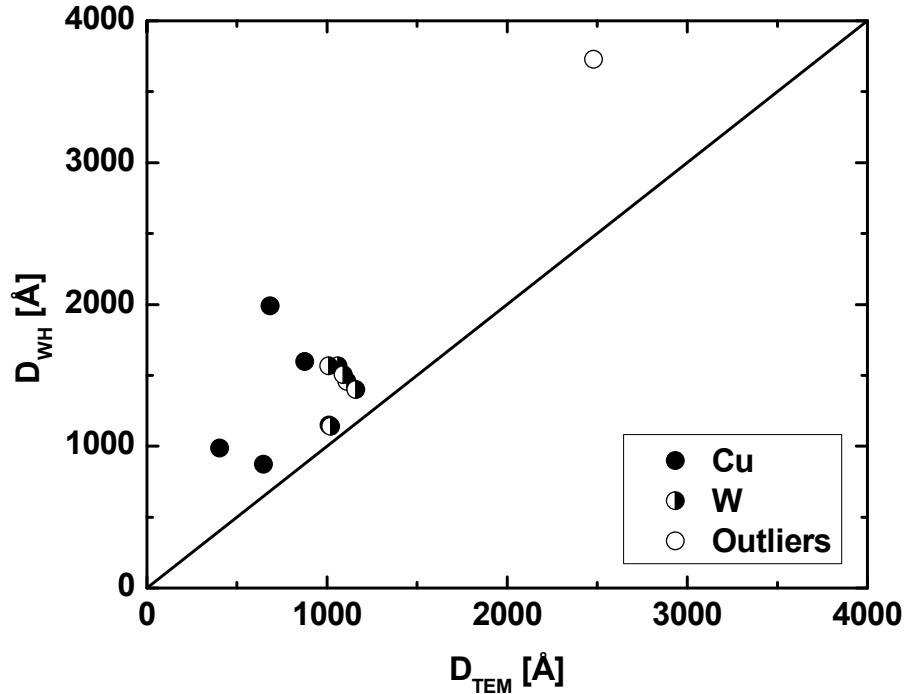
**Figure 26 Williamson-Hall and TEM grain size comparison**

Recall that Williamson-Hall analysis was explored to obtain more accurate measures of grain size by accounting for strain broadening in addition to grain size broadening. The fact that grain size values differ more considerably from TEM values for the Williamson-Hall analysis than for the Scherer analysis suggests that broadening mechanisms are not properly represented in the Williamson-Hall expression.

This is partially evident by the fact that strain anisotropy prevents those reflections not belonging to a single family from being considered. Therefore, the resulting "grain size" is more closely representative of a coherent x-ray scattering domain. This domain size is normal to the (111) planes in Cu and (110) planes in W, which are situated in the sample plane and whose variance in lattice spacing is loosely represented by the slope of the Williamson-Hall plot.

Evidence that broadening mechanisms are not properly treated in the Williamson-Hall method additionally exists in the fact that that physical interpretation of the strain as defined in equation ( 1-7 ) is vague:  Its source cannot be attributed to any defect type specifically.  Exploration of a modified Williamson-Hall method is warranted, wherein the microstrain is attributed to dislocations specifically.

4.3.2 Modified Williamson-Hall

Figure 27 (a,b) again present classical Williamson-Hall plots wherein all available reflections are plotted to reveal data scattered by strain anisotropy. Figure 27 (c,d) rescale the x-axis of the Williamson-Hall plots by the dislocation contrast factor [Ungár *et al.* 1996].  By inspection, this modified Williamson-Hall method provides improved confidence in the measured slope and intercept of data's linear fit, in comparison to the classical method.

An inherent assumption in the modified Williamson-Hall method is that strain broadening is caused by dislocations.  To generate the modified Williamson-Hall plots, dislocation contrast values were calculated uniquely for each reflection (equation ( 1-12 )).  Edge and screw dislocations were assumed to exist in equal amounts, and necessary physical constants for dislocation contrast factor calculations were found in literature [Overton *et al.* 1955], [Ungár *et al.* 1999].
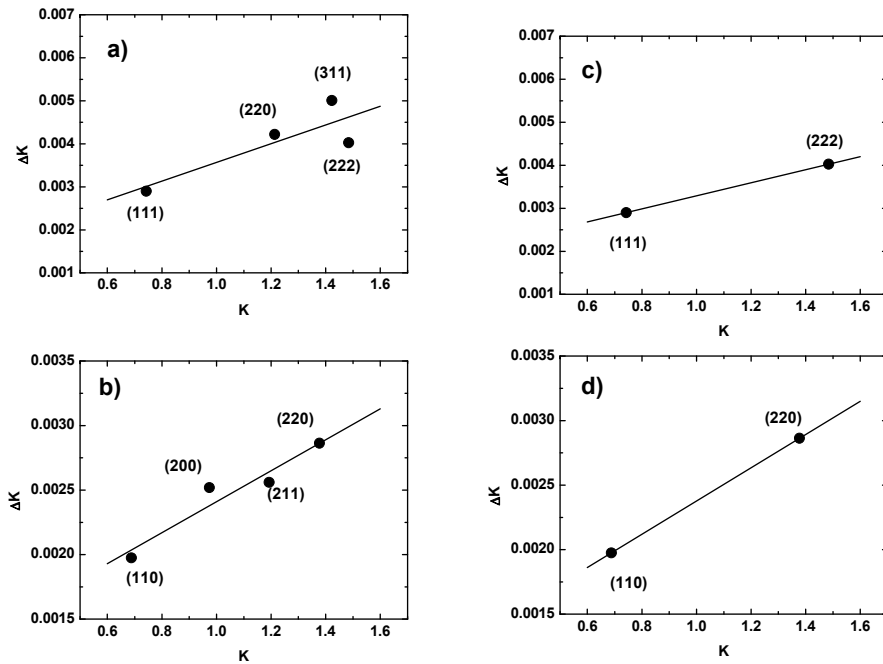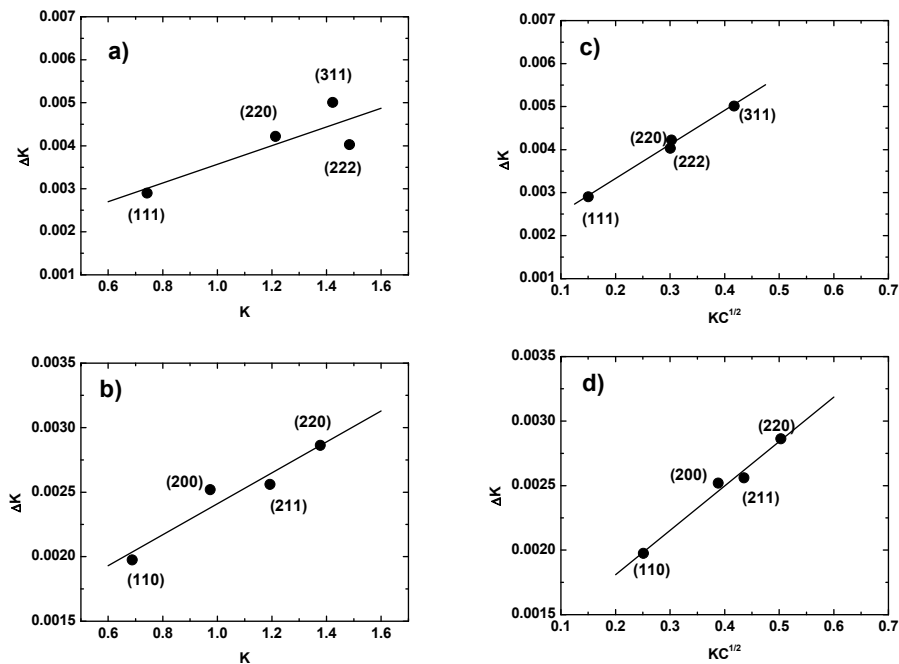
**Figure 27 Classical Williamson-Hall plots of Cu (a) and W (b) films: Strain anisotropy prevents monotonic function of peak width with Bragg angle. Modified Williamson-Hall plots of Cu (c) and W (d) films: Sscaling the peak position by the dislocation contrast reveals a monotonic function of peak width with Bragg angle.**

Comparing the grain size as determined by the modified Williamson-Hall method provides an improved correlation to TEM data over the classical Williamson-Hall method (Figure 28). As in previous figures, filled and half-filled circles represent Cu and W films respectively.

To quantify the correspondence between TEM and Modified Williamson-Hall measures of grain size a total sum squared error of $2.7 \times 10^6$ was determined. The improved correlation between TEM and XRD is significant when comparing the classical and modified methods; indicating a significant contribution from dislocations to the broadening of diffraction peaks. Nevertheless, the error obtained by the Modified Williamson -Hall approach approach is still in excess of that obtained by the Scherrer method. Therefore, while the Modified Williamson-Hall method attempts to attribute

stain broadening to physical sources of lattice distortion, the resulting grain sizes deviate from actual values by an amount large enough so as to provides little advantage over Scherrer first-order approximation.
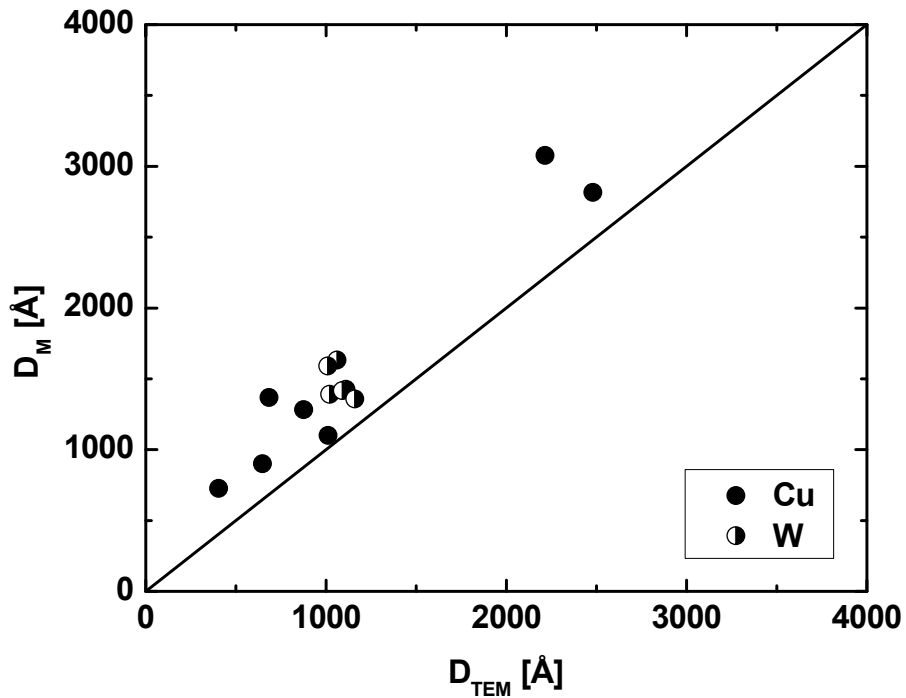


**Figure 28  Modified Williamson-Hall Grain Size**

## 4.4 Effects of Microstrain

The significant discrepancy between TEM and XRD measures of grain size indicates the present of other mechanisms contributing significantly to peak broadening. Because variations in lattice spacing have long been associated with peak broadening, the contribution of microstrains to x-ray peak width are discussed in the context of thin films

on substrates.  These are investigated in a novel manner, wherein the strain contribution to peak width is isolated by first obtaining grain size directly from TEM.

4.4.1 Residual FWHM

TEM micrographs of Cu and W films in Figure 29 reveal considerable differences in microstructures:  The Cu specimen (Figure 29(a)), is a hollow cone dark field image, used for TEM grain size analysis (Courtesy of Bo Yao; UCF) and corresponds to sample Cu-03.   The specimen is shown to possess an abundance of twins.    Figure 29(b),correspond to a Orientation Index Map (OIM) of a W film, specifically sample W-03, and was analyzed by ASTAR$^{TM}$ (Courtesy of Xuan Liu; CMU).  The micro structure of Cu and W films clearly differs in that the W film lacks the abundant twin boundaries that are apparent the Cu film.

Due to the varied defect structures observed between Cu and W films, coupled with the fact that neither classical nor modified Williamson-Hall methods are able to provide accurate grain size values, it may be expected that the x-ray line profile broadening methods employed simply fail to accurately accommodate strain broadening. Further investigations however reveal that this is not a proper conclusion.

a)

100nm

TEM Courtesy of Bo Yao; UCF



b)

200nm

TEM Courtesy of Xuan Liu; CMU
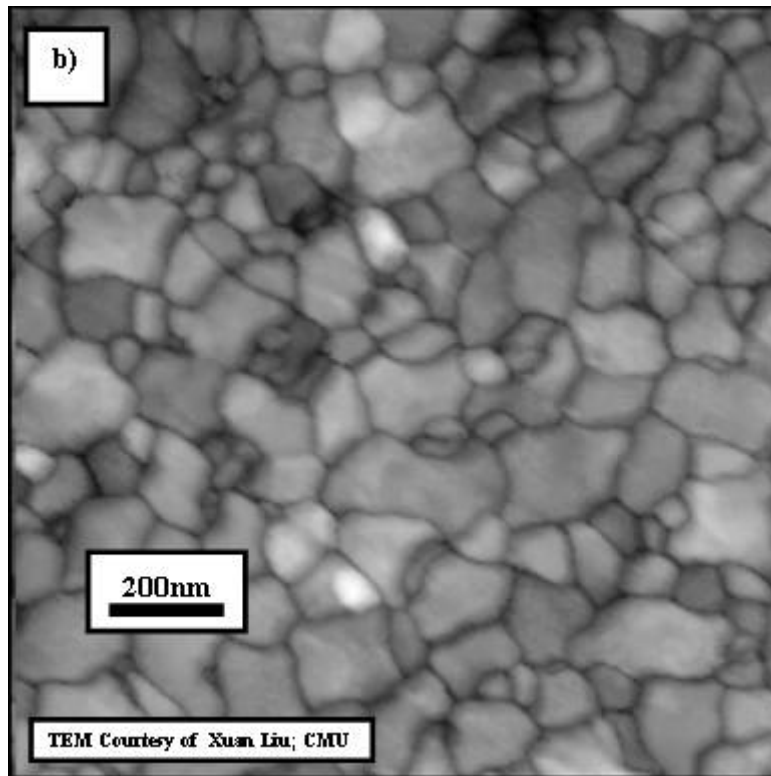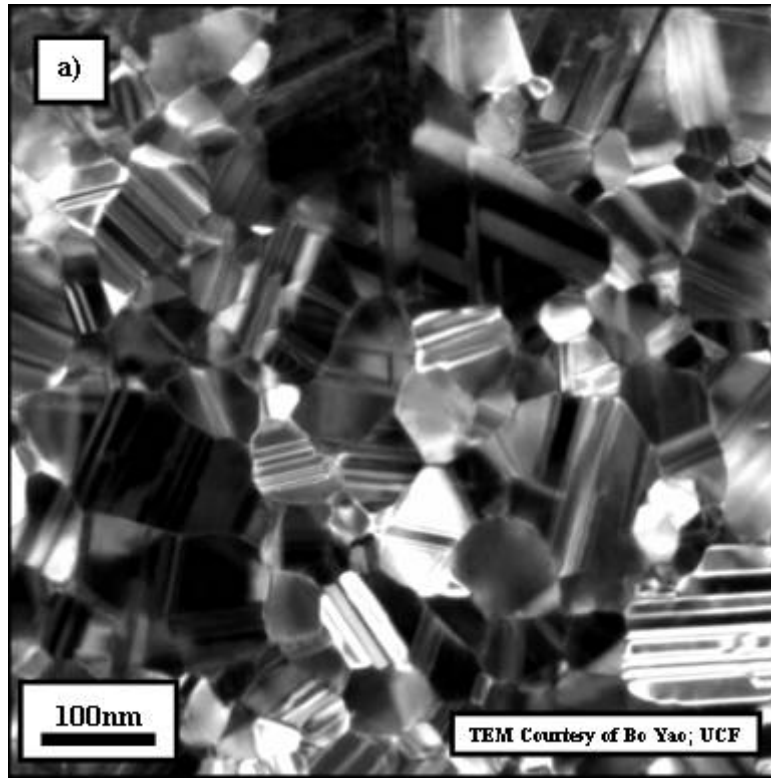
**Figure 29 (a) Cu-03 HCDF, (b) W-03 ASTAR OIM**

To assess the degree to which the slope of the modified Williamson-Hall plots correlate to strain-like broadening, let it be assumed that the measured peak width represents a Gaussian convolution of grain size, instrumental, and residual (strain-like) components:

$$\Delta(2\theta)_{Measured} = \sqrt{\Delta(2\theta)^2_{GrainSize} + \Delta(2\theta)^2_{Instrument} + \Delta(2\theta)^2_{Residual}} \quad \text{( 4-1 )}$$

Having measured peak widths and instrumental broadening, the TEM grain size may be used to calculate the residual peak width. This residual FWHM corresponds to "extra" broadening, not accounted for in instrumentation or grain size; it therefore offers a unique perspective on microstrain contributions to peak broadening. In the present discussion, the second order reflection was considered for residual FWHM analysis; i.e. the measured FWHM of a Cu(222) or W(220) reflection was used to determine grain size and strain broadening contributions to the respective reflection. This approach was used because higher order reflection are known to be more affected by strain effects than are first order reflections. Calculated values for of residual FWHM ($\Delta(2\theta)_{Res}$) are provided in Table 7.

**Table 7 Residual FWHM**

| ID | $T_{XRR}$ [Å] | $D_{TEM}$ [Å] | $\Delta(2\theta)_{Res}$ [°2θ] |
|---|---|---|---|
| Cu-01 | 270 | 405 | 0.260 |
| Cu-02 | 336 | 684 | 0.389 |
| Cu-03 | 371 | 648 | 0.277 |
| Cu-04 | 417 | 877 | 0.241 |
| Cu-05 | 451 | 1011 | 0.171 |
| Cu-06 | 836 | 2215 | 0.241 |
| Cu-07 | 1439 | 2480 | 0.144 |
| W-01 | 189 | 1020 | 0.177 |
| W-02 | 283 | 1060 | 0.223 |
| W-03 | 425 | 1010 | 0.255 |
| W-04 | 607 | 1110 | 0.237 |
| W-05 | 1229 | 1090 | 0.209 |
| W-06 | 1801 | 1160 | 0.200 |

The microstrain, as defined by the slope of the modified Williamson-Hall method, strongly correlates to the calculated residual FWHM (Figure 30), and may be fitted by a line with the following equation:

$$\Delta(2\theta)_{Residual} = 38.627\varepsilon_M + 0.0662 \qquad \textbf{( 4-2 )}$$

This strong correlation is indication that dislocations are indeed the primary defect contributing to microstrains in these thin films, and are responsible for limiting grain size analysis. The Cu specimens previously labeled "outliers" (Figure 22) also conform to the trend set by all other Cu and W data. Figure 30 and its implications are discussed further in the following section in terms of dislocation core spreading.
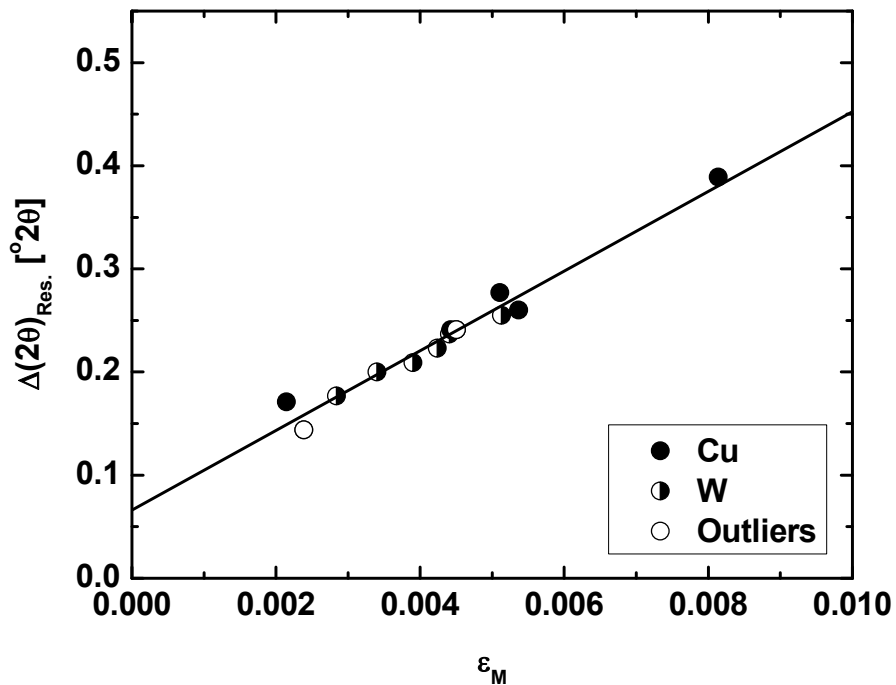


**Figure 30 Residual FWHM closely tracks the Modified Williamson-Hall micro-strain: This indicates a contribution of dislocations to x-ray peak width.**

While Figure 30 provides strong indication that dislocations, as determined by the modified method of Williamson-Hall, contribute significantly to x-ray peak broadening, the fact that the tend is linear with a non-zero intercept is noteworthy. Figure 31 replots the data set presented in Figure 30, with superimposed curves indicating the expected contributors of microstrain to peak broadening. Assuming four grain sizes (a) 250Å, b)500Å, c) 1000 Å and d) $10^{10}$Å), the slope of the modified Williamson-Hall plot was calculated for various microstrains. The peak broadening contribution of those microsatrins was thus determined according the residual width method described above.
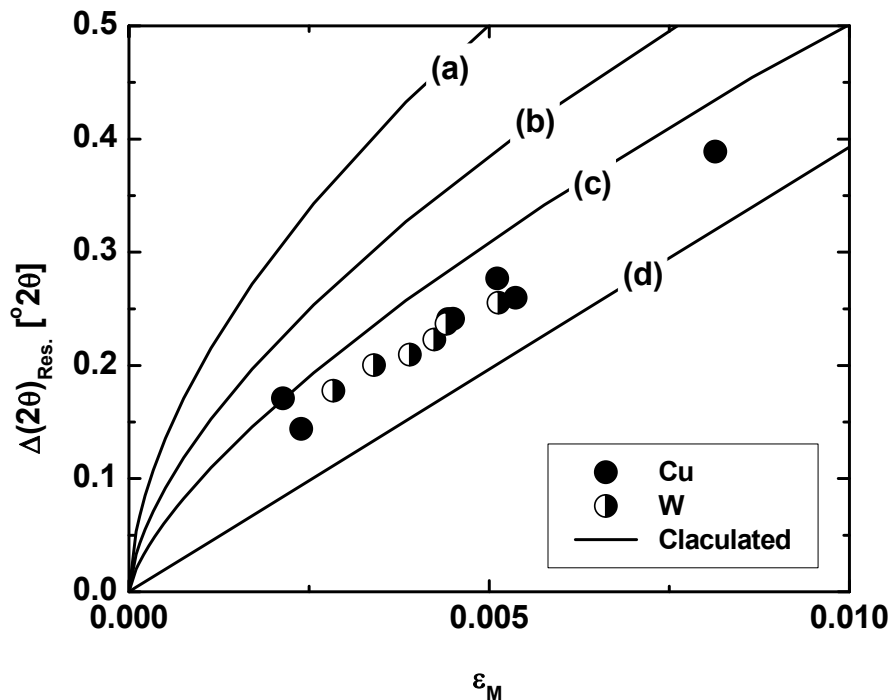


**Figure 31 Contribution of microstrain to x-ray peak broadening. Circles indicate data, solid lines represented calculated contributions for grain sizes of a) 250Å b)500Å c) 1000 Å d) $10^{10}$Å**

Because Cu and W data follow a single linear trend, despite the fact that they span a range of grain sizes and microstrains, indicates that peak broadening mechanisms

74

in these thin films are not completely described by the modified Williamson-Hall method. Nevertheless, the strong correlation between microstrain and residual width is evidence of a significant and systematic microstrain contribution to peak width.

4.4.2 Dislocation Core Spreading

The attribution of strain broadening to dislocations, as described in the modified Williamson-Hall method, results in an excellent correlation between the residual FWHM and modified Williamson-Hall slope for all Cu and W films (Figure 30). This strong correlation is noteworthy and warrants further discussion.

Figure 30 presents a dilemma in that the presence of dislocations is strongly evident; yet recalling Figure 29, TEM observations are unable to support these conclusions. The lack of observable dislocations in the TEM micrographs of Figure 29 may be attributed to the complex contrast exhibited in both figurers. Additionally, the hollow cone dark field and ASTAR imaging methods used to generate the Cu and W micrographs respectively may not be optimized for dislocation studies. In either case, these TEM studies cannot be used to confirm a contribution of dislocations to x-ray peak broadening. Additionally, the modified Williamson-Hall method resulted in grain size values whose correspondence to TEM measures was poorer than that obtained by Scherrer analysis. The validity of the modified Williamson-Hall method can therefore easily be disregarded for thin films, though doing so would be premature.

In addition to the aforementioned imaging-based limitations to detecting dislocations in these Cu and W specimens, it is hypothesized that dislocation core spreading at the film/substrate interface may be additionally impeding their observance by TEM. The disappearance of dislocation contrast is not without precedent [Müllner *et*

75

*al.* 1998].  Müllner et. al. reported dislocations along interfaces in Al systems which were seen to disappear under electron beam irradiation:  The disappearing contrast was attributed to spreading of the dislocation core.

The fact that thin films often exhibit unique mechanical properties has often been attributed to dislocations.  In most descriptions, dislocations are treated as 1-dimentional, compact defects.  The concept of dislocation core spreading was however described as early as 1949 [Eshelby 1949].   A theoretical considerations of the spreading of dislocation cores at film/substrate interfaces were published over 50 years later [Gao *et al.* 2002].  Figure 32 illustrates a simple example of an edge dislocation at an interface. When the adhesion (or coherency) between film and substrate is high, the dislocation will remain compact.  Such is the case with epitaxial films (Figure 32(a)). In the case of an edge dislocation at a film/(amorphous) substrate interface, where adhesion and coherency are low (Figure 32(b)) viscous sliding may take place between film and substrate, allowing the otherwise compact core to spread into many infinitesimal dislocations (Figure 32(c)).   The significance of  dislocation core spreading on the mechanical properties of thin films was discussed in a recent review paper [Wang *et al.* 2011].
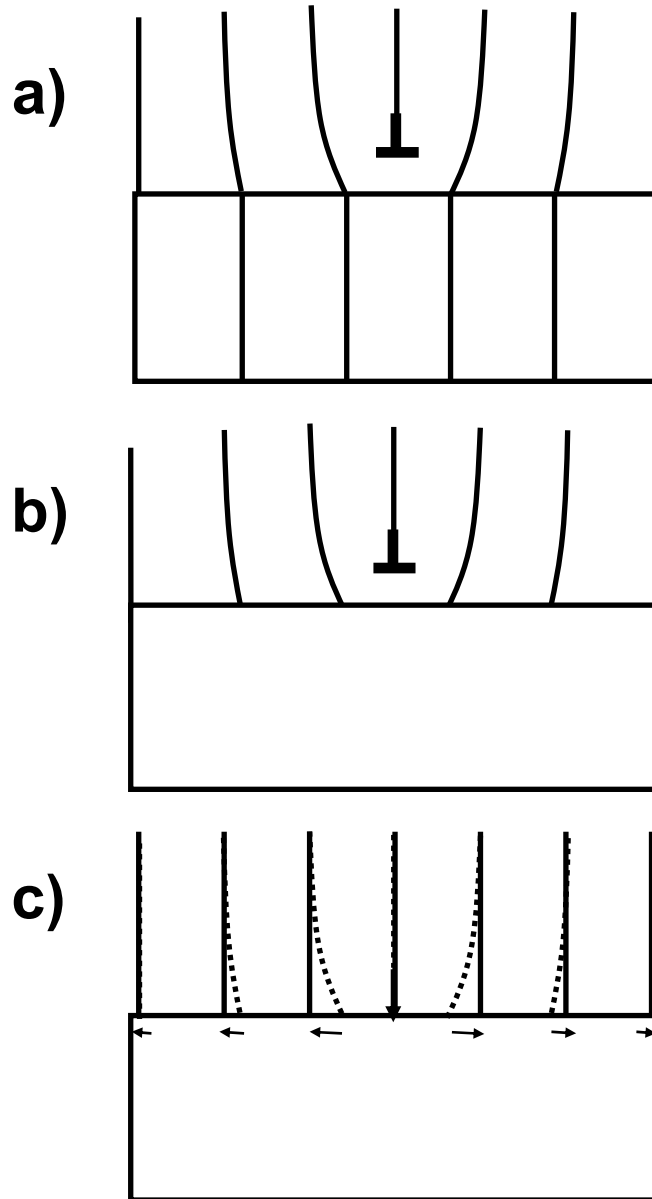
**Figure 32 Edge Dislocation at a film/substrate interface (a) epitaxial interface with compact dislocation core, i.e. a point defect (b) An edge dislocation at a crystalline/amorphous interface (c) a spread dislocation core at a crystalline/amorphous interface**

The extent of dislocation core spreading was characterized by Gao, and select solutions to equilibrium core widths have been published [Gao *et al.* 2002], [Gupta 2005]. Equation ( 4-3 ) represents the equilibrium core width for edge dislocations in an

array separated by a distance $L_\rho$. Figure 33 presents a schematic where the dotted circles represent the width of a spread edge dislocation core along a film/substrate interface.
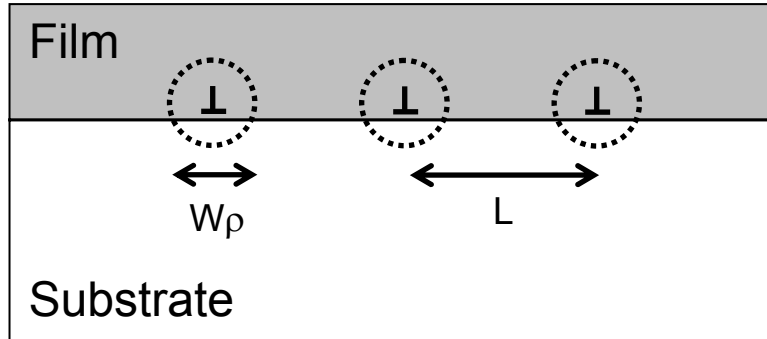


**Figure 33 Spread edge dislocation cores of width $W_\rho$ in array separated by a distance L**

In equation ( 4-3 ), the amorphous substrate and metallic film are assumed to have equivalent mechanical properties, i.e. Young's modulus (E) and Poisson's ratio ($\nu$). The interface strength is represented by $\tau_0$, which was taken to equal 140MPa for Cu and 153MPa for W: This is based on adhesion studies in damascene Cu structures [Lanckmans *et al.* 2002]. The Burgers vector (b) was calculated to equal 2.55Å for Cu using a lattice parameter of 3.61Å and the [110] close pack direction. For W, b is calculated to equal 2.74Å using a lattice parameter of 3.16Å and the [111] close pack direction. Bulk values of E and $\nu$ were assumed for Cu and W.

$$W_\rho = \frac{L}{\pi} \sin^{-1}\left[ \tanh\left( \frac{\pi Eb}{8(1-\upsilon^2)\tau_0 L} \right) \right] \qquad \text{( 4-3 )}$$

The distance between dislocations ( $L_\rho$ ) was determined from the dislocation density ($\rho_M$), which was calculated from the slope of the modified Williamson-Hall plot and equation ( 1-14 ):

$$L_\rho = \rho^{-1/2} \qquad \text{( 4-4 )}$$

Using equations ( 4-3 ) and ( 4-4 ), equilibrium core widths have been calculated for all Cu and W samples and the results are summarized in Table 8, which additionally includes calculated dislocation densities and dislocation separations.

**Table 8 Dislocation in Cu and W films**

| ID | $\rho_M$ [m⁻²] | $L_\rho$ [Å] | $W_\rho$ [Å] |
|---|---|---|---|
| Cu-01 | 1.9E+13 | 2308 | 355 |
| Cu-02 | 4.3E+13 | 1522 | 338 |
| Cu-03 | 1.7E+13 | 2426 | 356 |
| Cu-04 | 1.3E+13 | 2798 | 359 |
| Cu-05 | 3.0E+12 | 5777 | 367 |
| Cu-06 | 1.3E+13 | 2752 | 359 |
| Cu-07 | 3.7E+12 | 5192 | 366 |
| W-01 | 5.3E+12 | 4364 | 365 |
| W-02 | 1.2E+13 | 2924 | 360 |
| W-03 | 1.7E+13 | 2415 | 356 |
| W-04 | 1.3E+13 | 2810 | 359 |
| W-05 | 9.9E+12 | 3178 | 361 |
| W-06 | 7.5E+12 | 3640 | 363 |

Core widths are found to\ be on the order of  300Å, irrespective of film thickness, grain size or crystallographic structure (Figure 34 (a)).

The fact that core widths are essentially constant with thickness (not shown) and (TEM) grain size (Figure 34), means that outliers from previously discussed grain size data may be accounted for:  Figure 34(b) indicates that Scherrer grain size analysis becomes limited as a grains becomes populated with multiple dislocations.  It may thus be hypothesized that dislocations contribute to coherency disruptions, which contribute to the poor correlations between TEM and X-ray based grain size metrology methods.
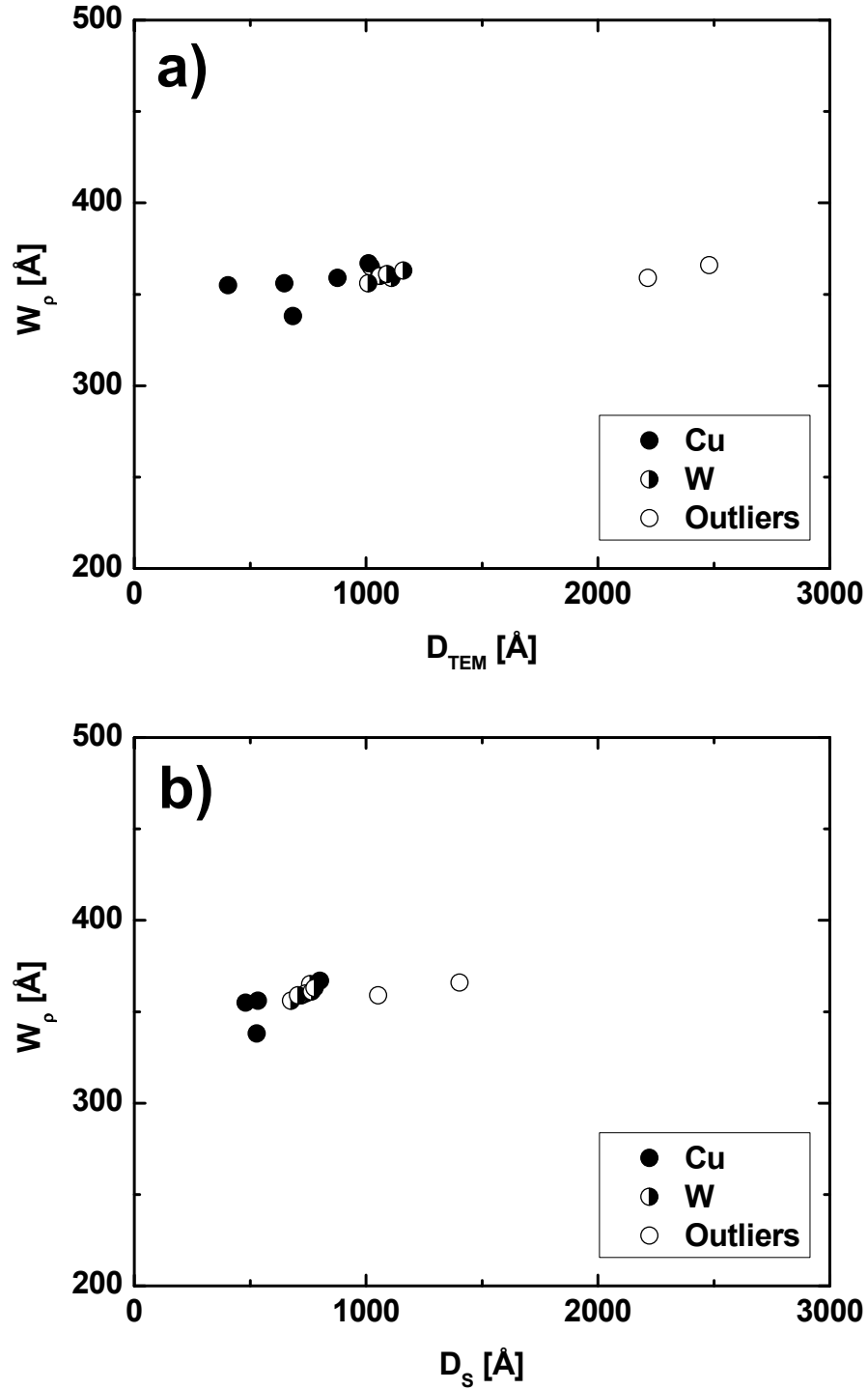
**Figure 34 Dislocation Core Width and Grain Size.  The core width is constant with (a) TEM and (b) Scherrer grain size.  The Scherrer grain size becomes limited as the real grain size, i.e. the TEM grain size, becomes large enough so as to accommodate multiple dislocation cores.**

## 4.4.3 Intra-Grain Misorientations

To further elucidate the effect of dislocation core spreading at film/substrate interfaces and its effect on x-ray profile analysis, a yet un-discussed sample set of W thin films will now be considered. The specimens currently under discussion have been prepared by Global Foundries.

**Table 9 GF-W Peak fitting results**

| ID | $\lambda$ [Å] | $\Delta(2\Theta)_{110}$ [°2$\Theta$] | $2\Theta_{110}$ [°2$\Theta$] | $\Delta(2\Theta)_{220}$ [°2$\Theta$] | $2\Theta_{220}$ [°2$\Theta$] |
|---|---|---|---|---|---|
| GF W 2 | | 0.575 | 40.095 | 0.996 | 86.613 |
| GF W 4 | Cu-K$\alpha$ | 0.756 | 40.163 | 1.696 | 86.826 |
| GF W 5 | | 0.66 | 40.146 | 1.342 | 86.771 |

The sample set is limited to three specimens wherein complete TEM and XRD data sets were available for comparison. Results of peak profile fitting are presented in Table 9. Results of grain size analysis (Scherrer analysis with k=1.00, and Modified Williamson-Hall); the slope of the modified Williamson-Hall plot; calculated values of residual FWHM; dislocation density; average dislocation separations; and equilibrium dislocation core width are listed in Table 10. Film thicknesses and TEM grain sizes are also included.

**Table 10 GW-W results of X-ray Line Profile Analysis**

| ID | $T_{Total}$ [Å] | $D_{TEM}$ [Å] | $D_S$ (k=1.00) [Å] | $D_M$ [Å] | $\varepsilon_M$ | $\Delta(2\Theta)_{Res.}$ [°2$\Theta$] | $\rho_M$ [m$^{-2}$] | $L_\rho$ [Å] | $W_\rho$ [Å] |
|---|---|---|---|---|---|---|---|---|---|
| GF W 2 | 134 | 830 | 192 | 383 | 0.016 | 0.938 | 2E+14 | 676 | 234 |
| GF W 4 | 129 | 820 | 135 | 962 | 0.039 | 1.663 | 1E+15 | 278 | 133 |
| GF W 5 | 127 | 810 | 160 | 572 | 0.028 | 1.299 | 7E+14 | 391 | 174 |

High quality TEM images and corresponding inverse pole figure maps of the three GF-W samples discussed above have been collected using ASTAR (Courtesy of Xuan Liu): Figure 35 shows representative orientations maps of GF-W samples -02, -04, and -05 in Figures (a), (b) and (c) respectively. False color is indicative of crystallographic orientation; a key is provided in Figure 35(d).
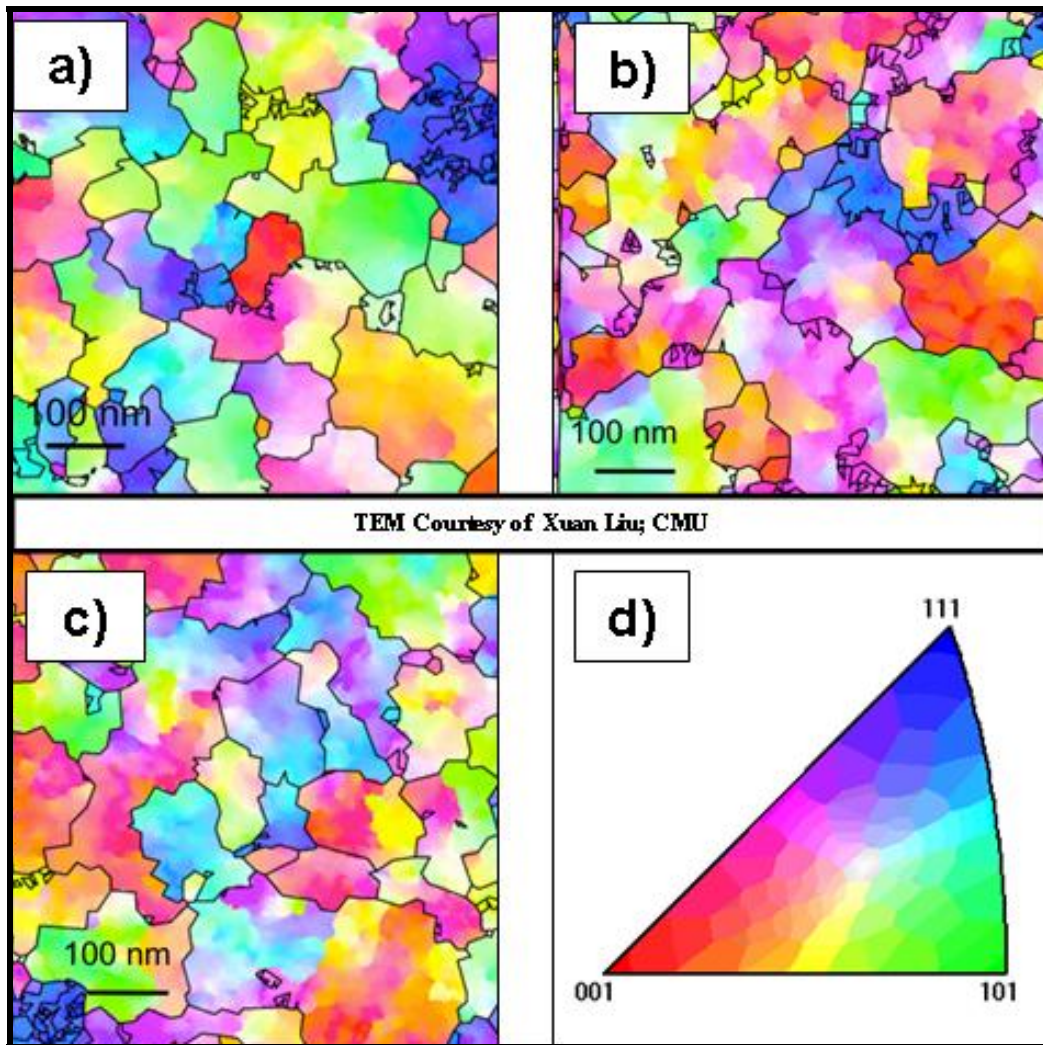


**Figure 35 ASTAR inverse pole figure maps of (a) GF-W2 (b) GF-W4 (c) GF-W5 Showing intra-rain misorientations. (d) Key.**

Grain boundaries are established by setting a 5° tolerance angle. The TEM investigation does not reveal dislocations. Instead, single grains are observed in which intra-granular distortion of the lattice are reported to exceed 50°. Such misorientation angles would be expected to result in geometrically necessary dislocations [Nye 1953], and will be considered in future work. Figure 36 shows a single grain from GF-W-05, where the relative orientation within the single grain was measured at 10 distinct points: Table 11 represents a matrix specifying the measured relative orientations.
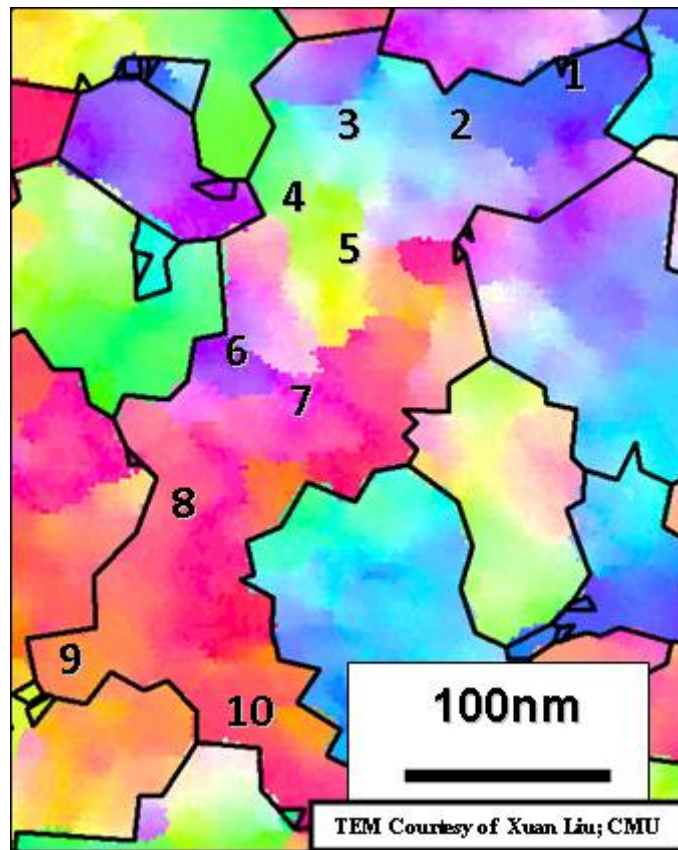


**Figure 36 ASTAR inverse pole figure maps of a single grain in sample GF-W-05. The numbers 1 - 10 indicate locations where relative orientations were measured and are tabulated in Table 11.**

**Table 11 Relative Misorientation angles**

|    | 1 | 2 | 3 | 4 | 5 | 6 | 7 | 8 | 9 | 10 |
|----|------|------|------|------|------|------|------|------|------|------|
| 1  |      | 16.3 | 13.9 | 25.2 | 32.1 | 43.2 | 50.5 | 46.4 | 41.3 | 38.8 |
| 2  | 16.3 |      | 2.4  | 9.3  | 16.6 | 41   | 35.3 | 31.6 | 27.1 | 26.8 |
| 3  | 13.9 | 2.4  |      | 11.4 | 18.7 | 43.3 | 37.4 | 33.6 | 29   | 28.3 |
| 4  | 25.2 | 9.3  | 11.4 |      | 9.8  | 31.9 | 27.8 | 24.7 | 21.7 | 24   |
| 5  | 32.1 | 16.6 | 18.7 | 9.8  |      | 27.6 | 18.7 | 15.2 | 11.9 | 15.5 |
| 6  | 43.2 | 41   | 43.3 | 31.9 | 27.6 |      | 20   | 23.2 | 28   | 36   |
| 7  | 50.5 | 35.3 | 37.4 | 27.8 | 18.7 | 20   |      | 4.7  | 10.9 | 18.4 |
| 8  | 46.4 | 31.6 | 33.6 | 24.7 | 15.2 | 23.2 | 4.7  |      | 6.3  | 14   |
| 9  | 41.3 | 27.1 | 29   | 21.7 | 11.9 | 28   | 10.9 | 6.3  |      | 8.1  |
| 10 | 38.8 | 26.8 | 28.3 | 24   | 15.5 | 36   | 18.4 | 14   | 8.1  |      |

Sub-grain distortions have been experimentally published in the past: These reports have focused on large grained (in excess of 100µm) bulk specimens and followed their inter- and intra-granular deformations as a function of loading conditions [Hofmann *et al.* 2009], [Korsunsky *et al.* 2012]. Intra-grain lattice distortions in polycrystalline thin films, on nanometric scales have not been previously reported.

The effect of these observed intra-grain distortions on the grain size measurable by line profile analysis is significant. Briefly considering the rocking of a specimen through the Bragg angle, is instructive [Warren 1990].
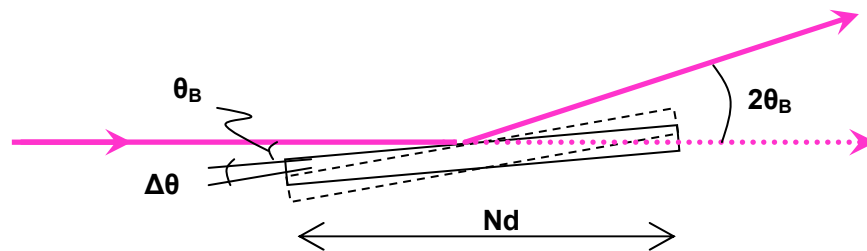


**Figure 37 Schematic of a rocking curve experiment.**

If a single-crystal specimen is rocked from low to high angles, and the detector remains fixed at the Bragg position; an increase in x-ray intensity will be observed as the

sample angle approaches 1/2 of the Bragg angle, $\theta_B$, and likewise decreases upon moving the specimen to higher angles. In the case where the specimen is smaller than the incident beam, The width of this "rocking curve" is influenced by the length of the crystal. Figure 37 presents a schematic of the situation, where N is the number of lattice planes, and d is the lattice spacing. The following equation can then be used to estimate the width of the rocking curve: Or rather, it can estimate the critical angular range, $\Delta\theta_C$, beyond which the Bragg condition is no longer satisfied:

$$\Delta\theta_C = \frac{\lambda}{2N a \sin\theta_B} \qquad\qquad \textbf{( 4-5 )}$$

The rocking curve concept may be applied to the intra-grain distortions discussed above. Let sub-grain lattice distortions be approximated by rigid, tilted planes. Consider a single crystallite of length D, and height (i.e. thickness) t, whose constituent lattice planes are each tilted with respect to one another about a common axis that is pointing out of the page (Figure 38). Attempts to measure D by x-ray methods will be unsuccessful because a portion of the planes are tilted beyond the critical angle, $\Delta\theta_C$. This break in coherency of the crystal from the perspective of the incident x-rays means that underestimated values of grain size will ultimately be measured. Specifically, N' planes with spacing d, will be seen as the coherent scatting domain.
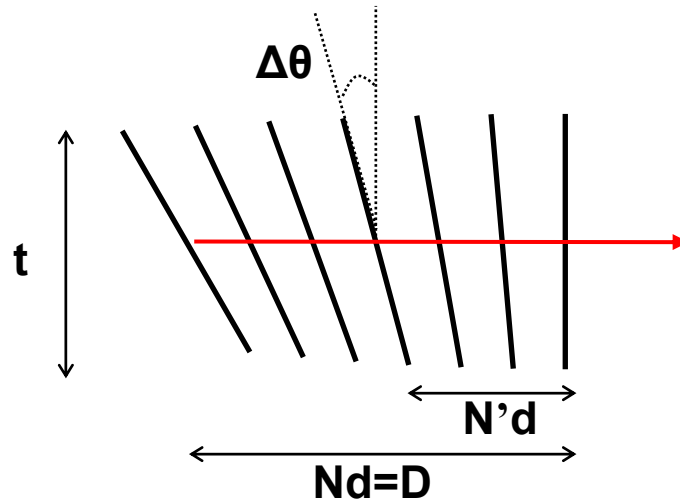
**Figure 38 Schematic of critical misorientation angle effect on grain size measured by x-ray diffraction**

In this approximation of a distorted crystal, the rocking curve equation may be applied. Using sample GF-W-05 as an example, t is film thickness (127Å), and Nd=D is the TEM grain size (1304Å). Using Cu-Ka radiation, and solving equation ( 4-5 ), $\Delta\theta_C$ is found to be approximately 1°. In this context, $\Delta\theta_C$ takes on the meaning of a critical intra-grain misorientation angle, beyond which the lattice planes no longer satisfy the Bragg condition with the incident beam. It is worth noting that rocking curve experiments on plastically deformed Cu single crystals have also reported that misorientations of only 1° are sufficient to terminate coherency [Wilkens *et al.* 1987]. Recall that intra-grain misorientations of up to 50° were observed in this specimen, which is far in excess of the calculated critical value. Additionally, recall that the measured Scherrer grain size for this sample was 168 Å, far short of the expected 1304Å. It may thus be concluded that the observed misorientations have a significant effect of the meaning and utility of x-ray based grain size analysis.

Coherency disruptions resulting from distortions within a crystal have been considered in terms of the effect on x-ray grain size analysis in plastically deformed metals [Ungár *et al.* 2012]. It was reported that dislocations in dipolar wall configurations result in x-ray phase shifts and peaks are therefore broadened by "sub-grains." While these reports are analogues to the present situation, and offer a conceptual framework for the present discussion, this prior work focused on specimens with grain on the order of 10μ and were representative of plastically deformed metals, rather than nanometic metallic thin films [Hughes *et al.* 1991].
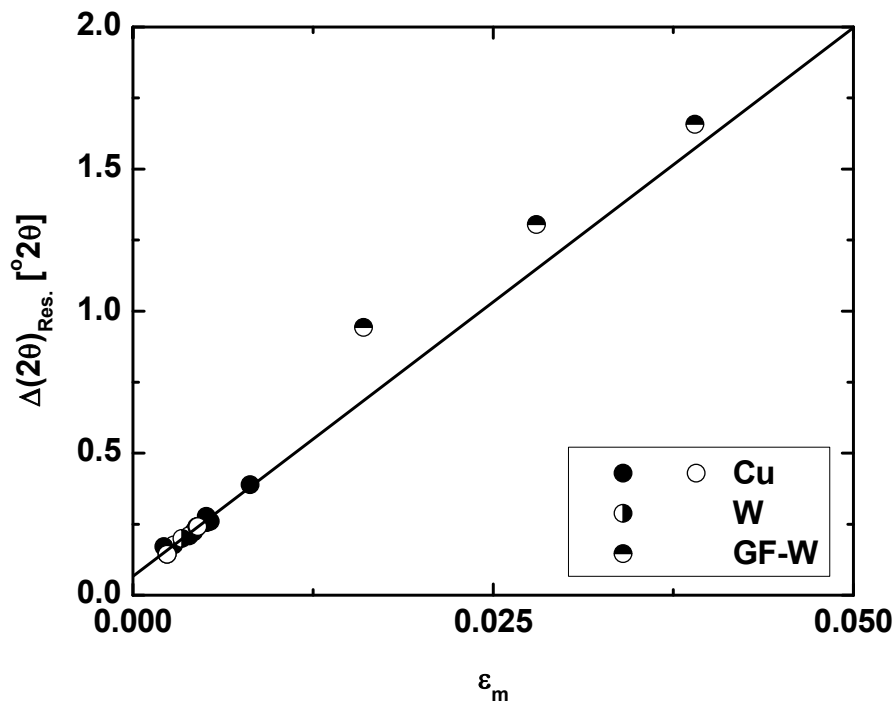


**Figure 39 Strong Correlation of Res. FWHM to the Mod. W-H slope; all samples**

The detailed TEM analysis of these GF-W samples may also be used revisit the concept of residual FWHM and its implications for grain size analysis. Figure 39 re-plots

the data from Figure 30 and its linear fit:  It additionally includes GF-W specimens for comparison.  The residual FWHM of the GF sample set not only strongly correlates to the slope of the modified Williamson-Hall, but closely follows the trend set by the Cu and W films discussed in previous sections.  This further indicates the influence of dislocations on the film and their effect on x-ray profiles.  It should be stressed that the strong correlation between residual FWHM and modified Williamson-Hall slope is comparable for all thin films explored; irrespective of crystallographic structure, atomic number, or diffractometer.

**4.5 Empirical Grain Size Calculation; A Novel Line Profile Method**

Because the residual width so closely follows the slope of the modified Williamson-Hall plot, it is possible to employ this empirical observation to formulate a novel line profile analysis strategy for measuring the grain size of thin films.  The slope of a line depicted in Figure 39 is equal to 38.627,  with an intercept of 0.0662 (equation ( 4-2 )).

The grain size contribution to peak broadening was thus calculated using (1) equation ( 4-2 ); (2) the instrument function (Figure 1);  and (3) the measured peak width, peak positions, and TEM grain sizes from Table 3.  Using the Scherrer equation and inserting the measured peak position and corresponding calculated FWHM, a calculated empirical grain size is obtained.  Table 12 lists grain sizes calculated by this method; a graphical comparison of TEM and empirical grain size values ($D_{Emp-\varepsilon}$) are presented in Figure 40.  The  solid line in Figure 40 indicates a hypothetical perfect correspondence between x-ray and TEM grain sizes.

**Table 12 Empirical grain size; calculated from $\varepsilon_M$**

| ID | $D_{TEM}$ [Å] | $D_{Emp-\varepsilon}$ [Å] |
|---|---|---|
| Cu-01 | 405 | 420 |
| Cu-02 | 684 | 633 |
| Cu-03 | 648 | 599 |
| Cu-04 | 877 | 846 |
| Cu-05 | 1011 | 852 |
| Cu-06 | 2215 | 2095 |
| Cu-07 | 2480 | 0 |
| W-01 | 1020 | 1000 |
| W-02 | 1060 | 1216 |
| W-03 | 1010 | 1231 |
| W-04 | 1110 | 1107 |
| W-05 | 1090 | 1260 |
| W-06 | 1160 | 1109 |
| GF W 2 | 830 | 185 |
| GF W 4 | 820 | 216 |
| GF W 5 | 810 | 188 |
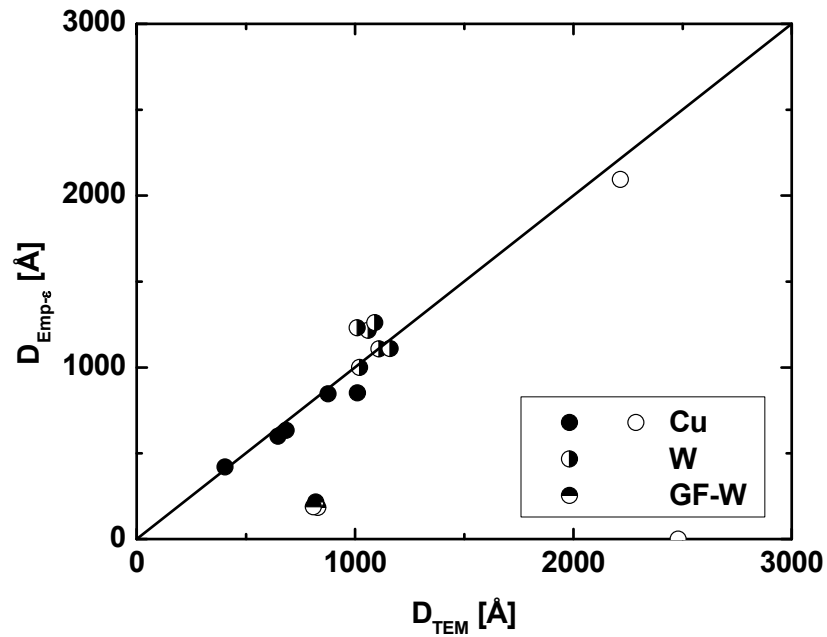


**Figure 40 Empirical grain size; calculated from $\varepsilon_M$**

Using this novel empirical method of line profile analysis, a strong correlation between TEM and x-ray measures of grain size is obtained. The sum squared error for

this method is calculated to be $8.4 \times 10^6$. This value is comparable to that obtained by the Modified Williamson-Hall method, when its error is calculated for all samples including the GF specimens ($3.7 \times 10^6$). It should be noted that a single Cu specimen, Cu-07, fails to be measurable by this method. This is attributed to The fact that the measured FWHM is essentially equal to the calculated residual FWHM, likely indicating that the narrow peak is almost entirely broadened by defects. Accordingly, a grain size value of 0 has been assigned in Table 12, Figure 40, and used for error calculations.

Similarly, the GF-W samples have large grain sizes, and high dislocation densities, in comparison to the instrumental resolution. Nevertheless, the strong correlation between microstrain and the residual width motivates further development of dislocation-based empirical strategy for grain size analysis by line profile methods. **Error! Reference source not found.** is presented as a summary of the line profile methods explored. It lists the total sum squared error between TEM and x-ray-based analyses of grain size.

**Table 13 Comparison errors for all Line Profile Methods**

| Line Profile Method | $\Sigma\chi^2$ |
|---|---|
| Scherrer (k=1.00) | 5.5.E+06 |
| Scherrer (k=1.055) | 2.6.E+06 |
| Williamson-Hall | 1.4.E+09 |
| Modified Williamson-Hall | 3.7.E+06 |
| Empirical ($\varepsilon_M$) | 8.4.E+06 |

Because the slope of the modified Williamson-Hall plot is understood to correspond to dislocation density, a graph similar to Figure 39 may be generated in which the residual width is plotted as a function of dislocation density directly. Figure 41 presented such a graph, which also includes a logarithmic fit to all data.
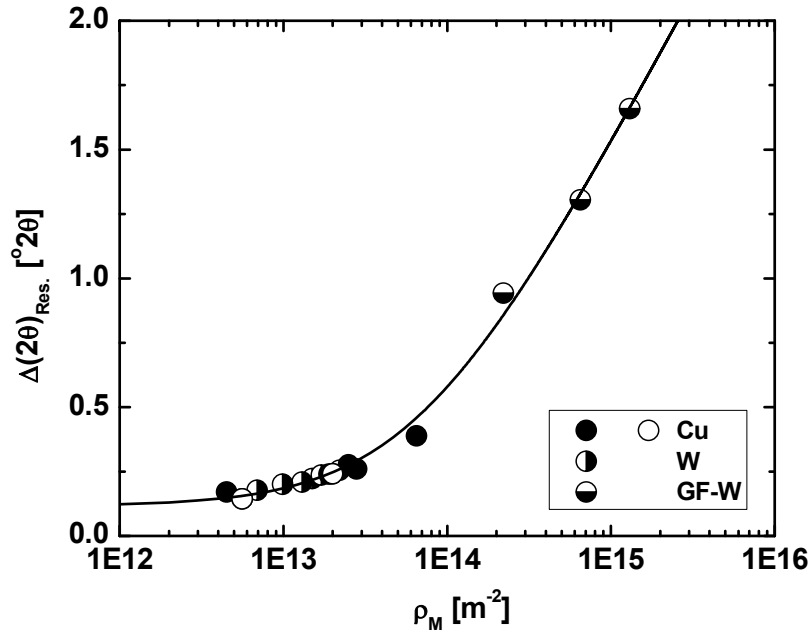


**Figure 41 Residual FWHM and Dislocation Density**

The equation of the fitted line in Figure 41 is displayed as equation ( 4-6 ).

$$\Delta(2\theta)_{Res.} = -16.38201 + -0.51773 Ln(\rho_M + 6.90075 \times 10^{13})$$

( 4-6 )

The fit is strongly indicative of a significant contribution to peak broadening stemming from dislocations. This work may be supplemented by considering dislocation density analysis by non-x-ray methods: Specifically TEM based analysis.

Preliminary investigations have been carried out into the correlation between dislocation density analysis based on TEM and X-ray diffraction. The TEM analysis were performed by Xuan Liu of CMU, and are based on a the Read-Shockley model of dislocations [Read *et al.* 1950]. More sophisticated analysis will be perused, which will be based on the Nye model of Geometrically Necessary Dislocations [Nye 1953].

Figure 42 presents a summery of the preliminary comparison between TEM and x-ray measures of dislocation density. Specifically, all GF-W samples are plotted along with sample W-03. While the values obtained by the Read-Shockley method are higher than that obtained by the modified Williamson-Hall method, a correlation is nevertheless evident. In terms of further developments warranting consideration for x-ray based analysis, the exact value of the constant $A_\rho$ in equation ( 1-14 ) may be investigated. Specifically, the constant $A_\rho$ in equation ( 1-14 ) was assumed to equal 10 for all samples. As stated in section 1.1.2.3 Williamson-Hall plotthis constant may vary by almost an order of magnitude: This translates to almost an order of magnitude uncertainty in the dislocation density itself. Continued efforts in are therefore motivated.
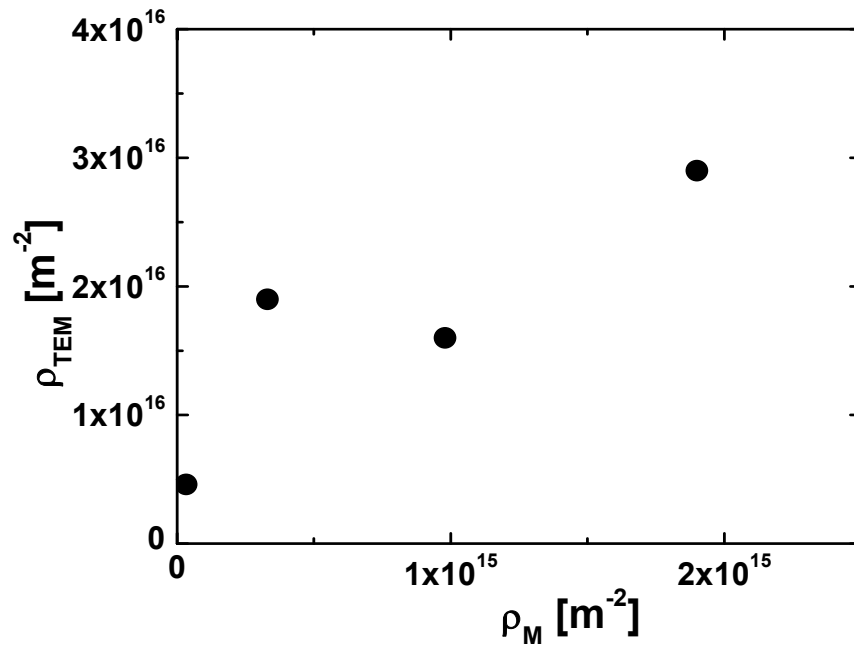
**Figure 42 Comparison of TEM and XRD dislocation density calculations**

## 4.6 Conclusion

It is proposed that misfit-like strains at the film/substrate interface result in dislocations whose cores spread, resulting in a distorted crystal lattice which affects x-ray diffraction in that the coherent scattering domain size is limited by these intra-granular distortions. The effect on peak broadening is two fold: (1) Lattice distortions result in an effective orientation contrast, wherein intra-grain lattice misorientations exceeds a critical value, $\Delta\theta c$, beyond which the Bragg condition is no longer satisfied. This ultimately results in the poor approximations of grain size as measured by line profile techniques, because coherency boundaries are not coincident with grain boundaries alone. (2) The induced lattice distortions vary the lattice spacing in a manner that requires use of the dislocation contrast factor to accommodate effects of strain anisotropy in the Williamson-

93

Hall plot. The speading of dislocation cores across the film/substrate interface would render them invisible to TEM investigations. Precession Electron Diffraction Orientation Maps in TEM studies of W films however, reveal intra-granular distortions whose misorientaion angles approach 50° across a grains whose diameters are approximately 1000Å. Calculations suggest a dislocation core width on the order of a few hundred Angstroms, independent of films thickness, or grain size. The poor correlation between TEM and x-ray measures of grain size may also be explained: When the (TEM) grain size is smaller than the dislocation core width, grain boundaries are the dominant mechanism by which coherency is disrupted. As the grains size increases and multiple dislocations are present within grains, coherency across the length of the crystallite is disrupted. Because x-rays "see" coherent domains, accurate measures of grain size are limited to specimens where the coherent scattering domains are established predominately by grain boundaries. In the case of thin films with very large grains, grain boundaries only represent a fraction of these coherency boundaries.

Finally, the effect of dislocations to broaden diffraction peaks, and hence limit grin size analysis, may be taken advantage of. A novel residual peak width parameters has been developed to provide insight into the broadening effects of dislocations. The strong correlation between residual peak width and the slope of the modified Williamson-Hall plot was used to developed an empirical method for determining grain size. This empirical method was additionally extended to consider the dislocation density directly. A significant decrease in the sum squared errors between TEM and x-ray based grain sizes values obtained by these empirical methods are encouraging and warrant further development.

# CHAPTER FIVE : INTERFACE MORPHOLGY ANALYSIS

The morphological evolution of chemically stable metal/air or metal/vacuum interfaces (free surfaces) with annealing temperature and/or time have been explored in the past [Nichols *et al.* 1965], [Balluffi *et al.* 2005], [Jiran *et al.* 1990]. Relatively little work has been done however, to extend that understanding to chemically stable buried interfaces. The tendency for systems to reduce their free energy by minimizing surface area, i.e., capillarity, should have an important role in the evolution of buried interfaces as it does for free surfaces. However, for buried interfaces two solids are present and their morphology is mechanically coupled. The role of mechanical coupling to modify the evolution of buried interfaces is of significant interest to many nano-scaled system and to semiconductor interconnections in particular.

## 5.1 Objectives

The objective of this research is to understand the morphological evolution of nanometric Cu film surfaces and interfaces, and to develop a fundamental understanding of the role that annealing plays on the evolution of solid/solid interfaces

## 5.2 Results

### 5.2.1 Qualitative Observations

X-ray scattering techniques reveal significant differences in the interfacial evolution of Cu thin films encapsulated by $SiO_2$ as compared to those encapsulated by Ta/$SiO_2$. Qualitative conclusions regarding RMS roughness can be drawn by simple inspection of the specular patterns. Annealing $SiO_2$ encapsulated films at 600°C results

in a smoother Cu/SiO$_2$ interface, as can be seen from the slower decay of specular intensity as compared to its 150°C counterpart (Figure 43(a)). Ta/SiO$_2$ encapsulated films change little upon annealing (Figure 43(c)).

The specular intensity profiles were modeled (solid lines) to allow for quantitative values of thickness, $\sigma_{upper}$ and $\sigma_{lower}$ for the Cu layers to be determined (Table 14). Figure 43(b and d) shows experimentally obtained rocking-curves (circles) and calculated spectra (solid lines). These diffuse X-ray reflectivity scans were modeled to determine the lateral correlation length of roughness, the vertical correlation fraction and the fractal exponent. The specular reflection in the diffuse spectra at $Q_x$=0 is broadened by instrument resolution and contains no quantitative information regarding the sample and was therefore excluded from the analysis. Qualitative trends can be observed by inspection of the diffuse patterns. For SiO$_2$ encapsulated Cu film, the diffusely scattered intensity for the sample annealed at 600°C (open circles) decays more quickly than at 150° (filled circles). Simply put, at 150°C the spectrum is essentially flat, and is concave at 600°C. Given that the intensity of scattered X-rays is proportional to the square of the interface roughness amplitude, inspection of the diffusely scatter intensity distribution for SiO$_2$ encapsulated films suggests a decay in roughness amplitude that depends on the lateral length scale of the roughness.
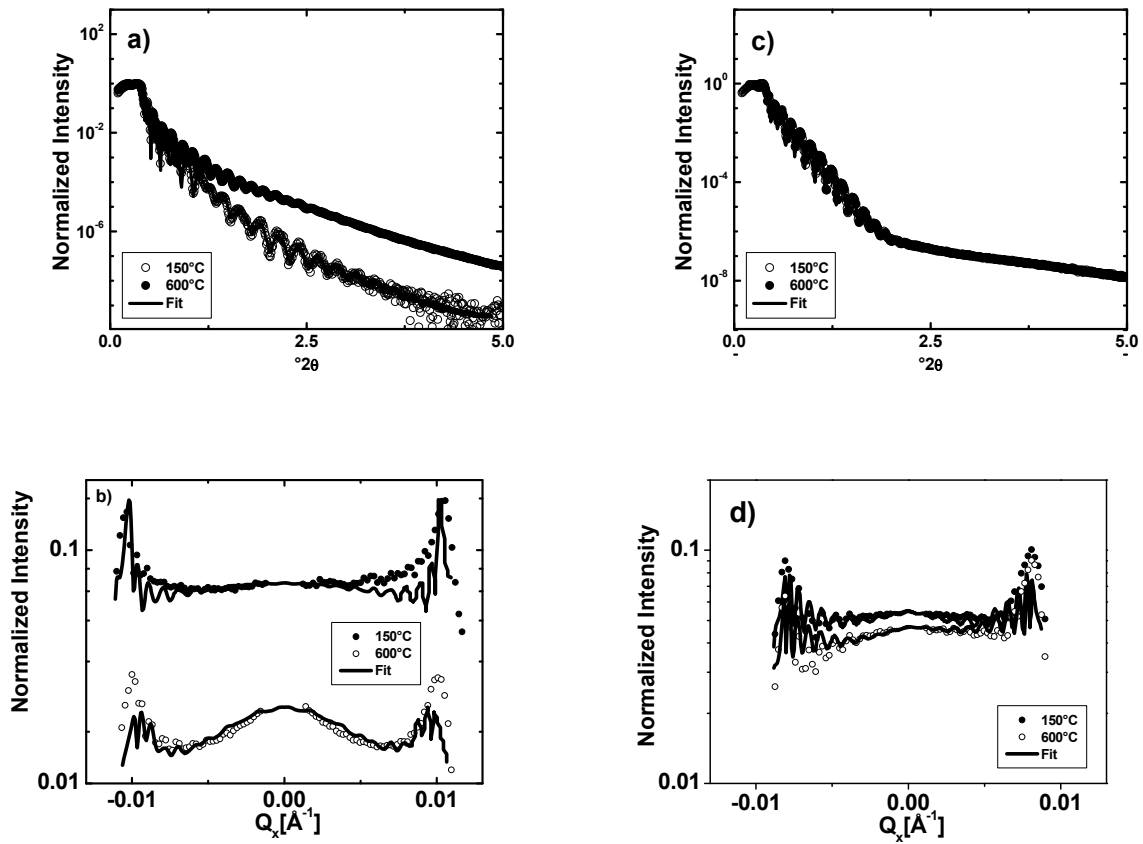
**Figure 43 X-ray reflectivity spectra(a,b) $SiO_2/Cu/SiO_2$ (c,d) $SiO_2/Ta/Cu/Ta/SiO_2$**

Before discussing quantitative results and their interpretations, the following conclusion should be kept in mind which can be drawn by simple inspection of the specular and diffuse X-ray reflectivity spectra: Annealing at 600°C results in a roughness-wavelength dependent decrease in roughness amplitude for $Cu/SiO_2$ interfaces. These observations are consistent with that predicted by capillarity driven surface diffusion and smoothening [Nichols *et al.* 1965]. The apparent lack of interface morphology evolution in the Cu/Ta interface is also noted.

To confirm, quantify, and interpret these observations, specular and diffuse x-ray reflectivity patterns were modeled using commercially available software: Results of

modeling can be found in Table 14. Error bars for reflectivity results are quoted at a 90% confidence level. Grain size values are provided for reference; a single asterisk (*) denotes grain sizes calculated from resistivity data [Sun 2009], a double asterisk (**) indicates samples characterized by GID in chapter 4.

**Table 14  Results of fitting X-ray reflectivity spectra.  Grain sizes based on TEM.**

a) $SiO_2$ / Cu / $SiO_2$; 150°C

| Thickness [Å] | Grain Size [Å] | $\sigma_{upper}$ [Å] | $\sigma_{lowerr}$ [Å] | $\xi_{lateral}$ [Å] | $\alpha$ | $\xi_{vertical}$ |
|---|---|---|---|---|---|---|
| 270±2 | **405±25 | 12±1 | 8±1 | 381±46 | 0.8±0.2 | 0.4±0.4 |
| 312±1 | *409±24 | 10±1 | 7±1 | 203±18 | 0.9±0.2 | 0.5±0.5 |
| 353±3 | 543±21 | 11±1 | 10±1 | 319±40 | 0.9±0.2 | 0.7±0.1 |
| 451±2 | **1011±46 | 10±1 | 8±1 | 287±33 | 0.9±0.2 | 0.4±0.1 |
| 718±2 | 1718±79 | 7±1 | 12±2 | 492±57 | 0.9±0.2 | 0.6±0.2 |
| 1439±3 | **2481±172 | 7±1 | 26±1 | 616±113 | 0.9±0.2 | 0.5±0.3 |

b) $SiO_2$/ Cu / $SiO_2$; 600°C

| Thickness [Å] | Grain Size [Å] | $\sigma_{upper}$ [Å] | $\sigma_{lowerr}$ [Å] | $\xi_{lateral}$ [Å] | $\alpha$ | $\xi_{vertical}$ |
|---|---|---|---|---|---|---|
| 292±1 | *305±15 | 3±1 | 8±1 | 318±90 | 0.6±0.2 | 0.6±0.1 |
| 336±5 | **684±44 | 2±2 | 7±1 | 412±56 | 0.9±0.1 | 0.5±0.5 |
| 369±3 | 814±45 | 5±1 | 10±2 | 420±112 | 0.9±0.2 | 0.9±0.1 |
| 464±1 | 1126±77 | 4±1 | 9±1 | 561±65 | 0.9±0.2 | 0.6±0.2 |
| 745±1 | 2200±95 | 3±1 | 10±1 | 706±62 | 0.5±0.2 | 0.5±0.3 |
| 1499±1 | 4252±157 | 3±1 | 10±1 | 798±62 | 0.8±0.2 | 0.1±0.1 |

c) $SiO_2$/ Ta / Cu / Ta / $SiO_2$; 150°C

| Thickness [Å] | Grain Size [Å] | $\sigma_{upper}$ [Å] | $\sigma_{lowerr}$ [Å] | $\xi_{lateral}$ [Å] | $\alpha$ | $\xi_{vertical}$ |
|---|---|---|---|---|---|---|
| 281±7 | *681±34 | 8±1 | 15±3 | 316±46 | 0.4±0.2 | 0.2±0.2 |
| 335±1 | *376±19 | 2±1 | 6±1 | 401±41 | 0.4±0.2 | 0.5±0.1 |
| 370±9 | *814±45 | 15±5 | 10±2 | 606±57 | 0.4±0.2 | 0.5±0.5 |
| 482±4 | *1126±77 | 11±1 | 10±1 | 326±38 | 0.7±0.2 | 0.3±0.1 |
| 762±2 | *2200±95 | 15±1 | 16±5 | 687±78 | 0.4±0.2 | 0.3±0.1 |
| 1541±5 | *4659±172 | 22±1 | 22±3 | 864±77 | 0.6±0.2 | 0.5±0.5 |

d) $SiO_2$ / Ta / Cu / Ta $SiO_2$; 600°C

| Thickness [Å] | Grain Size [Å] | $\sigma_{upper}$ [Å] | $\sigma_{lowerr}$ [Å] | $\xi_{lateral}$ [Å] | $\alpha$ | $\xi_{vertical}$ |
|---|---|---|---|---|---|---|
| 283±2 | 346±17 | 8±1 | 11±1 | 412±56 | 0.9±0.2 | 0.5±0.5 |
| 342±4 | 394±17 | 11±1 | 12±2 | 489±53 | 0.8±0.2 | 0.5±0.5 |
| 387±5 | 443±22 | 15±4 | 10±1 | 612±58 | 0.5±0.2 | 0.6±0.4 |
| 484±3 | 696±34 | 10±1 | 10±1 | 599±125 | 0.9±0.2 | 0.5±0.2 |
| 779±0 | 1101±46 | 14±2 | 12±3 | 773±94 | 0.5±0.2 | 0.5±0.5 |
| 1552±3 | 3451±150 | 9±1 | 15±2 | 891±79 | 0.9±0.2 | 0.5±0.2 |

In  Table 15 each entry represents an average of six sister samples (i.e. a total of 24 samples are represented) whose thicknesses were intentionally varied from 27Å  to 1580Å.  Error bars correspond to the average error from each set of six sister samples.

**Table 15 Average roughness values for $SiO_2$ and $Ta/SiO_2$ encapsulated Cu films.**

|  | $SiO_2$ / Cu / $SiO_2$ 150°C | $SiO_2$ / Cu / $SiO_2$ 600°C | Ta / Cu / Ta 150°C | Ta / Cu / Ta 600°C |
|---|---|---|---|---|
| $\sigma_{upper}$ [Å] | 10 ± 1 | 3 ± 1 | 14 ± 2 | 11 ± 2 |
| $\sigma_{lowerr}$ [Å] | 12 ± 1 | 9 ± 1 | 14 ± 2 | 12 ± 2 |
| $\Xi$ [Å] | 383 ± 38 | 533 ± 53 | 523 ± 5 | 588 ± 6 |
| $\xi_V$ | 0.50 ± 0.10 | 0.4 0 ± 0.10 | 0.10 ± 0.10 | 0.20 ± 0.10 |
| $\alpha$ | 0.9 ± 0.1 | 0.7 ± 0.3 | 0.5 ± 0.2 | 0.7 ± 0.2 |

## 5.2.2 Statistical Characterization of Film Growth

Having obtained numeric solutions of the correlation function, studying the effective growth dynamics within the thickness rage from 280Å to 1580Å is possible. Although the relatively small data set limits any conclusion to being semi quantitative, the consequence of barrier layer and annealing temperature on the effective growth dynamics can nonetheless be observed.

Given equation ( 1-16 ), $\xi(t) \sim t^{1/z}$, the determination of the dynamic exponent $z$ is achieved by fitting a power law to experimentally obtained values of $\xi(t)$. Note that the time for growth, $t$, corresponds to the deposition time for the thin film. If a constant deposition rate is assumed, film thickness is directly proportional to deposition time. Plotting $\xi$ as a function of thickness (which has been normalized to the thickest film) can accordingly be used to determine $z$. Accordingly, the correlation length as a function of normalized deposition time has been plotted in Figure 44(a) for $Cu/SiO_2$, and Figure 44(b) for Cu/Ta. Normalizing each data set (Figure 44(c)) highlights the fact that a single dynamic exponent value can be used to fit each data set, irrespective of barrier layer and annealing conditions. Here $\xi_0$ represents the proportionality constant that

makes the relation, $\xi(t) \sim t^{1/z}$, an equality, which then corresponds to the lateral
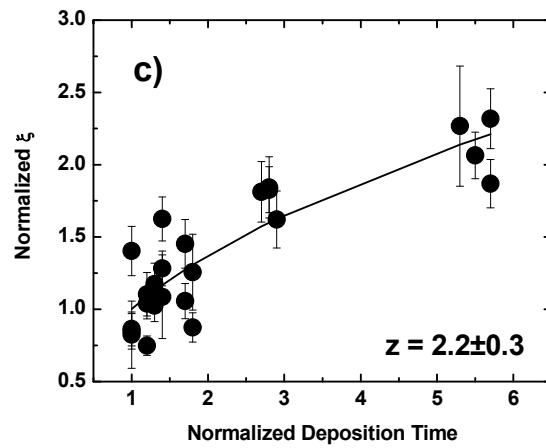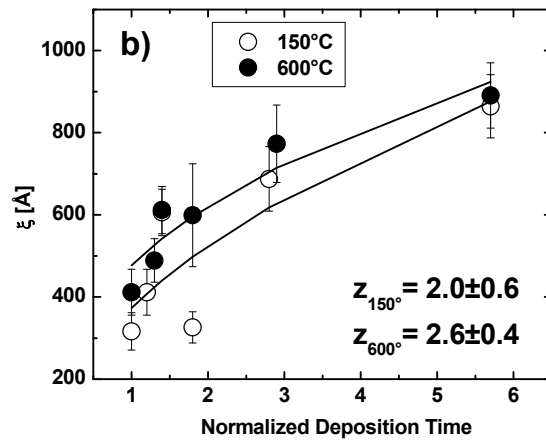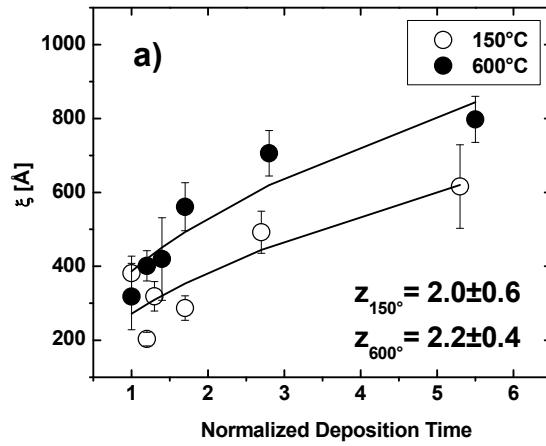
correlation length at time $t_0$.

**Figure 44 Power law scaling of correlation length; self affine behavior**

For determining the growth exponent $\beta$, a similar analysis can be carried out given the scaling law presented in equation ( 1-17 ): $\sigma(t) \sim t^{\beta}$. The data in Table 14 however shows the RMS roughness of both upper and lower interfaces to be independent of film thickness. Strictly speaking, the poor power-law dependence of $\sigma$ on thickness indicates that the Cu/barrier interfaces do not scale dynamically. Similar deviations from dynamic scaling in thin films have been reported in the past, especially given the thickness range being investigated[Schlatmann *et al.* 1996], [Lita *et al.* 2000]. Nevertheless, the continued assumption will be made that the Cu/barrier interfaces are self-affine and scale dynamically: The relation $\beta = \dfrac{\alpha}{z}$ will accordingly be used for determining $\beta$. Here $\alpha$ represents those average values from table 2. All three dynamic scaling exponents were thus determined and are listed in Table 16.

**Table 16  Dynamic growth exponents**

| Barrier | T | α | ß | z |
|---|---|---|---|---|
| SiO2 | 150°C | 0.9±0.2 | 0.4±0.2 | 2.0±0.5 |
| SiO2 | 600°C | 0.5±0.2 | 0.3±0.2 | 2.0±0.6 |
| Ta/SiO2 | 150°C | 0.7±0.2 | 0.3±0.2 | 2.2±0.4 |
| Ta/SiO2 | 600°C | 0.7±0.2 | 0.3±0.2 | 2.2±0.4 |
| Combined | | 0.7±0.2 | 0.3±0.2 | 2.2±0.5 |

The exponents are found to be independent of barrier layer and annealing conditions. This suggests that these films belong to a single universality class; even after experiencing two growth stages (during deposition, and during subsequent annealing) and capillarity driven surface diffusion activated by post-processing annealing. The averaged values for growth exponents are, within calculated error, comparable to those values predicted by the KPZ equation ( 1-22 ). The results are further summarized in Figure 45, where Fourier methods were used to reconstruct a self-affine surface growing in

accordance with dynamic scaling laws whose exponents are equal to those of the combined values from Table 16. Specifically, Figure 45 illustrates five distinct time-slices of a growing rough surface for which the amplitude of roughness and lateral correlation length increase in accordance with the combined values from Table 16.
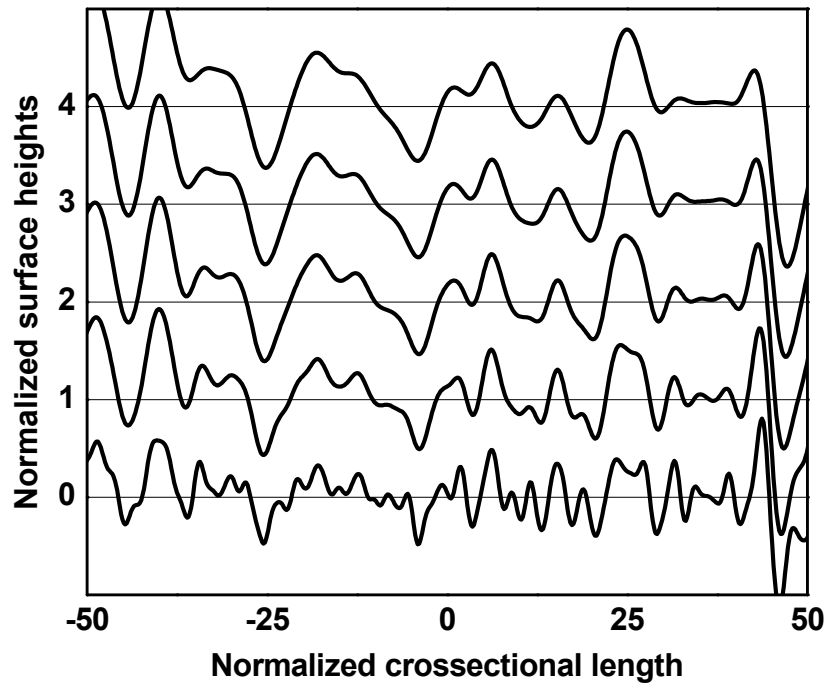


**Figure 45  Surface growth reconstruction based on exponents from table 3**

Additional investigation of the scaling of thin films may be pursued by considering grain size. In following the convention of Figure 44, Figure 46 presents the correlation length plotted as a function of grain size which has been normalized such that the larges measured grain size is equal to 1. While investigating grain growth dynamics is beyond the scope of this work, it is nonetheless worthwhile to look for trends.

**Figure 46 Power law scaling of correlation length with grain size**

Fitting the grain size data with a power law yields exponent values that are equivalent to those obtained for film thickness. This result is consistent with an incomplete decoupling of film thickness from grain size [Sun *et al.* 2009]. Normalizing each data set (Figure 46(c)), highlights the fact that a single dynamic exponent value can be used to fit each data set, and is equivalent, within statistical error, to that obtained in Figure 44(c). Although these results are not used to identify a universali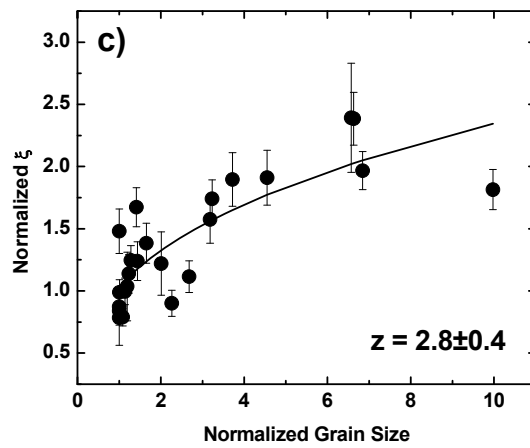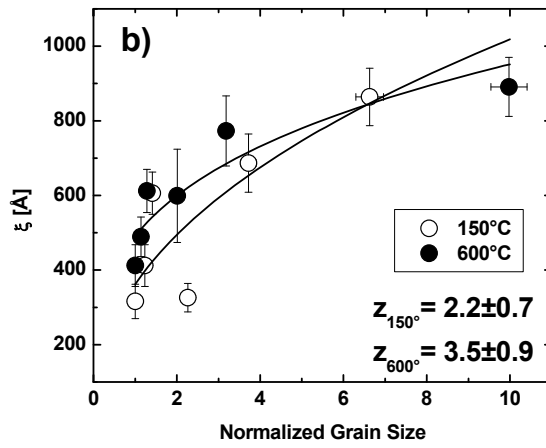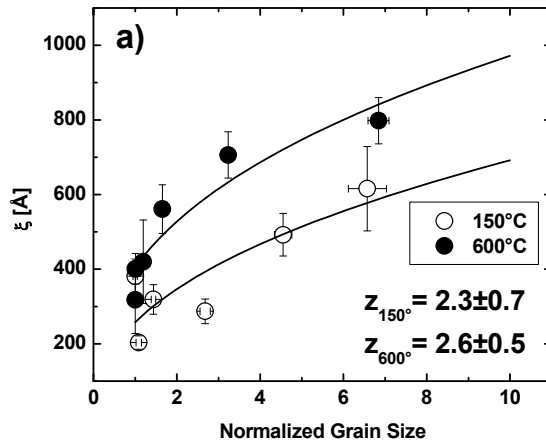ty class for grain growth, they do suggest a fundamental scaling relationship between grain size, film thickness, and lateral roughness[Lita *et al.* 2000].

## 5.2.3 Interface Smoothening

When comparing results from modeling specular reflectivity profiles, the most noteworthy trend is that of RMS roughness and annealing. Figure 6 presents average RMS roughness values from table 2 plotted as a function of anneal temperature. For $SiO_2$ encapsulated films, significant changes upon annealing at 600°C are observed (Figure 47(a)). Firstly, $\sigma_{upper}$ is observed to decrease significantly in comparison to $\sigma_{lower}$. This is attributed to the fact that the bottom $Cu/SiO_2$ interface, although chemically identical to the top, is attached to a rigid substrate which mechanically hinders changes in interfacial topography. For $Ta/SiO_2$ encapsulated films, $\sigma_{upper}$ and $\sigma_{lower}$ are not only comparable to one another, but also fail to evolve significantly upon annealing (Figure 47(b)).
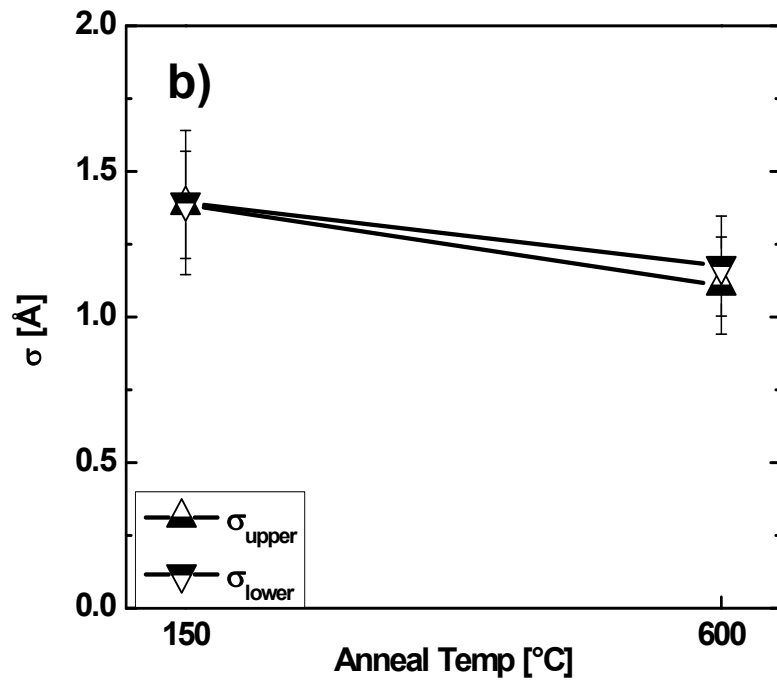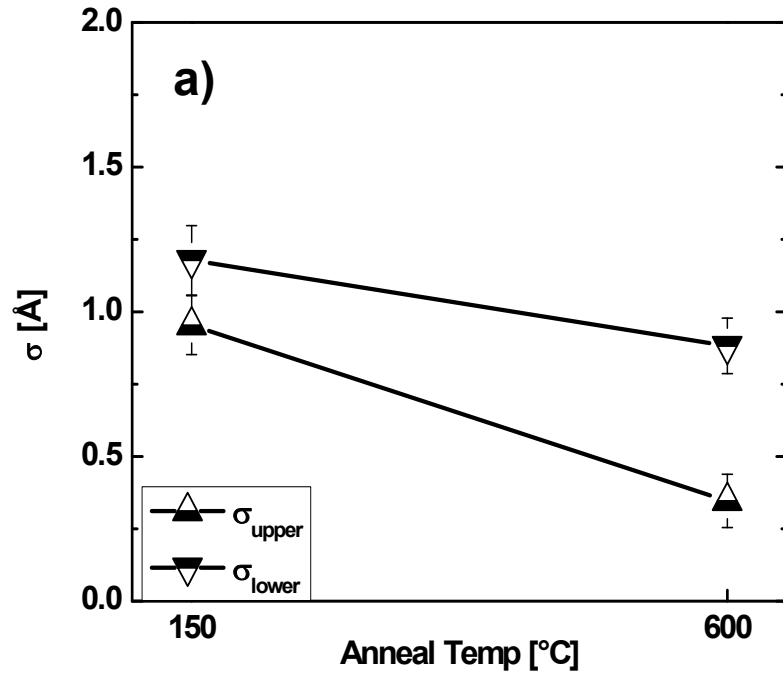
**Figure 47 Average RMS roughness (a) SiO$_2$ and (b) Ta/SiO$_2$ encapsulated Cu films**

106

These observations for the upper $Cu/SiO_2$ interfaces point toward capillarity as a driving force for surface smoothening; an increase in lateral correlation length is therefore expected to correspond to the decrease in roughness amplitude upon annealing.

Figure 48(a) depicts such an increase in correlation length corresponding to a decrease in RMS roughness with annealing for the upper $Cu/SiO_2$ interface, thus motivating a more detailed investigation of the Mullins theory of surface smoothing. No smoothing trend is apparent for Cu/Ta interfaces Figure 48 (b).
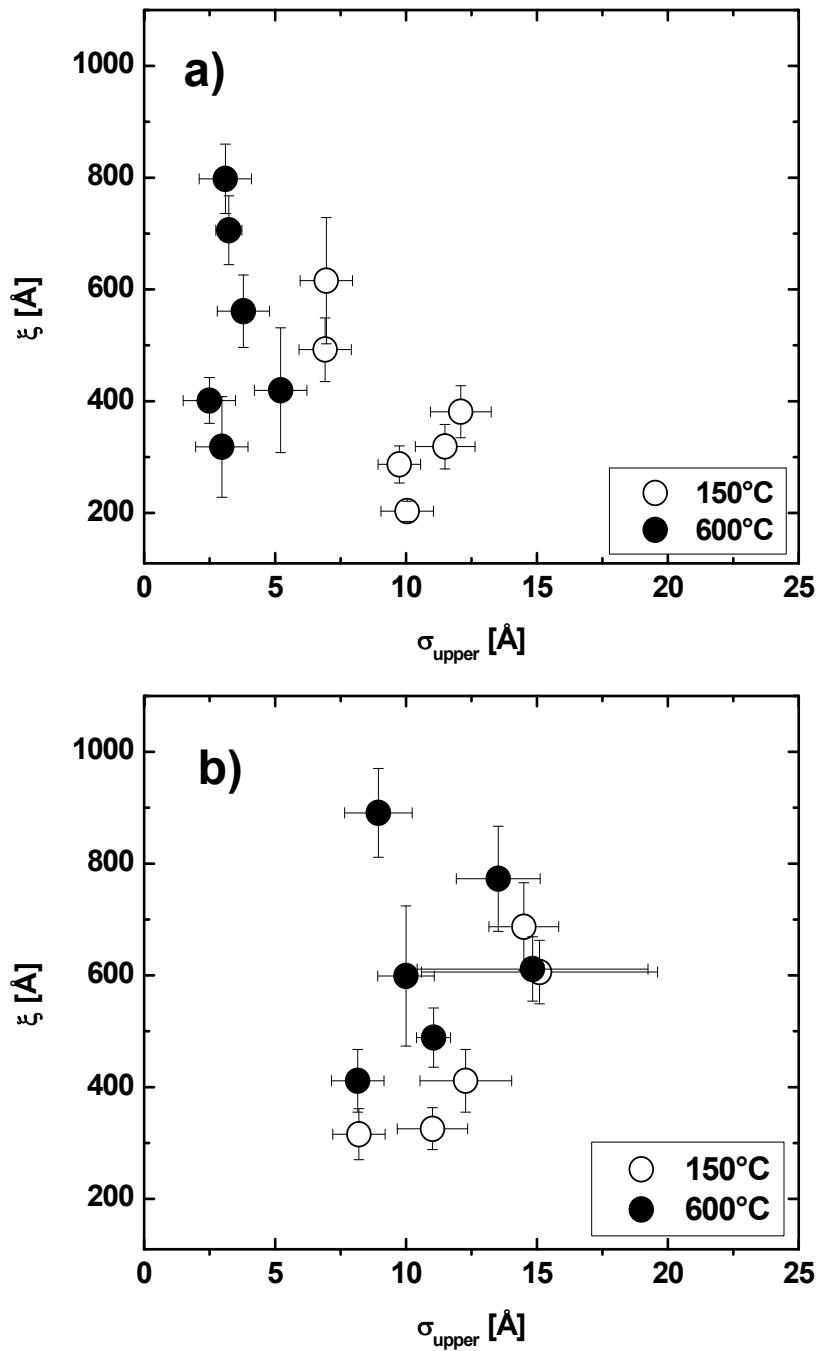
**Figure 48 Correlation length and. roughness of (a) Cu/SiO$_2$ and (b) Cu/Ta/SiO$_2$**

Figure 49 presents simplified illustrations to supplement and highlight the observed effects of annealing. A single sinusoidal wavelength, $\lambda$, is used to represent

the more complex topography of the interface summarized by the lateral correlation length, $\xi$. In summary: Upon annealing, $\sigma_{upper}$ of the Cu/SiO$_2$ interface decreases while $\sigma_{lower}$ remains unchanged. The wavelength $\lambda$ increase observed upon annealing is presumed to be that of the upper interface. However, while the RMS changes are distinguishable for the upper and lower interfaces, the same is not true for the changes in lateral correlation length, which is not experimentally distinguished between upper and lower interfaces. The Cu/Ta interfaces are consistent between top and bottom, and do not change upon annealing.
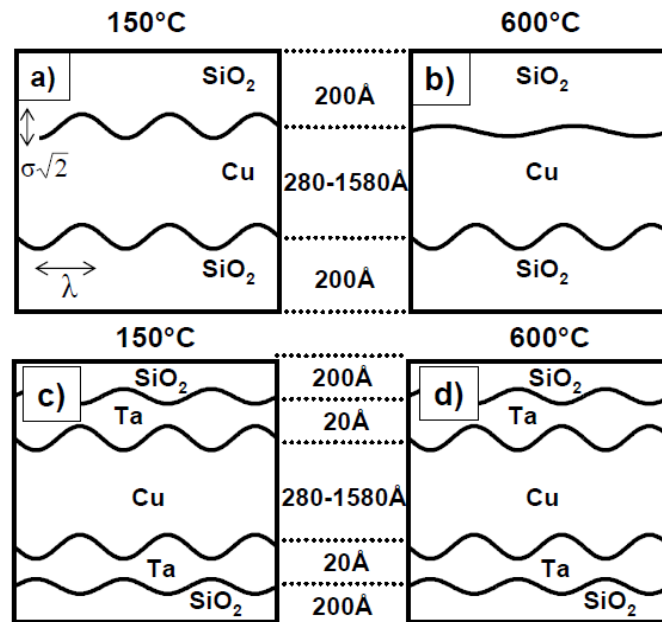


**Figure 49  Illustration of film interfaces displaying capillarity effects**

The results are quantitatively summarized in Figure 50, wherein Fourier methods were used to reconstruct the upper Cu/SiO$_2$ self-affine interface decaying in accordance with the results from Table 16. Specifically, the correlation length is shown to increase by 28%, while the RMS roughness is shown to decrease linearly by 70%.
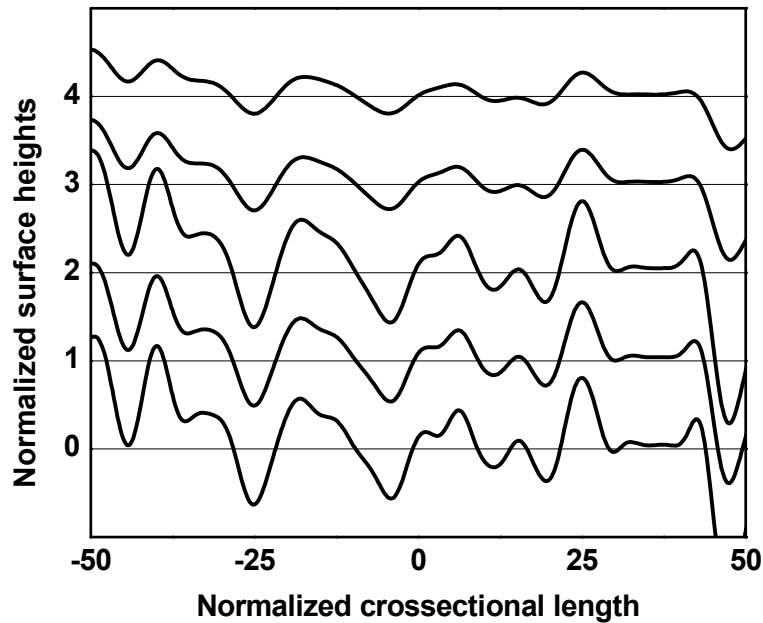
**Figure 50 Reconstruction the Cu/SiO$_2$ interface, decay according to Table 16.**

We now focus the discussion on the wavelength term in the exponent of equation ( 1-24 ) in the context of the upper Cu/SiO$_2$ interface which undergoes significant morphology evolution due to the higher temperature anneal. Because the decay of the amplitude exponent is proportional to the inverse of wavelength to the fourth power, short wavelength roughness is expected to smoothen much more quickly than long wavelength roughness, leading to an increase in the in-plane correlation length of the roughness as the amplitude of the roughness decreases.

The present results are in qualitative agreement with equation ( 1-24 ), in that a notable increase in the correlation length is observed. Furthermore, quantitative analysis of the diffusely scattered intensity over values of Q$_x$ for which the kinematical scattering approximation is valid, (0.001Å$^{-1}$ to 0.005Å$^{-1}$) shows a greater reduction in intensity at shorter wavelengths. However, the present data is found not to be consistent with the

110

expected $\lambda^{-4}$ dependence, as shown Figure 51(a), in which the dashed line represents roughness decay according to classical capillarity (i.e., equation ( 1-24 )). Instead, the data are reported to fit a much weaker wavelength dependence, decaying as $\lambda^{-\frac{1}{2}}$ for the evolution of this buried interface Figure 51(a), (solid line). The circles marked as data in Figure 51(a) corresponding to nominally 300Å (black), 500Å (grey) and 800Å (white) thick specimens.

Non-classical theories of smoothening of rough surfaces have been developed in the past. Comparison of the samples with nominally 300Å thick Cu films are additionally compared to non-classical models in Figure 51(b), for which the y-axis has been rescaled for clarity. One such approach [Erlebacher *et al.* 2000] treats a free surface whose height profile was intentionally modulated in a sinusoidal fashion. Although the surface statistics of such a system differ from encapsulated, self-affine thin films, the approach shows merit and should be investigated further Figure 51(b), (short-dashed line).
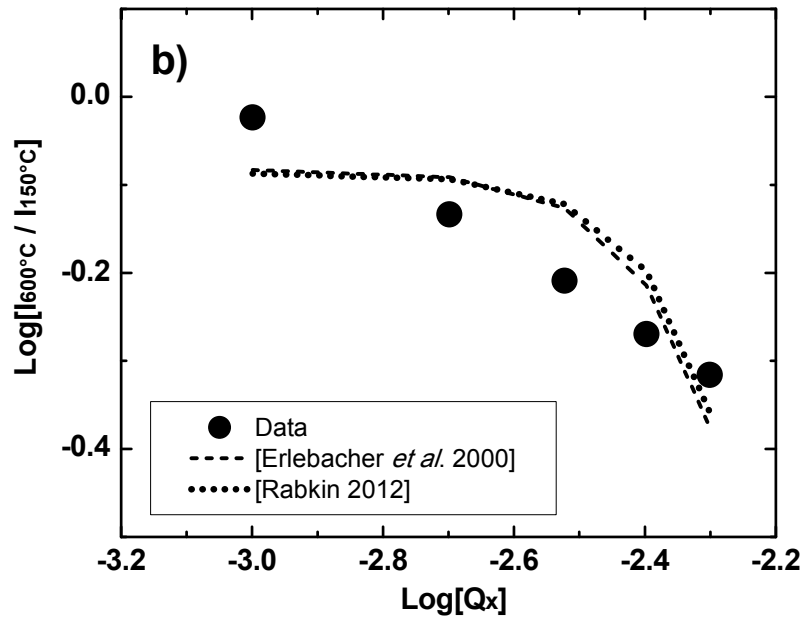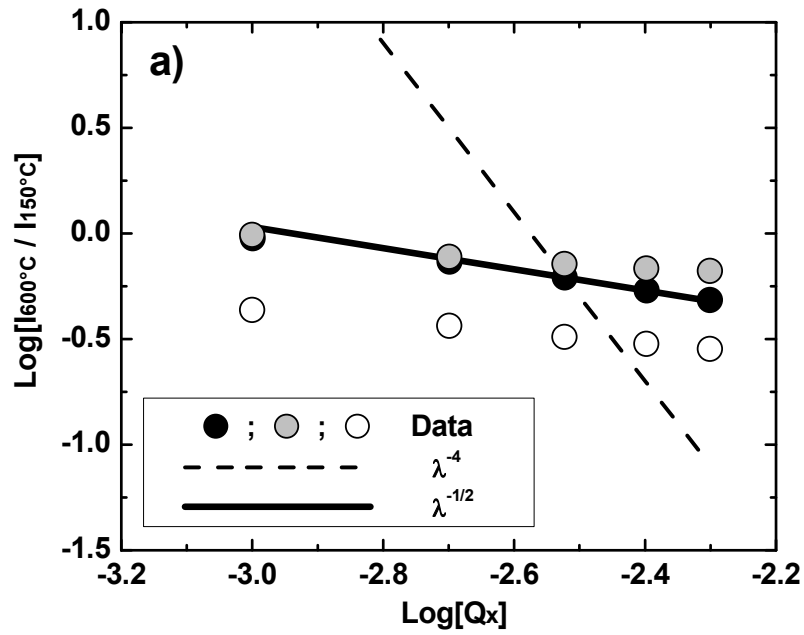
**Figure 51 Roughness amplitude decay: Comparison of models. (a) Nominally 300Å (black circles), 500Å (grey circles) and 800Å (white circles) thick specimens are compared to classical models of surface smoothening for which the decay exponent is varied. (b) Nominally 300Å (black circles) are compared to non-classical models of surface smoothening. The y-axis has been rescaled for clarity.**

The effects of capillarity at an incoherent interface of a passivated surface have recently been modeled [Rabkin 2012]. The model is analogous to that developed for a free surface, but is extended to include an elastically deformable surface layer. Rabkins Model is plotted in Figure 51(b) (dotted line). The trace of Rabkins model was generated using a product of anneal time (t) and Mullins coefficient (B) (as defined in equation ( 1-24 )) equal to $10^{-32}$ m$^{-4}$.

The difference in wavelength dependence and the lack of significant change of the lower Cu/SiO$_2$ interface are clear indications that buried interfaces may evolve differently from free surfaces. It is therefore hypothesized that the mechanical constraints of the opposing layer material are significant and thus warrant further investigation. Indeed, the Rabkin model is based on a similar hypothesis and proposes a roughness decay rate that explicitly depends on passivation layer thickness. The model developed by Rabkin follows the data presented herein; however closer examination of Figure 51 reveals that the curvature predicted by Rabkin's model is not experimentally realized. Further development of a Mullins-Rabkin-like model should be modified to allow for a plastically deforming encapsulating layer. It should also be noted that the observed differences in smoothing between SiO$_2$ and Ta/SiO$_2$ encapsulated Cu films are consistent with the expectation that the diffusivity of Cu in a Cu/dielectric interface is higher than that in a Cu/metal interface [Gan *et al.* 2011], [Lane *et al.* 2003].

## 5.3 Conclusions

X-ray reflectivity methods were used to study the evolution of interface roughness with annealing for a series of Cu thin films with thicknesses ranging from 270Å to 1580Å . The films were encapsulated in both SiO$_2$ and Ta/SiO$_2$ and were prepared by sputter

deposition onto thermally oxidized Si wafers. Specular X-ray reflectivity was used to separately determine the root mean square roughness for both the upper and lower Cu/SiO$_2$ (or Cu/Ta) interfaces and to study the growth dynamics of sputtered Cu. The lateral (in-plane) roughness characteristics were studied by diffuse X-ray reflectivity.

While all samples appeared to follow similar growth dynamics, notable differences in the roughness evolution with high temperature ex-situ annealing were observed. The annealing resulted in a smoothing of only one interface for the SiO$_2$ encapsulated films, while neither interface of the Ta/SiO$_2$ encapsulated films evolved significantly. The fact that only the upper Cu/SiO$_2$ interface evolves is attributed to mechanical pinning of the lower interface to the rigid substrate. The lack of evolution of the Cu/Ta/SiO$_2$ interface is consistent with the lower diffusivity expected of Cu in a Cu/Ta interface as compared to that in a Cu/SiO$_2$ interface. The smoothing of the upper Cu/SiO$_2$ interface qualitatively follows that expected for capillarity driven surface diffusion but with notable quantitative deviation.

# CHAPTER SIX : SUMMARY

The field of x-ray scattering encompasses a variety of analytical methods which can readily be applied to thin film analysis. In the experiments discussed here x-ray diffraction and x-ray reflectivity were primarily used to study metallic thin films of relevance to the microelectronics industry. Emphasis was placed on (1) phase identification of polycrystalline thin films, (2) the evaluation of the grain size and microstrain of metallic thin films by line profile analysis, and (3) the study of morphological evolution in solid/solid interfaces. In these efforts, the following is thus concluded:

(1) Pt-Ru thin film alloys present a notable increase in the compositional range of the HCP, suggesting a metastable extension of the HCP phase stability as compared to bulk Pt-Ru alloys. The steepest change in the electronic work function for the intermediate alloy compositions coincided with a rapid change in the c/a ratio of the HCP phase.

(2) Grain size analysis by traditional line profile fitting methods are limited by intra-granular distortions which arise from dislocation core spreading at the film interfaces. The extensive TEM based investigations of thin film gain sizes made possible the formulation of a novel "residual" peak width: Dislocations were thus found to contribute significantly to peak broadening and the development of an empirical line profile method for grain size analysis of thin films on substrates was motivated.

(3) X-ray reflectivity was used to study the interfacial evolution of encapsulated Cu thin films. The tendencies of such buried interfaces to evolve with time and

temperature will be crucial to the reliability of future nanoelectronic devices and are not yet well understood. Qualitatively, the interfaces evolve in a manner consistent with capillarity, albeit with some notable differences. Specifically, a $\lambda^{-\frac{1}{2}}$ dependence on roughness decay, rather than the expected $\lambda^{-4}$ dependence, was observed. In the case of a non-evolving bottom $SiO_2/Cu$ interface, the deviation from capillarity is hypothesized to stem from the coupling of kinetic properties to mechanical properties. Whereas the lack of notable changes in either $Cu/Ta$ interfaces is attributed to the lower diffusivity of $Cu$ on $Ta$ compared with $Cu$ on $SiO_2$. Mechanical coupling would also be expected to play a role in $Cu/Ta$ systems; however, the absence of a changing interface prevents this effect from being observed.

# CHAPTER SEVEN : FUTURE WORK

## 7.1 Future work in grain size and microstructural analysis of metallic thin films

The present work demonstrates that the widely used x-ray line profile techniques generally fail to provide reliable measures of grain size for metallic thin films. The conclusion of these investigations is that defect densities prevent reliable measures of average grain boundary separation, stemming from heavily distorted, and hence incoherent, lattices.

The novel residual width parameter, and its close correlation to dislocation density, suggests that an empirical method of grain size analysis is possible. This proposed method will depend on reliably measuring the dislocation density of thin films.

Because TEM analysis revealed misorientations over a sub-grain length scale in excess of 50°, these grains may readily be considered as plastically deformed. Such plastic deformation necessitates the presence of dislocations: i.e. geometrically necessary dislocations. These defects were first proposed by Nye [Nye 1953], and may be understood to be the dislocations required to accommodate a given amount of curvature in crystalline mater. These dislocations have been discussed in literature extensively, especially pertaining to their roll in size-dependant plasticity [Gao *et al.* 2003].

The significant distortions, i.e. curvatures, within individual grains, as evident in Figure 36, motivates TEM-based quantification of geometrically necessary dislocations. Analogous electron microscopy based analyses of these defects have been carried out in the past, but have focused on electron backscatter diffraction methods [El-Dasher *et al.* 2003] [Demir *et al.* 2009]. The proposed future work would employ TEM based

investigations and ASTAR orientation mapping. Dislocation densities measured by such TEM analysis would be compared to x-ray based measures. A goal of this research would be (1) to compare TEM and X-ray measures of dislocation density; (2) eliminate ambiguity in the value of the constant, A, in equation ( 1-14 ); and (3) to further develop the proposed empirical method of grain size analysis.

## 7.2 Future investigations into the morphological stability of interfaces

The present work demonstrates that wavelength roughness smoothens more quickly than long wavelength roughness, but modifies this known phenomena in that the exact value of the decay exponent in equation ( 1-24 ) must be modified to properly represent the evolution of solid/solid interfaces. The more rapid smoothing of short wavelength perturbations motivates the use of a corrugated surface profile when the Fourier series of a square wave is considered:

$$A_{square} = \frac{4}{\pi} \sum_{n=1,3,5,\ldots}^{\infty} \frac{1}{n} \sin\left(\frac{n\pi x}{\lambda}\right) \tag{7-1}$$

Such a corrugated surface therefore is expected to provide real and measurable roughness wavelengths, instead of the random roughness of a self-affine interface for which a continuum of roughness wavelengths must be assumed. Because a square wave is composed of an infinite sum of odd integer harmonics, the surface should decay in a predictable manner: Equation ( 1-24 ) dictates that the short wavelength terms (i.e. the higher order Fourier coefficients of the square wave) will decay more rapidly. This results initially in the rounding-off of square corners, and is followed by a decrease in amplitude of the surface height. By measuring this topographic decay, it should be possible to quantify the interface smoothing kinetics.

The fact that these interfaces are buried prevents the use of atomic force microscopy or related surface characterization techniques. Accordingly, X-ray reflectivity will be used to probe the changing height profile. The intensity of diffusely reflected X-rays is related to the Fourier transform of the scattering interface. This implies the existence of a primary Fourier peak located at $2\pi/d$ (where d is the period spacing), whose intensity decay can be measured and attributed to the smoothing of the interface. Similar topographies have been analyzed on polymer surfaces using the same principle [Geue et al. 2002]. The decay of surface heights can therefore be measured by analysis of the aforementioned primary Fourier peak in the diffuse reflectivity spectrum and its changing amplitude. Quantitative models of capillarity driven surface evolution due to surface diffusion are shown in Figure 52(a). A schematics of the expected corresponding diffuse x-ray scattering intensity spectrums are depicted in Figure 52(b). The model in Figure 52(a) assumes a period spacing of 2000Å with a peak-to-trough amplitude of 100Å.
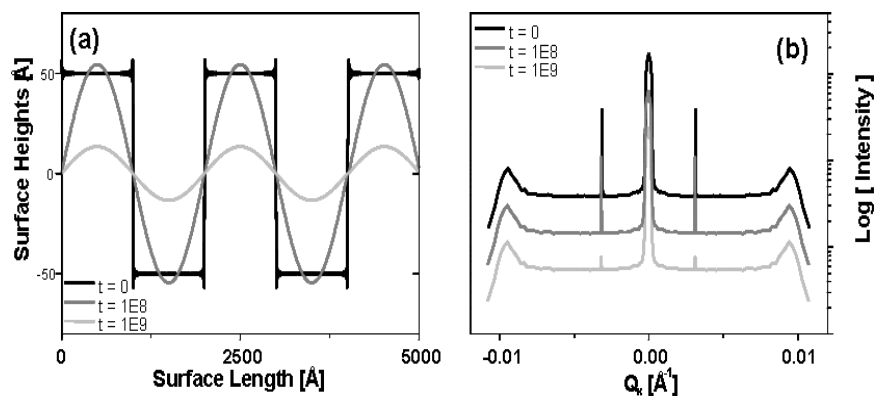


**Figure 52 (a) Corrugation decay (b) Expected diffuse reflectivity pattern**

119

Although the specular signal (not shown) contains no information regarding the in plane nature of a surface, the method may still be useful for the study of planar interface diffusion: The grated interfaces will be "seen" by the incident x-rays as a single continuous layer, whose density is equal to the average of Cu and the encapsulating material. Therefore the grated interface may be modeled as a separate layer, whose thickness will be indicative of the grating amplitude.

These studies will be based on thin films of Cu whose thickness exceeds the attenuation length of the incident X-rays ($>0.5\mu m$ for 1.54Å X-rays at a 5° incident angle); which are subsequently lithographically patterned, encapsulated, and annealing.

Using E-beam lithography, a nominally square grating has been processed at the Center for Nanophase Materials Sciences (CNMS) at Oakridge National Labs. The techniques for etching Cu have recently been developed by researchers at Oakridge making it a well suited facility for pursuing these studies. Cross-sectional and plan view SEM images are presented in Figure 53(a) and (b) respectively. The cross section presented in Figure 53(a) was prepared by ion milling in a focused ion beam; the image was subsequently collected in a SEM wherein the specimen was at an inclination of 45°.
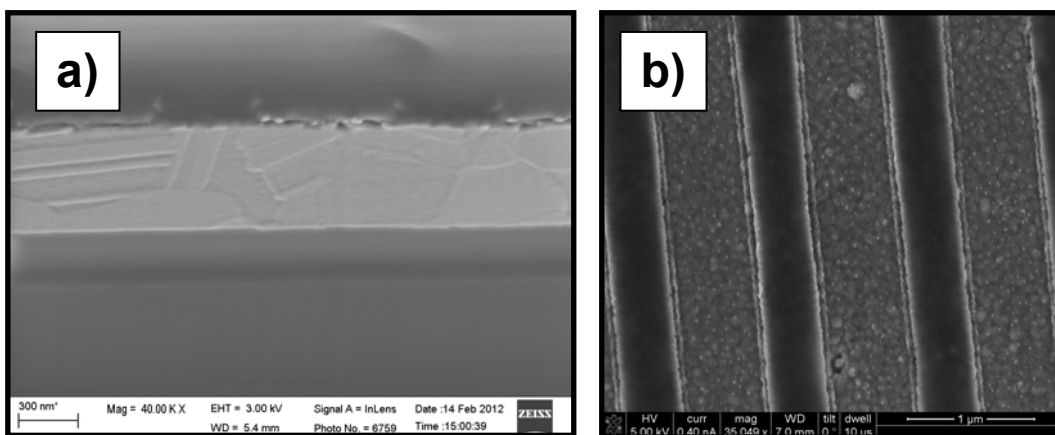


**Figure 53 SEM micrograph of corrugated Cu (a) cross section (b) plan view**
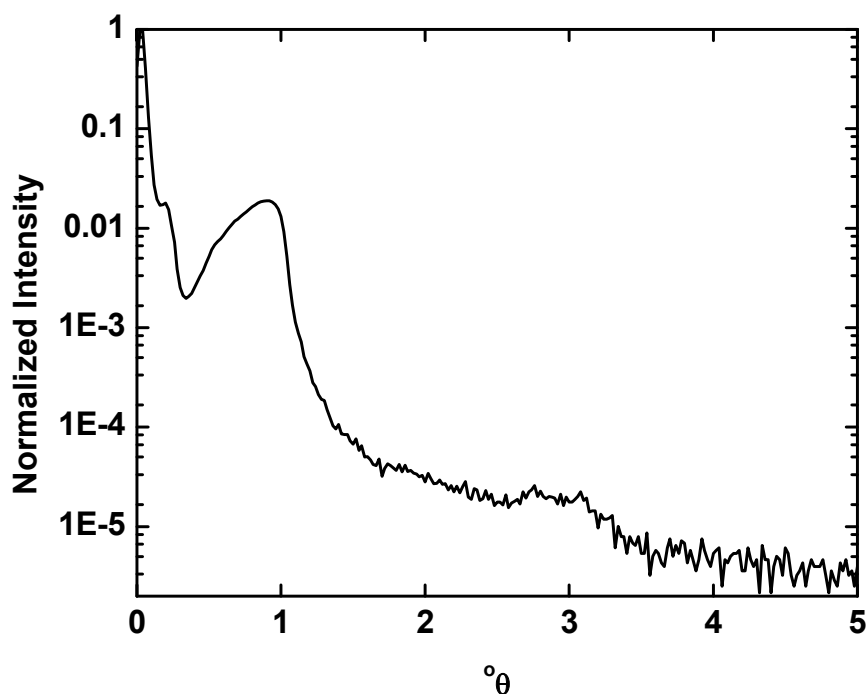
**Figure 54 Attempted XRR of corrugated Cu film**

First attempts to study these films by x-ray scattering have been unsuccessful (Figure 54). No measurable oscillations from the grated interface have been detected. Similarly, no discernable diffuse pattern was detected. The lack of measurable x-ray scattering patterns may be attributed to the notable roughness along the interface, superimposed on the grated pattern, resulting from e-beam exposure (Figure 53). Further development of etching processes is therefore required so that smoother and more idealized square pulse patterns may be lithographically processed into the Cu surface.

# REFERENCES

[Aarão Reis 2001] Aarão Reis FDA "Universality and Corrections to Scaling in the Ballistic Deposition Model," Physical Review E, **63** (2001)

[Abrikosov et al. 1993] Abrikosov IA, Skriver HL "Self-Consistent Linear-Muffin-Tin-Orbitals Coherent-Potential Technique for Bulk and Surface Calculations: Cu-Ni, Ag-Pd, and Au-Pt Random Alloys," Physical Review B, **47**, 16532 (1993)

[Balluffi et al. 2005] Balluffi RW, Allen SM, Carter WC, Kemper RA, Kinetics of Materials, J. Wiley & Sons, Hoboken, N.J (2005)

[Balogh et al. 2006] Balogh L, Ribaarik G, Ungár T "Stacking Faults and Twin Boundaries in Fcc Crystals Determined by X-Ray Diffraction Profile Analysis," Journal of Applied Physics, **100**, 023512 (2006)

[Barabási et al. 1995] Barabási A-L, Stanley EH, Fractal Concepts in Surface Growth, Press Syndicate of the University of Cambridge, New York, NY, USA (1995)

[Birkholz et al. 2006] Birkholz M, Fewster PF, Genzel C, Thin Film Analysis by X-Ray Scattering, John Wiley, Germany, Weinheim (2006)

[Bragg 1913] Bragg WL "The Diffraction of Short Electromagnetic Waves by a Crystal," Proceedings of the Cambridge Philosophical Society, **17**, 43 (1913)

[Brune et al. 1995] Brune H, Bromann K, Röder H, Kern K, Jacobsen J, Stoltze P, Jacobsen K, Norskov J "Effect of Strain on Surface Diffusion and Nucleation," Physical Review B, **52**, R14380 (1995)

[Castez et al. 2006] Castez M, Salvarezza R, Solari H "Modeling Growth from the Vapor and Thermal Annealing on Micro- and Nanopatterned Substrates," Physical Review E, **73** (2006)

[Choi 2011] Choi D, Tungsten as a Next-Generation Interconnect Metal in Semiconductor Devices, Ph.D., Carnegie Mellon University (2011)

[Choi et al. 2012] Choi D, Kim CS, Naveh D, Chung S, Warren AP, Nuhfer NT, Toney MF, Coffey KR, Barmak K "Electron Mean Free Path of Tungsten and the Electrical Resistivity of Epitaxial (110) Tungsten Films," Physical Review B, **86**, 045432 (2012)

[Cullity et al. 2001] Cullity BD, Stock SR, Elements of X-Ray Diffraction, Prentice Hall, Upper Saddle River, NJ (2001)

[De Boer et al. 1996] De Boer DKG, Leenaers AJG "Probing Interface Roughness by X-Ray Scattering," Physica B: Condensed Matter, **221**, 18 (1996)

[Demir *et al.* 2009] Demir E, Raabe D, Zaafarani N, Zaefferer S "Investigation of the Indentation Size Effect through the Measurement of the Geometrically Necessary Dislocations beneath Small Indents of Different Depths Using Ebsd Tomography," Acta Materialia, **57**, 559 (2009)

[Dubson *et al.* 1994] Dubson M, Jeffers G "Profile Decay by Surface Diffusion at Low Temperature," Physical Review B, **49**, 8347 (1994)

[Edwards *et al.* 1982] Edwards SF, Wilkinson DR "The Surface Statistics of a Granular Aggregate," Proceedings of the Royal Society A: Mathematical, Physical and Engineering Sciences, **381**, 17 (1982)

[El-Dasher *et al.* 2003] El-Dasher BS, Adams BL, Rollett AD "Viewpoint: Experimental Recovery of Geometrically Necessary Dislocation Density in Polycrystals," Scripta Materialia, **48**, 141 (2003)

[Erlebacher *et al.* 2000] Erlebacher J, Aziz MJ, Chason E, Sinclair MB, Floro JA "Nonclassical Smoothening of Nanoscale Surface Corrugations," Physical Review Letters, **84**, 5800 (2000)

[Eshelby 1949] Eshelby JD "Edge Dislocations in Anisotropic Materials " Phil. Mag., **40**, 903 (1949)

[Family *et al.* 1985] Family F, Vicsek T "Scaling of the Active Zone in the Eden Process on Percolation Networks and the Ballistic Deposition Model," Journal of Physics A: Mathematical and General, **18**, L75 (1985)

[Gan *et al.* 2011] Gan D, Ho PS, Pang Y, Huang R, Leu J, Maiz J, Scherban T "Effect of Passivation on Stress Relaxation in Electroplated Copper Films," Journal of Materials Research, **21**, 1512 (2011)

[Gao *et al.* 2003] Gao H, Huang Y "Geometrically Necessary Dislocation and Size-Dependent Plasticity," Scripta Materialia, **48**, 113 (2003)

[Gao *et al.* 2002] Gao H, Zhang L, Baker SP "Dislocation Core Spreading at Interfaces between Metal Films and Amorphous Substrates," Journal of the Mechanics and Physics of Solids, **50**, 2169 (2002)

[Geue *et al.* 2002] Geue T, Henneberg O, Pietsch U "X-Ray Reflectivity from Sinusoidal Surface Relief Gratings," Crystal Research and Technology, **37**, 770 (2002)

[Gonçalves *et al.* 2012] Gonçalves NS, Carvalho JA, Lima ZM, Sasaki JM "Size–Strain Study of Nio Nanoparticles by X-Ray Powder Diffraction Line Broadening," Materials Letters, **72**, 36 (2012)

[Gupta 2005] Gupta D, <u>Diffusion Processes in Advanced Technological Materials</u>, William Andrew, Inc., Norwich, N.Y (2005)

[Hofmann *et al.* 2009] Hofmann F, Song X, Dolbnya I, Abbey B, Korsunsky AM "Probing Intra-Granular Deformation by Micro-Beam Laue Diffraction," Procedia Engineering, **1**, 193 (2009)

[Holý *et al.* 1999] Holý V, Baumbach T, Pietsch U, <u>High-Resolution X-Ray Scattering from Thin Films and Multilayers</u>, Springer Tracts in Modern Physics, 0081-3869 ; V. 149, Springer, Berlin ; New York (1999)

[Hughes *et al.* 1991] Hughes DA, Hansen N "Microstructural Evolution in Nickel During Rolling and Torsion," Materials Science and Technology, **7**, 544 (1991)

[Jiran *et al.* 1990] Jiran E, Thompson C "Capillary Instabilities in Thin Films," Journal of Electronic Materials, **19**, 1153 (1990)

[Kardar *et al.* 1986] Kardar M, Parisi G, Zhang Y-C "Dynamic Scaling of Growing Interfaces," Physical Review Letters, **56**, 889 (1986)

[Keblinski *et al.* 1996] Keblinski P, Maritan A, Toigo F, Messier R, Banavar J "Continuum Model for the Growth of Interfaces," Physical Review E, **53**, 759 (1996)

[Khorsand Zak *et al.* 2012] Khorsand Zak A, Majid WHA, Ebrahimizadeh Abrishami M, Yousefi R, Parvizi R "Synthesis, Magnetic Properties and X-Ray Analysis of Zn0.97x0.03o Nanoparticles (X = mn, Ni, and Co) Using Scherrer and Size–Strain Plot Methods," Solid State Sciences, **14**, 488 (2012)

[Kim *et al.* 2005] Kim T-W, Park S-J, Jones LE, Toney MF, Park K-W, Sung Y-E "Structure and Electrocatalysis of Sputtered Rupt Thin-Film Electrodes," The Journal of Physical Chemistry B, **109**, 12845 (2005)

[Korsunsky *et al.* 2012] Korsunsky AM, Hofmann F, Abbey B, Song X, Belnoue JP, Mocuta C, Dolbnya I "Analysis of the Internal Structure and Lattice (Mis)Orientation in Individual Grains of Deformed Cp Nickel Polycrystals by Synchrotron X-Ray Micro-Diffraction and Microscopy," International Journal of Fatigue, **42**, 1 (2012)

[Lanckmans *et al.* 2002] Lanckmans F, Brongersma SH, Varga I, Poortmans S, Bender H, Conard T, Maex K "A Quantitative Adhesion Study between Contacting Materials in Cu Damascene Structures," Applied Surface Science, **201**, 20 (2002)

[Lane *et al.* 2003] Lane MW, Liniger EG, Lloyd JR "Relationship between Interfacial Adhesion and Electromigration in Cu Metallization," Journal of Applied Physics, **93**, 1417 (2003)

[Langford *et al.* 1988] Langford JI, Delhez R, Keijser THD, Mittemeijer EJ "Profile Analysis for Microcrystalline Properties by the Fourier and Other Methods," Aust. J. Phys., **41**, 173 (1988)

[Langford *et al.* 1978] Langford JI, Wilson AJC "Scherrer after Sixty Years: A Survey and Some New Results in the Determination of Crystallite Size," Journal of Applied Crystallography, **11**, 102 (1978)

[Larche *et al.* 1982] Larche FC, Cahn JL "The Effect of Self-Stress on Diffusion in Solids," Acta Metallurgica, **30**, 1835 (1982)

[Laue 1913] Laue MV "Röntgenstrahlinterferenzen," Physikalische Zeitschrift, **14**, 1075 (1913)

[Lita *et al.* 2000] Lita AE, Sanchez JE, Jr. "Effects of Grain Growth on Dynamic Surface Scaling During the Deposition of Al Polycrystalline Thin Films," Physical Review B, **61**, 7692 (2000)

[Maiya *et al.* 1965] Maiya PS, Blakely JM "A Technique for Study of Mass Transport Mechanisms at Crystal Surfaces," Applied Physics Letters, **7**, 60 (1965)

[Mandelbrot 1985] Mandelbrot BB "Self-Affine Fractals and Fractal Dimension," Physica Scripta, **32**, 257 (1985)

[Massalski *et al.* 1990] Massalski TB, Okamoto H, <u>Binary Alloy Phase Diagrams / Editor-in-Chief, Thaddeus B. Massalski ; Editors, Hiroaki Okamoto, P.R. Subramanian, Linda Kacprzak ; Publisher, William W. Scott, Jr</u>, Materials Park, Ohio : ASM International (1990)

[Meakin 1998] Meakin P, <u>Fractals, Scaling, and Growth Far from Equilibrium,</u> Cambridge Nonlinear Science Series ; 5, Cambridge University Press, Cambridge, U.K. ; New York (1998)

[Müllner *et al.* 1998] Müllner P, Arzt E "Observation of Dislocations Disappearance in Aluminum Thin Films and Consequences for Thin Film Properties" Mater. Res. Soc. Symp. Proc., **505**, 149 (1998)

[Nichols *et al.* 1965] Nichols FA, Mullins WW "Morphological Changes of a Surface of Revolution Due to Capillarity-Induced Surface Diffusion," Journal of Applied Physics, **36**, 1826 (1965)

[Nye 1953] Nye JF "Some Geometrical Relations in Dislocated Solids," Acta Metallurgica, **1**, 153 (1953)

[Ogilvy *et al.* 1989] Ogilvy JA, Foster JR "Rough Surfaces: Gaussian or Exponential Statistics?," Journal of Physics D: Applied Physics, **22**, 1243 (1989)

[Overton *et al.* 1955] Overton W, Gaffney J "Temperature Variation of the Elastic Constants of Cubic Elements. I. Copper," Physical Review, **98**, 969 (1955)

[Parratt 1954] Parratt LG "Surface Studies of Solids by Total Reflection of X-Rays," Physical Review, **95**, 359 (1954)

[Pelliccione *et al.* 2008] Pelliccione M, Lu TM, <u>Evolution of Thin-Film Morphology Modeling and Simulations</u>, Springer Series in Materials Science ; V. 108. 0933-033x, Springer, Berlin ; New York (2008)

[Rabkin 2012] Rabkin E "Flattening of a Passivated Solid Surface Due to Capillarity," Scripta Materialia, **67**, 625 (2012)

[Read *et al.* 1950] Read WT, Shockley W "Dislocation Models of Crystal Grain Boundaries," Physical Review, **78**, 275 (1950)

[Révész *et al.* 1996] Révész Á, Ungár T, Borbély A, Lendvai J "Dislocations and Grain Size in Ball-Milled Iron Powder," Nanostructured Materials, **7**, 779 (1996)

[Savaloni *et al.* 2006] Savaloni H, Gholipour-Shahraki M, Player MA "A Comparison of Different Methods for X-Ray Diffraction Line Broadening Analysis of Ti and Ag Uhv Deposited Thin Films: Nanostructural Dependence on Substrate Temperature and Film Thickness," Journal of Physics D: Applied Physics, **39**, 2231 (2006)

[Scherrer 1918] Scherrer P "Bestimmung Der Größe Und Der Inneren Struktur Von Kolloidteilchen Mittels Röntgenstrahlen," Nachrichten von der Königlichen Gesellschaft der Wissenschaften zu Göttingen, Mathematisch-physikalische Klasse (1918)

[Schlatmann *et al.* 1996] Schlatmann R, Shindler JD, Verhoeven J "Evolution of Surface Morphology During Growth and Ion Erosion of Thin Films," Physical Review B, **54**, 10880 (1996)

[Schmidbauer 2003] Schmidbauer M, <u>X-Ray Diffuse Scattering from Self-Organized Mesoscopic Semiconductor Structures</u>, Springer Tracts in Modern Physics, 0081-3869 ; V. 199, Springer, Berlin ; New York (2003)

[Shu *et al.* 2001] Shu D, Liu F, Gong X "Simple Generic Method for Predicting the Effect of Strain on Surface Diffusion," Physical Review B, **64** (2001)

[Sinha *et al.* 1988] Sinha SK, Sirota EB, Garoff S "X-Ray and Neutron Scattering from Rough Surfaces," Physical Review B, **38**, 2297 (1988)

[Smilgies 2009] Smilgies DM "Scherrer Grain-Size Analysis Adapted to Grazing-Incidence Scattering with Area Detectors," J Appl Crystallogr, **42**, 1030 (2009)

[Stokes *et al.* 1944] Stokes AR, Wilson AJC "The Diffraction of X Rays by Distorted Crystal Aggregates - I," Proceedings of the Physical Society, **56**, 174 (1944)

[Sun 2009] Sun T, <u>Classical Size Effect in Copper Thin Films: Impact of Surface and Grain Boundary Scattering on Resistivity</u>, Ph.D., University of Central Florida (2009)

[Sun *et al.* 2009] Sun T, Yao B, Warren A, Barmak K, Toney M, Peale R, Coffey K "Dominant Role of Grain Boundary Scattering in the Resistivity of Nanometric Cu Films," Physical Review B, **79** (2009)

[Sun *et al.* 2010] Sun T, Yao B, Warren AP, Barmak K, Toney MF, Peale RE, Coffey KR "Surface and Grain-Boundary Scattering in Nanometric Cu Films," Physical Review B, **81** (2010)

[Sun *et al.* 2008] Sun T, Yao B, Warren AP, Kumar V, Roberts S, Barmak K, Coffey KR "Classical Size Effect in Oxide-Encapsulated Cu Thin Films: Impact of Grain Boundaries Versus Surfaces on Resistivity," Journal of Vacuum Science & Technology A: Vacuum, Surfaces, and Films, **26**, 605 (2008)

[Todi *et al.* 2007] Todi RM, Erickson MS, Sundaram KB, Barmak K, Coffey KR "Comparison of the Work Function of Pt&Ndash;Ru Binary Metal Alloys Extracted from Mos Capacitor and Schottky-Barrier-Diode Measurements," Electron Devices, IEEE Transactions on, **54**, 807 (2007)

[Todi *et al.* 2006] Todi RM, Warren AP, Sundaram KB, Barmak K, Coffey KR "Characterization of Pt-Ru Binary Alloy Thin Films for Work Function Tuning," Electron Device Letters, IEEE, **27**, 542 (2006)

[Tolan 1998] Tolan M, <u>X-Ray Scattering from Soft-Matter Thin Films : Materials Science and Basic Research</u>, Springer Tracts in Modern Physics ; 148, Springer, New York (1998)

[Ungár 1996] Ungár T "Strain Broadening Caused by Dislocations," Advances in X-ray Analysis, **40** (1996)

[Ungár 2008] Ungár T "Dislocation Model of Strain Anisotropy," Powder Diffraction, **23**, 125 (2008)

[Ungár *et al.* 1996] Ungár T, Borbely A "The Effect of Dislocation Contrast on X-Ray Line Broadening: A New Approach to Line Profile Analysis," Applied Physics Letters, **69**, 3173 (1996)

[Ungár *et al.* 1999] Ungár T, Dragomir I, Revesz A, Borbely A "The Contrast Factors of Dislocations in Cubic Crystals: The Dislocation Model of Strain Anisotropy in Practice," Journal of Applied Crystallography, **32**, 992 (1999)

[Ungár *et al.* 2012] Ungár T, Tichy G, Gubicza J, Hellmig RJ "Correlation between Subgrains and Coherently Scattering Domains," Powder Diffraction, **20**, 366 (2012)

[Vidal *et al.* 1984] Vidal B, Vincent P "Metallic Multilayers for X Rays Using Classical Thin-Film Theory," Appl. Opt., **23**, 1794 (1984)

[Vvedensky 2003] Vvedensky D "Edwards-Wilkinson Equation from Lattice Transition Rules," Physical Review E, **67** (2003)

[Wang *et al.* 2011] Wang J, Misra A "An Overview of Interface-Dominated Deformation Mechanisms in Metallic Multilayers," Current Opinion in Solid State and Materials Science, **15**, 20 (2011)

[Warren *et al.* 2008] Warren AP, Todi RM, Yao B, Barmak K, Sundaram KB, Coffey KR "On the Phase Identification of Dc Magnetron Sputtered Pt–Ru Alloy Thin Films," Journal of Vacuum Science & Technology A: Vacuum, Surfaces, and Films, **26**, 1208 (2008)

[Warren 1990] Warren BE, <u>X-Ray Diffraction</u>, Dover Publications, New York (1990)

[Wilk *et al.* 2001] Wilk GD, Wallace RM, Anthony JM "High-K Gate Dielectrics: Current Status and Materials Properties Considerations," Journal of Applied Physics, **89**, 5243 (2001)

[Wilkens 1970] Wilkens M "The Determination of Density and Distribution of Dislocations in Deformed Single Crystals from Broadened X-Ray Diffraction Profiles," physica status solidi (a), **2**, 359 (1970)

[Wilkens *et al.* 1987] Wilkens M, Ungár T, Mughrabi H "X-Ray Rocking-Curve Broadening of Tensile-Deformed 001 -Orientated Copper Single-Crystals," Physica Status Solidi a-Applied Research, **104**, 157 (1987)

[Williamson *et al.* 1953] Williamson GK, Hall WH "X-Ray Line Broadening from Filed Aluminium and Wolfram," Acta Metallurgica, **1**, 22 (1953)

[Wormington *et al.* 1999] Wormington M, Panaccione C, Matney KM, Bowen KD "Characterization of Structures from X-Ray Scattering Data Using Genetic Algorithms," Philosophical Transactions of the Royal Society of London. Series A: Mathematical, Physical and Engineering Sciences, **357**, 2827 (1999)

[Yao *et al.* 2008] Yao B, Coffey KR "Back-Etch Method for Plan View Transmission Electron Microscopy Sample Preparation of Optically Opaque Films," Journal of Electron Microscopy, **57**, 47 (2008)

[Yao *et al.* 2008] Yao B, Coffey KR "A High-Throughput Approach for Cross-Sectional Transmission Electron Microscopy Sample Preparation of Thin Films," J Electron Microsc (Tokyo), **57**, 189 (2008)